Bureau of Safety and Environmental Enforcement (BSEE) Report: Computational Fluid Dynamics (CFD) Model for Predicting Wellhead Oil-Burning Efficiency at Bench and Intermediate Scales: Interim Report

Steven G. Tuttle, David A. Kessler, Brian T. Fisher, Christopher J. Pfützner, Aaron W. Skiba, Rohit J. Jacob

This page intentionally left blank

REPORT DOCUMENTATION PAGE

1. REPORT DATE *(DD-MM-YYYY)*	2. REPORT TYPE		3. DATES COVERED *(From -To)*
	NRL Memorandum Report		

4. TITLE AND SUBTITLE

Computational Fluid Dynamics (CFD) Model for Predicting Wellhead Oil-Burning Efficiency at Bench and Intermediate Scales: Interim Report

5a. CONTRACT NUMBER

5b. GRANT NUMBER
E15PG00022

5c. PROGRAM ELEMENT NUMBER

6. AUTHOR(S)

Steven G. Tuttle, David A. Kessler, Brian T. Fisher, Christopher J. Pfützner, Aaron W. Skiba*, Rohit J. Jacob**

5d. PROJECT NUMBER
61-1M82-0-9-5

5e. TASK NUMBER

5f. WORK UNIT NUMBER
1M82

7. PERFORMING ORGANIZATION NAME(S) AND ADDRESS(ES)

Naval Research Laboratory
4555 Overlook Avenue, SW
Washington, DC , 20375-5320

8. PERFORMING ORGANIZATION REPORT

NRL/MR/6185--20-####

9. SPONSORING / MONITORING AGENCY NAME(S) AND ADDRESS(ES)

Bureau of Safety & Environmental Enforcement
45600 Woodland Road, VAE-AMD
Sterling VA 20166

10. SPONSOR/MONITOR'S ACRONYM(S)
MIS-NONDOD

11. SPONSOR/MONITOR'S REPORT NUMBER(S)

12. DISTRIBUTION / AVAILABILITY STATEMENT

DISTRIBUTION STATEMENT A: Approved for public release; distribution is unlimited.

13. SUPPLEMENTARY NOTES
* American Society of Engineering Education Postdoctoral Fellow
** National Research Council Postdoctoral Fellow

14. ABSTRACT

While wellhead burning has been an oil field hazard for generations, the oil exploration community has begun to view it as a potential spill response tool. Presently, there are significant gaps in the validated science to reliably and accurately predict the burn efficiency of a wellhead. A coupled, multi-physics spray combustion model has been developed and validated with multi-scale experiments for wellhead burning. Spray measurement and sub-scale burn efficiency measurement methods have been developed and applied to determine the behaviors that drive low wellhead burn efficiency. Analysis of potential wellhead spray conditions revealed that the worst-case discharge scenario may not create the worst-case spill scenario because lower flow rates produce thicker wellbore films, which lead to lower burn efficiencies.

15. SUBJECT TERMS
Crude oil, in situ burn, wellhead blowout, burn efficiency, combustion, flame, burn residual

16. SECURITY CLASSIFICATION OF:			17. LIMITATION OF ABSTRACT	18. NUMBER OF PAGES	19a. NAME OF RESPONSIBLE PERSON
a. REPORT UNCLASSIFIED	**b. ABSTRACT** UNCLASSIFIED	**c. THIS PAGE** UNCLASSIFIED	Unlimited Unclassified		

i

This page intentionally left blank

CONTENTS

FIGURES

TABLES

EXECUTIVE SUMMARY

While wellhead burning has been an oil field hazard for generations, the development of capping response technologies and practices by industry experts has enabled the oil exploration community to shift its views of wellhead burning from a hazard to an oil spill response tool. In order to examine the validity of such an approach, this study has developed computational fluid dynamic models, experiments to examine the fundamental behaviors of wellhead spray combustion that drive burn efficiency, and a critical review of the research that engineers and policy makers have been using to make decisions.

We have developed a computational architecture composed of a number of coupled models to accurately predict turbulent gas-phase mechanics and transport; spray injection, transport, collision, and evaporation; soot formation, transport, and radiation; and a range of other relevant mechanical, thermodynamic, and chemical processes. This architecture has been able to accurately predict the gas-phase behavior and examine how the spray influences the combustion behavior. In turn, it has opened up questions that have driven laboratory research to examine specific aspects of the two-phase spray.

In order to validate those predictions and provide accurate boundary conditions, a parallel effort of experimental development, measurement, and processing was performed. Two experimental platforms were developed to meet this need. A bench-scale experiment, composed of a flat, premixed hydrogen-air pilot flame and a central atomizing jet designed to simulate wellhead atomization, was used to examine fundamental spray transport, combustion temperature, flame anchoring, and atomization behavior. This study revealed that open pipe atomization processes produce spray plumes that are highly dependent on the two-phase flow characteristics of the wellbore flow. In particular, if the two-phase flow is annular, with a liquid film on the inside surface of the pipe and a central core flow of gas, the resulting spray will concentrate the liquid in an annular pattern in the plume. In such a flow, the central core of the flow is composed of small-diameter droplets traveling at or near the speed of the potential core of the gas jet and larger-diameter droplets traveling at much lower velocities. The higher speed droplets in the plume were formed as instability waves formed at the gas-liquid film interface as gas shear pulled ligaments from the film's waves, which then formed droplets. The lower speed droplets in the plume formed when the film was ejected at the mouth of the pipe to form ligaments, which then formed droplets much larger than those entrained at the core of the gas flow.

An intermediate-scale experiment was also developed to observe spray combustion behavior at a larger scale, though still much smaller than an actual wellbore. This experiment was used to make burn efficiency measurements and to observe the primary mechanisms of low burn efficiency. We discovered that for annular flows, the primary mechanism of droplet fallout was that of the larger annular droplets falling out of the plume. In the process, we developed a repeatable, reliable method to measure burn efficiency that will provide a platform for parametric studies of gas flow, liquid flow, and their combined influences on burn efficiency.

In order to examine this problem and provide scientific, engineering, and policy perspective, we also performed a literature review of the background research and policy. After examining a range of potential flow rates that might be encountered during a wellhead blowout, we discovered that the Worst-Case Discharge case, as defined by law and specified by permit-granting agencies, may not produce the worst-case spill scenario for a wellhead. The Worst-Case Discharge may actually burn with very high efficiency if there is sufficient wellhead pressure and gas flow available to entrain and atomize the crude oil. If the crude oil is not fully entrained, there is a possibility that the resulting annular spray may not burn efficiently.

NOMENCLATURE

a	Radiation adsorption coefficient (gas phase)		1/m
a_p	Radiation adsorption coefficient (secondary phase)		1/m
B_m	Spalding mass transfer		
C_W	Surface tension coefficient for annular wave circulation and dissipation		
C_d	Drag coefficient		
C_ι	Turbulence model constants		
C_p	Gas-phase specific heat		J/kgK
c	Flame reaction progress variable		
d_p	Droplet diameter		mm
D	Wellbore diameter	inches	mm
D_{vm}	Volume mean droplet diameter		μm
$D_{i,m}$	Diffusion coefficient		m^2/s
E_z	Entrainment volume fraction for a given length, z		
E_∞	Entrainment volume fraction for a fully developed or nearly infinite length pipe		
E_p	Radiation emission from secondary phase		W/m^3
Fr_G	Gas Froude number		
Fr_L	Liquid Froude number		
f_1	Gas-phase fuel mixture fraction		
f_2	Liquid-phase fuel mixture fraction		
GOR	Gas-oil ratio, volumetric	SCF/BBL	m^3/m^3
G	Incident radiation flux		W/m^2
G_k	Turbulent kinetic energy source term		Pa/s
H	Enthalpy		J/kg
h	Convective heat transfer coefficient		W/m^2K
h_{fg}	Latent heat of vaporization		J/kg
k	Turbulent kinetic energy		m^2/s^2
k_t	Turbulent thermal conductivity		W/m·K
L_b	Liquid sheet breakup length		m
m_p	Droplet mass		kg
N_μ	Entrainment viscosity number		
n	Index of refraction		
Oh	Ohnesorge number		
p	Pressure		atm
$\mathcal{R}$	Soot formation and destruction rate laws		kg/m^3s
Re_G	Superficial gas Reynolds number		
Re_L	Superficial liquid Reynolds number		
Sc	Schmidt number		
Sh	Sherwood number		
S_c	Reaction progress variable source term		kg/m^3s
$S_{D,m}$	Mass source term (exchange with secondary phase)		kg/m^3s
$S_{D,mom}$	Momentum source term (exchange with secondary phase)		kg/m^2s^2
$S_{D,H}$	Enthalphy source term (exchange with secondary phase)		kg/m^2s^2
$S_{D,f}$	Mixture fraction source terms (exchange with secondary phase)		kg/m^3s
S_h	Gas-phase enthalpy source term		J/kgs
T	Temperature		K
T_p	Droplet temperature		K
$U_{G,S}$	Superficial gas velocity; gas velocity in the pipe as if the liquid is not present.		m/s
$U_{L,S}$	Superficial liquid velocity; liquid velocity in the pipe as if the gas is not present.		m/s
U_l	Laminar flame speed		m/s

u	Vector velocity	m/s
u'	Vector turbulent velocity fluctuation	m/s
u_p	Droplet velocity	m/s
We_d	Droplet Weber number	
$We_{G,E}$	Entrainment Weber number	
x_p	Droplet position	m
Y_k	Mass fraction of the kth species	
z	Arbitrary entrainment length	
z_∞	Quasi-equilibrium entrainment development length	
α_k	Reaction progress variable molecular concentration coefficients	
δ	Annular film thickness	μm
ε	Turbulent energy dissipation rate	m^2/s^2
Λ	Kelvin-Helmholtz most unstable wavelength	m
μ_G	Gas viscosity	Pa·s
μ_L	Liquid viscosity	Pa·s
μ_t	Turbulent viscosity	Pa·s
ρ	Density, generalized	kg/m^3
ρ_G	Gas density	kg/m^3
ρ_L	Liquid density	kg/m^3
σ_L	Liquid-gas surface tension	N/m
σ_B	Stefan-Boltzmann constant	W/m^2K^4
σ_s	Radiation scattering coefficient	1/m
τ_r	Droplet relaxation time	s
Ω	Wave growth rate	1/s
ζ	Normalized entry length for entrainment fraction	
Σ	Flame surface area density	1/m

COMPUTATIONAL FLUID DYNAMICS (CFD) MODEL FOR PREDICTING WELLHEAD OIL-BURNING EFFICIENCY AT BENCH AND INTERMEDIATE SCALES: INTERIM REPORT

INTRODUCTION

Wellhead fires have been an industry concern for many years for their danger, expense, and, at times, their necessity. They produce very large and visible burning plumes that require significant skill and expertise to extinguish. Though these fires are not trivial to extinguish, there are a number of companies that have developed the expertise to reliably and safely extinguish wellhead fires [1,2]. With the maturation of these fire suppression techniques, wellhead fires can be viewed as a tool to manage and contain the environmental impact of a wellhead spill if the properties and flow rates of the gas and liquid are favorable. If favorable, wellhead burning can rapidly and inexpensively dispose of wellhead effluent more effectively than should the liquid effluent fall on the ground or waterways; in cases where burning is unfavorable, mechanical recovery is the only remediation option. Instead of devoting space to a thorough review of the progress in the analysis of wellheads and the related behavior, we will constrain our discussion to the latest work and leave a more thorough discussion of the background to a review paper we are writing.

Recent Work

In November 2017, the Ocean Energy Safety Institute (OESI)-hosted a peer review workshop entitled "Well Ignition as a Blowout Response" that provided a venue for industry, academic, and government to present their work on this topic and to review past research [3-24]. Many of the ideas discussed in the meeting were included in a meeting whitepaper written by Hasan and Kwon [25] that was then developed into an article written by Siddhamshetty *et al.* [26]. They expanded the method first suggested by the S.L. Ross and Energetex [5], used updated correlations, and accounted reservoir gas properties more carefully. The process they outlined to calculate the wellhead burn efficiency was as follows:

1. Determine the two-phase flow regime (bubbly, slug, churn, annular).

2. If annular, then determine the oil droplet size distribution.

3. Perform calculation determining the droplet evaporation and burning time scales to determine the flame height necessary to evaporate the droplets.

4. Perform a 0-dimensional heat release analysis from the gas to determine if sufficient heat is available to evaporate the liquid fuel.

5. Calculate the adiabatic flame temperature of the gas-phase flame and correct with radiant energy loss due to soot formation.

Siddhamshetty *et al.* then applied their approach to a worst-case discharge (WCD) case posited by Hilcorp for a potential well [27-29] to predict an efficiency of 100%. A careful examination of the process outlined above [5,26] will reinforce that they approached their calculations conservatively, but there are some caveats that must be considered.

Referring to Step 1, Siddhamshetty *et al.* [26] did not elaborate on the ramifications of how the wider range of two-phase flow regimes (bubble, slug, and churn) would impact the effluent plume. This is especially important in light of their choice of wellbore diameter. Siddhamshetty *et al.* [26] made the assumption that the wellbore diameter was 4-6 in. (102-152 mm). A careful examination of the Hillcorp documentation sets the casing's inside diameter at 8.5 in (216 mm) [29]. Such an change in diameter will shift the flow velocities significantly, depending on whether they conducted their analysis with the 102 or

152 mm-diameter wellbore. Though their focus was on the wellbore flow, a topic on which they are experts, they did not fully discuss how the wellbore flow would influence the ejected plume behavior, which directly influences how the oil and gas burns and how much will either fall back to the surface or remain vapor.

There was also a gap in the discussion over the annular flow entrainment fraction: the fraction of the liquid volume that has been entrained as droplets in the gas flow within the wellbore. A reader might incorrectly assume that annular flow in the wellbore would produce the same spray plume as that of a fully entrained mist, regardless of the entrainment fraction [30,31]. In recent experimental work, we have observed at laboratory and larger scales there is significant differences in spray plume behavior as the flow transitions between annular flow and a fully entrained mist. In Fisher *et al.* [32,33], we showed that annular flows with large liquid loading and/or thick annular films produce an annular spray plume with large, slower droplets at the periphery and small, high-speed droplets at the center.

We were also concerned by the statement that Siddhamshetty *et al.* made that the criterion for transition to annular flow is a GOR value of 500 SCF/BBL, with sufficient gas velocity. Though this statement might be a good industry rule of thumb, they did not elaborate to justify it. This is disconcerting because it assumes that the oil viscosity, surface tension, and density are irrelevant and what that sufficient, critical gas-phase velocity was never described or referenced [26]. We should expect that the superficial gas and liquid Reynolds numbers (Re_G and Re_L, respectively), pipe-diameter Weber number (We_D), and other dimensionless parameters should be used to express this behavior so that a wide range of reservoir properties can be applied. These dimensionless parameters will be defined later in this document.

Referring to Step 2, we should note that the Liberty well conditions that Siddhamshetty *et al.* [26] referenced were at significantly greater Re_G and Re_L than the validated range of the entrainment and droplet correlations [30,31,34-36]. This does not invalidate their conclusions because a careful reading of these background papers reveal that as the gas flow rates increase, the general trend is for the entrainment to approach 100% and droplet diameters to decrease. However, the reader should note that conditions outside of the validated range of a correlation do not allow it to be used for reliable prediction of droplet diameters. We should also consider that the cited correlations only consider the entrained droplets and not those formed as the un-entrained annular liquid film is expelled and atomized, which can form a significant fraction of the oil volume.

Step 3 assumes the primary mechanism that drives poor burn efficiency is that the droplet lifetime [37] is greater than the residence time within the burning plume. Though this is a potential a mechanism, it is not the only plausible mechanism. If we consider that much of the spray produced by flows with less than complete entrainment will be from the annular film and that the spray density of both the core and the periphery of the plume can be very high, two additional mechanisms are possible. One is that the larger droplets from the annular film are too large to evaporate or for the plume momentum to entrain them, so they fall to the ground. This mechanism corroborates with the Kuwaiti oil fire residue measurements of Henry and Overton [15], which revealed that the oil fallout residue was not significantly altered by the heat of the flames – pyrogenic compounds were not as common as those originally in the oil. Therefore, the oil fell to the ground before it could pass through the burning plume and undergo significant pyrogenic reactions. If the droplets were too large to have a long enough residence time in the plume to evaporate, it is probable that the oil would have still undergone appreciable pyrogenic reactions. A related evaporation failure mechanism is that the droplet loading or number density is too great for all individual droplets to experience the same heat transfer and evaporation rate. This third failure mechanism is frequently neglected because traditional droplet evaporation or combustion analysis considers only a single droplet instead of a droplet ensemble or cloud that has as droplet density great enough to cool the gases surrounding the droplets. The single droplet evaporation and combustion approach also fails to consider that multi-component crude oil droplets do not simply evaporatively shrink. Instead, they bubble, swell, burst, and

fragment into many smaller droplets [38,39]. For now, each mechanism awaits thorough experimental validation.

Step 3 must be treated with caution, due to potential unquantifiable uncertainty with flame development and droplet conservation. Siddhamshetty *et al.* [26] acknowledge that the chosen model for droplet evaporation has some issues built in, including an assumption that both phases of flow travel at the same velocity and are at the same temperature at given points in the flow. This, combined with the fact that the model was originally for non-reacting flows, means that the evaporation rates (and therefore droplet sizes) of the oil are subject to high margins of uncertainty. This is exacerbated by changing the liquid loading, as more liquid fuel will alter bulk velocity, droplet development, and the flame height. Ideally, any calculation of the droplet evaporation should take into account the fraction of liquid present in the flow.

Step 4 makes a conservative assumption that the heat release from the gas phase should be sufficient to evaporate all of the liquid effluent to insure perfect burn efficiency. Though this is a conservative approach, it is not realistic. The reservoir gas and lighter crude oil constituents, which will start diffusing and evaporating as soon as it leaves the wellhead, will burn and the radiative heat transfer will further evaporate more crude oil. The process is highly coupled and another analytical route should be considered in the future.

There is a final, but more important, problem with the approach adopted by Siddhamshetty *et al.* [26] that engineers, policy makers, and policy enforcers should note: there is an assumption that the WCD will produce the worst-case spill scenario. Our discussion below shows that these two scenarios should be considered distinct. The referenced correlations show that for a constant GOR, if the total flow rate decreases, then entrainment fraction will also decrease, the annular liquid film thickness will increase, and the peripheral droplet diameters will increase to much larger diameters than those at the core of the flow. The residence time of the larger droplets within the plume cannot be assumed to be long enough to evaporate and burn, whether they remain entrained in the plume or not [30-33].

Policy Versus Potential Hazard

Within the United States, laws and agency policies define WCD. The source for federal policy is U.S. 30 CFR § 254.26, which requires an oil spill response plan (OSRP) to accommodate the largest potential volume of a spill. Individual U.S. federal and state agencies then interpret that definition to apply to their jurisdictional spaces, from which policy is developed. For the example of an oil pipeline, tanker, or liquid tank farm, the WCD will create a large surface slick. A two-phase wellhead WCD with sufficiently high GOR and pressure, in contrast, will probably only create a slick if the wellhead is not ignited, as Sidhamshetty *et al.* described [26].

OBJECTIVE

The objective of this program is to develop and validate computational fluid dynamic models for predicting of wellhead burn efficiency. This requires a detailed understanding of the fundamental gas and liquid fluid mechanics; droplet formation, convection, and evaporation; and the spray combustion behavior of crude oil relevant to wellhead conditions.

Throughout this program, we have written a number of conference papers and the research is at a state of maturity that we are also writing peer-reviewed journal articles. Though we will not repeat content that is currently in journal papers, we will include content similar to what was included in conference papers because that research was not as mature.

APPROACH

This program was divided into two principle efforts. The first was the development of a computational model that captured, with as much fidelity as possible, the multi-phase mechanics, energy transport, chemical species transport, and chemical reaction dynamics. Because there are gaps in what is known about the actual flows and a need to validate computational predictions, the second effort was to develop a body of experimental data and knowledge beyond what was available in the literature. In order to place this work into the context of real petroleum reservoirs, a hypothetical set of conditions will be proposed from which we will conduct analysis, described in the following section entitled "Reservoir and Wellhead Considerations". These conditions will then be used to conduct preliminary analysis using correlations from the literature to identify conditions with potentially poor burn efficiency. The following two sections will be divided into Computational Development and Experimental Validation, which will predict and examine the critical behavior that drives wellhead burn efficiency.

RESERVOIR AND WELLHEAD CONSIDERATIONS

Before we explore the phenomena associated with wellhead blowout combustion, it is essential that we define the flow rate range that we will use for analysis and predictions. On the high end of the flow rates, we will consider the WCD conditions used by and Siddhamshetty et al. [26] in consideration of the Liberty Project [27-29,40]. The associated WCD flow rates and GOR are listed in Table 1.Hasan and Kwon [25] and Sidhamshetty et al. [26] in consideration of the Liberty Project [27-29,40]. The associated WCD flow rates and GOR are listed in Table 1.

Table 1-The predicted maximum well and flow conditions for WCD of the Liberty Project [27-29]. Values are in SI units and in industry-standard units. Oil properties are from Ref. [29], which were in comparison to Endicott properties, which can be found at Refs. [41,42].

Peak WCD Condition		Crude Oil	Reservoir Gas
Parameter	(Unit)	Crude Oil	Reservoir Gas
Flow	(m^3/s)	0.168	26.1
	(bbl/day)	91,200	-
	(scf/day)	-	7.95×10^7
GOR	(m^3/m^3)	155	
	(scf/bbl)	872	
Exit Temp.	(K)	366	
	(°F)	199	
API (°)		24-27	-
Density (kg/m^3)		900	0.663
Viscosity (Pa·s@298 K)		0.0762	
	(Pa·s@366 K)	0.0254	1.33×10^{-5}
Surface Tension	(N/m)	0.019	-
Pipe Diameter	(mm)	216	
Superficial Reynolds Number		8.2×10^5	7.7×10^6

The peak Liberty WCD flow conditions provide the quantitative ceiling to our study and provide insight into the orders of magnitude of the flows we need to consider. Such potentially high oil and gas flow rates are typical for some new wells, though the maximum gas or oil flow rate will vary significantly between wells and reservoirs. Once a reservoir starts producing gas and oil, the reservoir pressure decreases

and the maximum potential flow rates also decrease. Therefore, our solution space needs to consider that either the gas or the oil flow rate may be any value between zero to values similar to those in Table 1, depending on the well depth, reservoir, and other engineering details.

Even for a new spill, the WCD flow rates will vary once a wellhead has been compromised. Rastegar [40] performed wellhead WCD flow predictions for the Liberty project reservoir and revealed the time-dependent nature of the wellhead effluent, shown in Figure 1. We can see that the gas flow rate decreases and then increases while the liquid flow rate decreases over time. Later analysis will examine how the shifts in gas-oil ratio (GOR) influence the spray and combustion behavior. The conditions plotted in Figure 1 provide an additional, realistic set of conditions for analysis and will be used for discussing different physical or chemical processes of wellhead burning.

The thermophysical properties of the oil and gas depends upon the temperature and pressure in the reservoir, which can vary widely. Most oil assays report properties at 298 K, while the estimated Liberty wellhead temperature is 366 K. Since our objective is not to represent a single case but the broader solution space, we will make some assumptions and estimations. We will assume that the viscosity is roughly that of Endicott's reservoir conditions of 1.09 cP [42], and that the surface tension is equal to n-decane at the same temperature: 0.019 N/m [43]. For gas properties, we will assume those of methane, since the bulk of the gas from reservoirs with both oil and gas is methane [43]. These will provide order-of-magnitude ranges from which we can calculate predictions and draw conclusions.

We will constrain our discussion to flow out of a circular exit. It is not unknown for wellhead blowouts to occur out of an annular exit if the blowout occurs between the casing and tubing, but for simplicity we will not review that research.
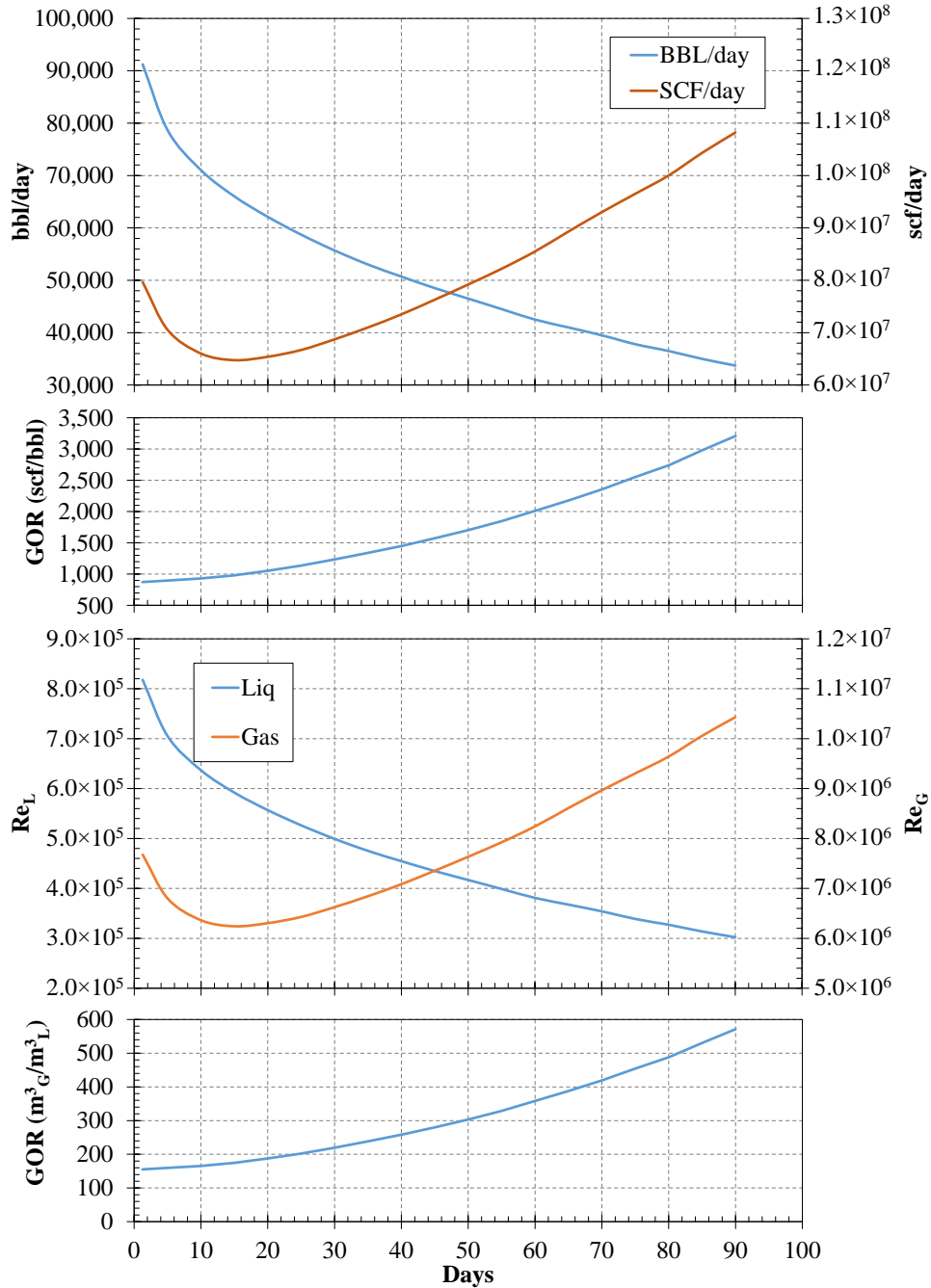
Fig. 1-Change in predicted WCD flow rates and GOR over the first 90 days of a wellhead release from the Liberty Project reservoir in dimensional and dimensionless format.

WELLHEAD FLOW REVIEW AND ANALYSIS

There are broad ranges of topics we can examine when considering the various behaviors observed during a wellhead fire, as discussed in Refs. [6-23]. Among them are the fluid mechanics and gas phase combustion of the gas phase flow behavior, as well as the various aspects of the two-phase behavior. These include the wellbore flow, wellhead ejection, and the two-phase combustion behavior. A full examination

of these behaviors will not be included in this report. Instead, those and additional topics will be included in a literature review, which is also summarized in a conference report [44]. It is sufficient to briefly examine two-phase wellbore and wellhead ejection behavior, since these create the conditions in which computational and experimental investigation have been conducted.

Wellbore Flow

One of the most important questions we need to consider for a wellhead blowout is how the two-phase wellbore flow will influence the wellhead ejection behavior and the resulting two-phase flow structure of the spray plume. The liquid and gas dynamics of the pipe, wellhead, and plume flows are a result of the change in phase between the reservoir and the wellhead, the resulting high-speed pipe flows, and the expansion of the pressurized plume. In the reservoir, the gas is frequently at supercritical pressures and temperatures so that the reservoir gas and crude oil are in solution. As they flow up through the reservoir riser or wellbore, the decreasing pressure allows the gases to evaporate, but since the distance between the reservoir and the wellhead is so long, it is reasonable to assume that the flow behavior is in equilibrium and fully developed at any point upstream of the exit plane.

In the process, these flows can exhibit specific patterns, depending on the liquid-to-gas ratio, pipe angle, and liquid properties. Understanding and predicting these behaviors, their characteristics, and their regime margins is an ongoing research topic that is relevant to a wide range of chemical transportation and processing applications [31,45-48]. For this paper, we will constrain our discussion to vertical pipes or channels. To understand these patterns, it is constructive to go back to the model of the fluid rising up from a reservoir. As the fluid rises and the static pressure reduces, small bubbles will form in the flow. This regime is called, understandably, bubbly flow. As the bubbles increase in size, they agglomerate such that the flow forms axially distinct regions of gas and liquid in the flow, forming the pattern referred to as slug flow. As the gas fraction increases, the distinct sections begin to mix and collapse upon one another to form churn flow. Eventually, the gas volumetric flow rate becomes large enough to form a contiguous flow at the center of the flow. The remaining liquid initially forms an annulus at the wellbore wall that is sheared by the gas flow to form droplets that deposit and are sheared again in steady, dynamic equilibrium; this flow patter is referred to as annular flow. Finally, with sufficient gas flow increase and distance, nearly all of the liquid will be entrained except for a very small fraction that forms a thin film in the pipe. In this mist regime, droplets will continually impinge, coalesce into films, and then be sheared to form new droplets, but the film is thin enough to be negligible. Subsequent discussion of annular flow will refer to this film and droplet flow regime in a cylindrical pipe.

The difficulty in predicting these transitions was discussed in the textbook by Hasan and Kabir [49] after reviewing a number of different regime maps, boundary criteria, and applications from a range of authors. They noted that each regime shift is accompanied by a shift in the fluid mechanic behavior and highlighted that the wellbore pressure influence on the separation of the gas and liquid has considerable influence. In the same chapter, Hasan and Kabir [49] review some of the latest research in these flow transitions and discuss how to predict them.

We can assume that for an annular flow regime, the ejected flow will form a spray plume, but it is unclear what kind of flow structures form when bubbly, plug, or churn flows are expelled through a wellhead. It is reasonable to assume that these lower velocity flows are more likely to form pools or fountains than well-atomized sprays. Therefore, for the sake of brevity and applicability, we will focus on the annular-mist flow behavior. The dominant behavior of annular-mist flow is the interaction between the liquid annular film and the core gas, which drives annular flow characteristics such as the film thickness, liquid entrainment fraction, and the instability waves that form at the gas-liquid interface that are sheared off to form ligaments, which then break apart into droplets and are entrained into the gas flow. The higher velocity gas convects the droplets axially, while the three-dimensional, unsteady turbulence convects them transversely until some of them eventually collide back against the film and wellbore wall to start the

process over again. Once ejected, the annular film thickness will directly influence the droplet diameter distribution of the annular spray region [32,33] while the liquid entrainment fraction will directly influence how much liquid ends up in that annular spray region or as fine droplets in the central core of the flow. If the gas flow rate is sufficiently large to entrain all of the liquid, the film thickness will be negligible and the only droplets that are of concern will be those that were formed in the wellbore. A thorough treatment is too large to be contained in this paper and would significantly distract from the main ideas we wish to express. Therefore, we will focus on three, measureable annular flow parameters that have the greatest influence on the wellhead spray: film thickness, entrainment, and droplet diameter.

Film Thickness and Instability

The liquid film thickness, δ, is an average thickness with the presence of surface waves and other perturbations. This metric that has been often overlooked in consideration to wellhead blowouts even though the film will drive the formation of much larger droplets upon ejection than the entrained droplets at the center of the flow [32,33]. A recent review of droplet entrainment behaviors by Berna *et al.* [31] describes the two-phase flow regimes for horizontal and vertical pipes, liquid wave behavior and characteristic metrics, and the significant research in correlating these metrics to dimensionless flow numbers. Typical dimensionless numbers for these correlations incorporate the pipe diameter (D), density (ρ), and viscosity (μ) with subscripts corresponding to the liquid (L) and gas (G), respectively. The superficial Reynolds numbers, Re, liquid-gas interface Weber number, We_G, and Froude numbers, Fr, number are expressed by

$$Re_G = \frac{\rho_G D U_{G,S}}{\mu_G} \tag{1a}$$

$$Re_L = \frac{\rho_L D U_{L,S}}{\mu_L} \tag{1b}$$

$$We_G = \frac{\rho_G D U_{G,S}^2}{\sigma_L} \tag{1c}$$

$$Fr_G = \frac{U_{G,S}}{\sqrt{gD}} \tag{1d}$$

$$Fr_L = \frac{U_{L,S}}{\sqrt{gD}} \tag{1e}$$

where the superficial gas and liquid velocities ($U_{G,S}$ and $U_{L,S}$) are calculated as if only the gas or liquid are flowing through the pipe as plug flow. The surface tension, σ_L, is for the liquid-gas interface.

Berna *et al.* [31] expressed their correlation for film thickness as

$$\delta/D = 7.165 \cdot Re_G^{-1.07} Re_L^{0.48} \left(\frac{Fr_G}{Fr_L}\right)^{0.24} \tag{2}$$

after comparing data from Refs. [50-54]. A careful examination of the Froude number ratios reveals that it is simply a superficial velocity ratio. If we assume a constant gas flow of 0.01 to 35.7 m³/s, GORs of 500, 872, and 2000 scf/bbl, calculate the corresponding Re_L range from around 10^2 to near 10^6, then calculate the corresponding d from Equation 2, we create the top plot in Figure 2. The Liberty 90 day WCD range corresponds to $3.0 \times 10^5 \leq Re_L \leq 8.2 \times 10^5$, which was highlighted green in Figure 2.

Figure 2 suggests a number of significant behaviors and implications that should be noted. First, there is the general, predictable trend that increasing the Re_L or the GOR decreases the film thickness, which we expect from Equation 2. Most importantly, the plots of film thickness show that for much of the range of Re_L, if droplets are formed with diameters on the same order of magnitude as δ, it is not clear if those droplets would be entrained and have sufficient residence time to evaporate and burn or eventually fall out
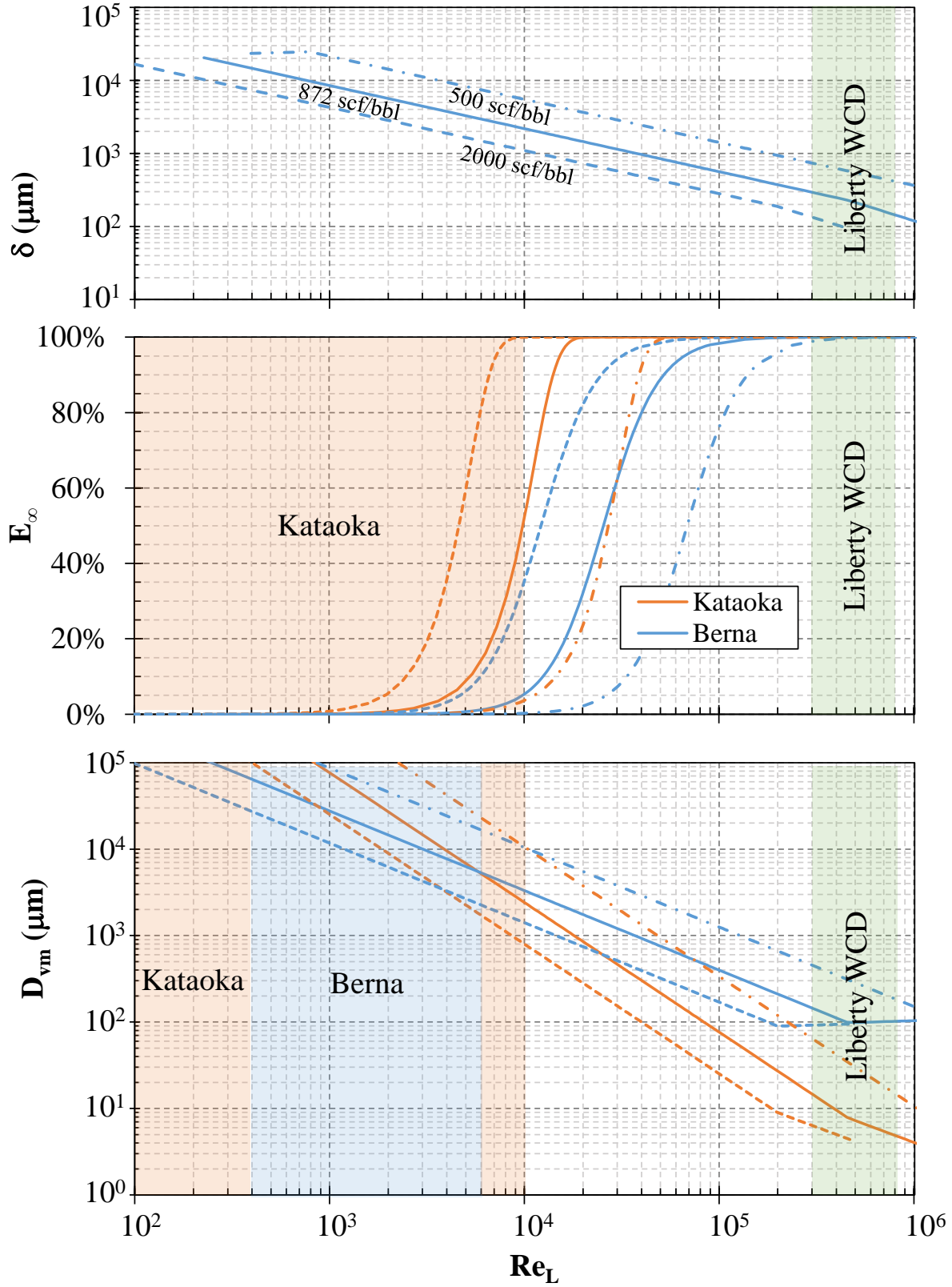
Fig. 2-Plotted δ, E_∞, and D_{vm} for a range of Re_L, for 500, 872, and 2000 scf/bbl (51, 155, and 356 m_{gas}^3/m_{oil}^3), with the first 90 days of Liberty WCD highlighted green. The validated range of the Kataoka *et al.* correlation shown highlighted orange and the validated range of Berna *et al.* is highlighted blue.

12

of the plume. The δ plots bring up some fundamental question for wellhead burning: what happens to the film once it is ejected from the wellhead? How does the film thickness influence the droplet formation process and whether those droplets will evaporate and burn? We will consider these questions in the sections discussing our measurements from *Phase Doppler Anemometry* and *Diffuse Back-Illumination Imaging*.

Liquid Entrainment

Recent entrainment correlations, set forth in Refs. [25,26] from both Kataoka *et al.* [30] and Berna *et al.* [35], have been referenced in recent industry and government reports [55]. The correlations within these two papers provide a broad set of mathematical relations that describe entrainment, the axial distance required for quasi-equilibrium, and the distance required for full entrainment. Entrainment is defined as the fraction of the total liquid mass that is entrained into the gas flow in the form of droplets.

In general, we will denote entrainment as E at an arbitrary location, denoted by the axial distance z, whether non-equilibrium or equilibrium. We will denote the quasi-equilibrium entrainment by E_∞ and the corresponding length required for quasi-equilibrium as z_∞. From Kataoka *et al.* [30], we have the correlation for entrainment:

$$E_\infty = tanh\left(7.25 \times 10^{-7} We_{G,E}^{1.25} Re_L^{0.25}\right) \tag{3}$$

$$273 \le Re_L \le 5041$$

$$1414 \le We_{G,E} \le 9602$$

based on the data of Cousins and Hewitt [51] and Gill *et al.* [56]. Equation 3, with its dimensionless numbers, incorporates the momentum of the gas ($We_{G,E}$) and that of the liquid (Re_L). We should note that the entrainment Weber number, $We_{G,E}$, is not the same as defined in Equation 1c, but by the expression:

$$We_{G,E} = \frac{\rho_G D U_{G,S}^2}{\sigma_L}\left(\frac{\rho_L - \rho_G}{\rho_G}\right)^{1/3} \tag{4}$$

There are a number of other critical expressions that we should relate from Kataoka *et al.* [30]:

$$z_\infty = \frac{440 D We_{G,E}^{0.25}}{Re_L^{0.5}} \tag{5a}$$

$$\zeta = \frac{z \, Re_L^{0.5}}{D We_{G,E}^{0.25}} \tag{5b}$$

$$E_z = [1 - exp(-1.87 \times 10^{-5}\zeta^2)]E_\infty \tag{5c}$$

where z_∞ is the quasi-equilibrium entry length, z is an arbitrary entry length less than z_∞, ζ is the normalized entry length, and E_z is the entrainment fraction corresponding to z. Curiously, none of the entrainment correlations from Kataoka *et al.* [30] involve Re_G. Instead, $We_{G,E}$ accounts for the gas momentum.

Berna *et al.* [35], after reviewing correlations and data from various sources, developed their own correlation for entrainment with the expression:

$$\frac{E_\infty}{1-E_\infty} = 5.51 \times 10^{-7} We_G^{2.68} Re_G^{-2.68} Re_L^{0.34}\left(\frac{\rho_G}{\rho_L}\right)^{-0.37}\left(\frac{\mu_G}{\mu_L}\right)^{-3.71} C_W^{4.24} \tag{6}$$

Equation 6 has an additional term, C_W, that accounts for the surface tension effect on wave circulation and dissipation [57] and was defined by the expressions:

$$C_W = 0.028N_\mu^{-4/5} \ for \ N_\mu \leq 1/15 \tag{7}$$

where N_μ is a viscosity number that considers the density, buoyancy, and surface tension [58]. We note that the fit to the included data was not very good, with an R^2 of 0.66, but they considered data from both vertical and horizontal pipes, which have some fundamental differences. We also had difficulty finding relevant validation bounds for the different parameters of the correlation. Finally, the Berna *et al.* [35,36] developments did not discuss quasi-equilibrium length nor how their correlation should be corrected for shorter lengths. Though this is fine for wellhead calculations where the pipe can be assumed to be much greater than z_∞, we need to account for smaller approach lengths for practical experimental apparatuses.

Figure 2, middle, shows a plot comparing the entrainment predictions for the Kataoka and Berna correlations for a range of Re_L and three different values of GOR. The most significant aspect of the plot is that the 30-day period of the example Liberty WCD is 100% entrained. Increasing the GOR correspondingly increases the entrainment, while decreasing the GOR also decreases entrainment, as we might expect. In Figure 2, we notice that even with full entrainment, the film thickness is significant large enough, if that same film distance were to develop into a droplet diameter, those droplets may not evaporate and burn if they are convected to the outer edges of the gas-air shear layer, and thus may fall to the ground.

Droplet Diameter

The droplet correlations referenced in Siddhamshetty *et al.* [26] were those developed by Kataoka *et al.* [34] and a later correlation was developed Berna *et al.* [35] that accounts for higher pressures. The Kataoka *et al.* [34] correlation is expressed as:

$$\frac{D_{vm}}{D} = 0.01 \cdot We_G^{-1} Re_L^{-\frac{1}{6}} Re_G^{\frac{2}{3}} \left(\frac{\rho_G}{\rho_L}\right)^{-\frac{1}{3}} \left(\frac{\mu_G}{\mu_L}\right)^{\frac{2}{3}} \tag{8}$$

100 ≤ Re_L ≤ 9700
2.5 ≤ Re_G × 10^{-4} ≤ 17
1 atm ≤ P ≤ 2 atm

where D_{vm} is the volume median diameter, normalized by *D*.

Berna *et al.* [35] developed another correlation from data published by Lopes [59], Fore *et al.* [60], and Cousins and Hewitt [51]. The vertical droplet diameter correlation is similar to Equation 8 and uses the same variables, but takes on the form:

$$\frac{D_{vm}}{D} = 0.11 \cdot We_G^{-0.68} Re_L^{0.11} Re_G^{0.33} \left(\frac{\rho_G}{\rho_L}\right)^{0.31} \tag{9}$$

390 ≤ Re_L ≤ 6500
1.3 ≤ Re_G × 10^{-4} ≤ 12
1 atm ≤ p ≤ 18 atm

The plots in Figure 2, bottom, reveal a number of behaviors that should be considered in the context of wellhead flows. First, the Liberty worst-case discharge conditions, over the first 90 days of a free-flowing wellhead, are far outside of the validated range for both correlations. Therefore, we can expect that the trends are qualitatively accurate, but we cannot use those droplet diameters to make quantitative burn efficiency predictions. The extrapolated trend for the Liberty WCD conditions suggests that the droplet diameters are in the range between 10 and 100 μm. Though this is a wide range and unsubstantiated from the data cited by Kataoka *et al.* [34] and Berna *et al.* [36], the correlations (Equations 8 and 9) predict that

the droplet diameters should generally decrease as We_G, Re_L, and Re_G increase, since the liquid-gas interface shear, which drives droplet formation, would correspondingly increase to form smaller droplets. Such trends are similar for the film thickness (Equation 2) and entrainment fractions (Equations 3 and 6).

We should clarify an important caveat so that our plots are not misused or misinterpreted in the future. We note from Figure 1 that the GOR does NOT remain constant. Therefore, investigators should not look at one of the plots in Figure 2 and assume that they can trace a curve to lower values of Re_L to approximate shifts in film thickness, entrainment fraction, or droplet diameter. Such an approach discounts the variation in GOR that will occur for a wellhead blowout. Therefore, engineers should take reservoir predictions, such as plotted in Figure 1, and use these referenced correlations to predict how the flow behavior will change, as we have plotted in Figure 3, which show the calculated δ, E_∞, and D_{vm} over the first 90 days of a blowout. We should note that with the gradual decrease and then increase of the gas flow rate, δ increases and then decreases. Simultaneously, E_∞ remains at 100%, as we expect, for both the Berna and Kataoka correlations. The entrained droplet diameters remain nearly constant, but there is variation in time and with the different correlations.
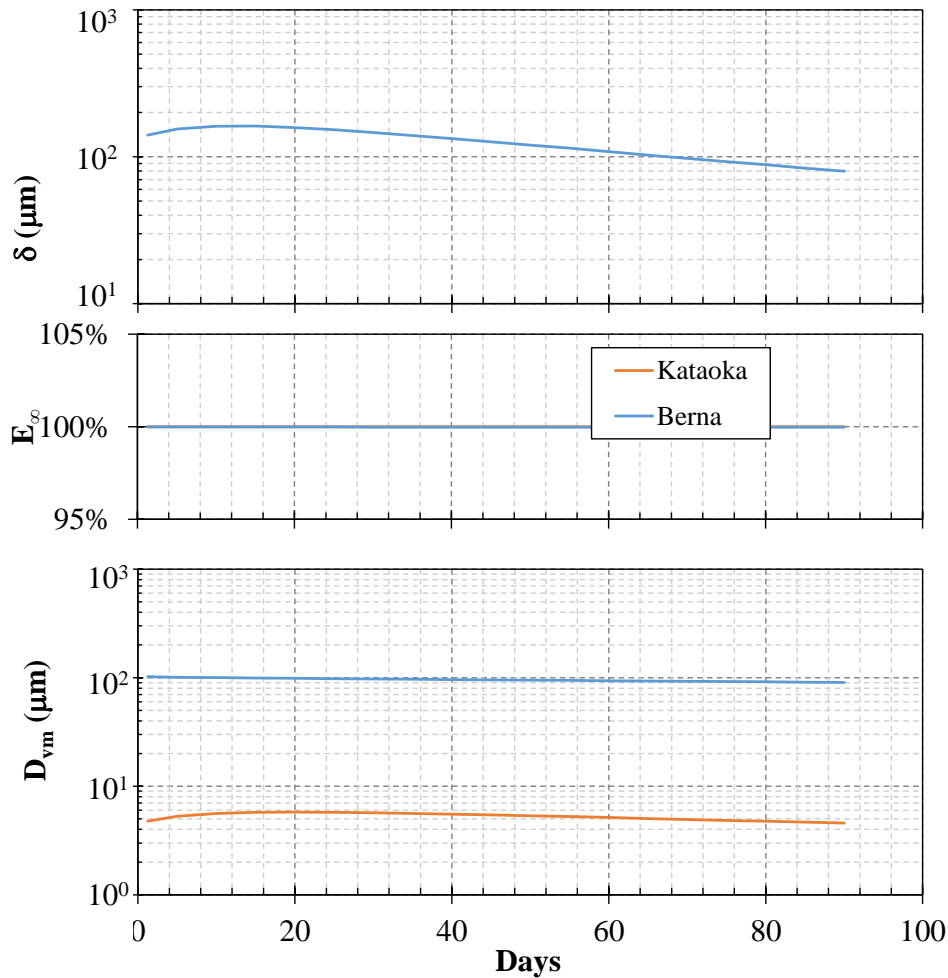
Fig. 3-Plotted δ, E_∞, and D_{vm} as a function of the WCD flow rates plotted in Fig. 1 for the first 90 days of Liberty WCD.

Wellhead Ejection

Upon exiting the wellhead, the two-phase flow behavior shifts dramatically and the resulting behavior, whether a spray, fountain, or pool, again depends on the GOR and the flow rates of the respective liquid and gas. For churn, plug, or bubble flow, Siddhamshetty *et al.* [26] assumed that the flow would have poor atomization and thus poor burn efficiency. The most analogous atomization process for such regimes is that of effervescent sprays, which depend on a large pressure gradient across the exit plane [61-66]. Researchers have examined these sprays from a number of contexts and for a range of applications, but we will not explore them fully in this study. For this work, we have focused on annular and/or misty flows.

Assuming annular flow, Figure 4 shows how the crude oil and well gas form a flame and diagrams the potential products that are formed. There are two potential fates of the oil: *oleum evanescet* and *oleum ruinam*. The disappeared oil, *oleum evanescet*, completely burns into gaseous products (CO_2, CO, H_2O, SO_x, NO_x and unburned hydrocarbon vapor) and soot that is carried away by the atmosphere. The residue and oil that falls upon the ground, *oleum ruinam*, is composed of soot agglomerates and droplets ranging from those partially evaporated or burned to large droplets splattered close to the wellhead [6-8].

The atomization process for annular flow is best understood in the context of the geometry upstream of the wellhead. It is composed of a central core of gas, surrounded by an annular film of liquid, on the inside of the pipe that the wellbore pressure expels out, through the wellhead. The entrained droplets do not undergo any immediate

Fig. 4-Diagram of wellhead spray combustion behavior and the fate of the two-phase fuels.

changes unless there are shock structures present [67], while the expelled annular film is sheared into ligaments, which eventually break up to form droplets; a common process in almost all atomizing systems [68,69]. The droplet formation process of an annular film is of interest because of its applicability to gas-turbine spray combustion and other air- or gas-assisted atomization processes [70-74]. Unfortunately, these studies employ much shorter development lengths than those of a wellbore. In response, we have developed an atomizer to examine these sprays in the laboratory (see Fisher *et al.* [32,33]), which mimics the wellbore atomization process. This open-pipe atomizer (OPA) allows both the gas and liquid to develop to quasi-equilibrium because of the large length-to-diameter ratio and allows the examination of droplet formation, transport, evaporation, and combustion.

Recent work reported by Fisher *et al.* [32,33], which we will cover in the results of the bench-scale *Phase Doppler Anemometry* and *Diffuse Back-Illumination Imaging* measurements, examined aspects of annular flow-driven open pipe atomization. Both studies were based on laboratory flows using ethane and heptane as gaseous and liquid fuels, respectively. Using phase Doppler anemometry and high-speed diffuse back-illumination (HS-DBI) imaging [75-78], they discovered that the spray plume from an annular flow

16

produced two distinct spray regions: an inner core of high-speed, small droplets and an outer region of relatively slower, larger droplets formed by the shear of the annular film.

More recent, unpublished work by this group is examining the droplet formation process using HS-DBI of the exit of the open-pipe atomizer to examine the details of the annular film ejection and droplet formation process. Figure 5 shows a diffuse back-illumination [75] image of spray issuing from an OPA to produce an annular, two-phase flow, similar to that by Fisher *et al*. [32,33]. At the base and in the outer regions of both plumes, where the film is ejected from the OPA, there is a region of large ligament formation, stretching, and pinching to form droplets much larger than those at the center of the flow, which were formed by entrainment before the flow exited the atomizer. This non-uniformity persists downstream to form a central region of high-speed droplets.

In contrast to the correlations and plots shown in the *Wellbore Flow* section, researchers have not developed droplet diameter and spatial distribution correlations for the wide range of possible flow velocities. This is especially important since the flow is constrained within the wellbore to be less than or equal to the speed of sound. Once the flow exits, it can expand and accelerate to velocities beyond sonic. The compressible flow behavior presents a number of complications that warrant further examination. That discussion and additional discussion of and droplet entrainment, suspension, and fallout are included in the literature review.
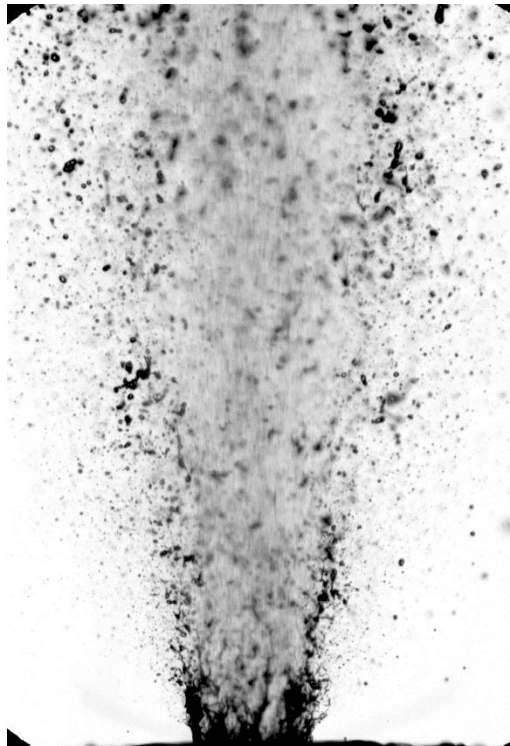
Fig. 5-Diffuse imageback-illumination imaging of spray from annular flow out of a laboratory-scale (D=0.84 mm), OPA described by Fisher *et al*. [32,33]. The image is approximately 4.6 mm wide by 6.7 mm high. The flow rates were 0.4 g/s of air and 0.8 g/s of water. This flow had a GOR of 228 m_{air}^3/m_{water}^3.

COMPUTATIONAL DEVELOPMENT

Theoretical Development

Overview of the Multi-Phase Simulation Framework

In this work, we describe the development of a physical model suitable for simulating field-scale in-situ oil wellhead burning scenarios. Such wellhead fires are driven by a diverse set of tightly coupled physical processes, including compressible reacting turbulent gas flows, liquid droplet dynamics and phase change, and radiative heat transfer between phases and to the ambient environment. Due to the sheer size of the discharge jet and the resulting flame plume, it is not possible to simulate this multi-physics flow problem, which ultimately dictates the overall burning efficiency of the in-situ burning event, from first principles. Instead, a number of modeling assumptions must be made that will bring down the overall computational cost of the simulations. These assumptions and the corresponding governing equations will be laid out in the ensuing subsections.

The primary modeling choice to be made is how to couple the secondary (liquid droplet) phase to the gas-phase flow field. Two options exist: (1) treat the secondary phase as a continuous media and utilize specialized models for the transport or mass, momentum, and energy between phases and (2) treat the secondary phase as a collection of discrete droplets, whose individual mass, momentum, and energy are tracked explicitly based on the local gas-phase conditions and modify the gas-phase flow through source terms that represent the collective behavior as averages of the individual droplet behaviors. We refer to the first approach as the Eulerian-Eulerian (EE) model and the second approach as the Eulerian-Lagrangian (EL) model. There is a trade between cost and accuracy when considering these two models. The EE model is more cost-effective, but the accuracy of the droplet-gas interaction models can be low when the energy and mass exchange becomes complex. The EL model, on the other hand, allows for a more detailed description of the droplet physics but comes at a higher computational cost. In this work, we utilize the EL model to build a higher-fidelity representation of the multiphase flame behaviors.

Gas-Phase Model

The gas-phase flow is modeled using the Favre-averaged reacting Reynolds-Averaged Navier-Stokes equations for which the mixture density ρ, momentum $\rho\boldsymbol{u}$, and total enthalpy ρH are governed by

$$\frac{\partial \rho}{\partial t} + \nabla \cdot \rho\boldsymbol{u} = S_{D,m} \tag{10a}$$

$$\frac{\partial}{\partial t}(\rho\boldsymbol{u}) + \nabla \cdot (\rho\boldsymbol{u}\boldsymbol{u}) = -\nabla P + \nabla \cdot \left[\mu\left(\nabla\boldsymbol{u} + \nabla\boldsymbol{u}^T - \frac{2}{3}\nabla \cdot \boldsymbol{u}\right)\right] + \nabla \cdot (-\rho\overline{\boldsymbol{u}'\boldsymbol{u}'}) + S_{D,mom} \tag{10b}$$

$$\frac{\partial}{\partial t}(\rho\overline{H}) + \nabla \cdot (\rho\boldsymbol{u}\overline{H}) = \nabla \cdot \left(\left(\frac{k_t}{C_p}\right)\nabla\overline{H}\right) + S_h + S_{D,H} \tag{10c}$$

where bold variables are vector quantities and the Reynolds stresses,

$$-\rho\overline{\boldsymbol{u}'\boldsymbol{u}'} = \mu_t\left(\nabla\boldsymbol{u} + \nabla\boldsymbol{u}^T\right) - \frac{2}{3}(\rho k + \mu_t\nabla \cdot \boldsymbol{u}) \tag{10d}$$

are modeled using the realizable $k - \varepsilon$ model,

$$\frac{\partial}{\partial t}(\rho k) + \nabla \cdot (\rho k\boldsymbol{u}) = \nabla \cdot \left[\left(\mu + \frac{\mu_t}{\sigma_k}\right)\nabla k\right] + G_k - \rho\varepsilon - Y_M \tag{10e}$$

$$\frac{\partial}{\partial t}(\rho\varepsilon) + \nabla \cdot (\rho\varepsilon\boldsymbol{u}) = \nabla \cdot \left[\left(\mu + \frac{\mu_t}{\sigma_\varepsilon}\right)\nabla\varepsilon\right] + \rho C_1 S\varepsilon - \rho C_2 \frac{\varepsilon^2}{k+\sqrt{\nu\varepsilon}} \tag{10f}$$

The production of turbulent kinetic energy k is given by $G_k = \mu_t S^2$, where $S \equiv \sqrt{2S_{ij}S_{ij}}$ is the modulus of the mean rate of strain tensor, $S_{ij} = \frac{1}{2}\left(\frac{\partial u_j}{\partial x_i} + \frac{\partial u_i}{\partial x_j}\right)$. The turbulent viscosity μ_t is defined as

$$\mu_t = \rho C_\mu \frac{k^2}{\varepsilon} \tag{11a}$$

where the model parameter C_μ varies with S_{ij} and the mean rate-of-rotation tensor $\bar{\Omega}_{ij}$ according to

$$C_\mu = 1/\left(A_0 + A_S \frac{kU^*}{\varepsilon}\right) \tag{11b}$$

where

$$U^* = \sqrt{S_{ij}S_{ij} + \bar{\Omega}_{ij}\bar{\Omega}_{ij}} \tag{11c}$$

$$A_S = \sqrt{6}\cos\phi \tag{11d}$$

$$\phi = \frac{1}{3}\cos^{-1}\left(\sqrt{6}\frac{S_{ij}S_{jk}S_{ki}}{\tilde{S}^3}\right) \tag{11e}$$

Turbulent Flame Model

The turbulent flame brush is modeled as a partially-premixed flame that is in chemical equilibrium throughout both premixed and non-premixed reaction zones. Here, we parameterize the premixed flame using a single reaction progress variable,

$$c = \sum_k \alpha_k(Y_k - Y_k^u)/\sum_k \alpha_k\left(Y_k^{eq} - Y_k^u\right) \tag{12a}$$

for which we utilize CO and CO_2 as tracer species, such that α_{CO} and α_{CO_2} are taken to be unity and α_k for all other species is set to zero. The non-premixed combustion is characterized by two mixture fractions $f_1 = (Z_i - Z_{i,ox})/(Z_{i,wg} - Z_{i,ox})$ and $f_2 = (Z_i - Z_{i,ox})/(Z_{i,os} - Z_{i,ox})$, for which the Z_i are the conserved atomic mass fractions of the elements present in the well gases (subscript "wg"), oil surrogate ("os"), and oxidizer ("ox") streams. Assuming the net mass diffusivities of the fuel and oxidizer species are equal, a reasonable assumption in highly turbulent flows, there exist unique values of f_1 and f_2, representing the degree of mixing between the primary and secondary fuel streams and the oxidizer stream. The species mass fractions and temperature can then be uniquely determined based on the values of f_1, f_2, c, and the mean flow enthalpy $\bar{H}$. These quantities are computed *a priori* and tabulated, assuming the reactions proceed to chemical equilibrium. Mean values for the temperature and mass fractions throughout the turbulent flame brush are computed according to

$$\bar{\phi}_i = \int_0^1 \phi_i(f_1, f_2, c, \bar{H})p(f_1, f_2, c, \bar{H})df_1 df_2 \, dc \, d\bar{H} \tag{13}$$

where the joint probability density function (pdf) $p(f_1, f_2, c, \bar{H})$ is taken to be the product of the four independent pdf's for f_1, f_2, c, and $\bar{H}$. We model $p(\bar{H})$ as a delta function and $p(f_i)$ and $p(c)$ as assumed-shape beta functions that depend on the mean value $\bar{Q}$ and its variance $\overline{Q'^2}$. We solve transport equations for the mean and variance of $\bar{f}_i$ and the mean of the progress variable $\bar{c}$,

$$\frac{\partial}{\partial t}(\rho\bar{f}_i) + \nabla(\rho\boldsymbol{u}\bar{f}_i) = \nabla \cdot \left(\left(\frac{k}{C_p} + \frac{\mu_t}{\sigma_l}\right)\nabla\bar{f}_i\right) + S_{Df_i} \tag{14a}$$

$$\frac{\partial}{\partial t}\left(\rho\overline{f'^2}\right) + \nabla\left(\rho\boldsymbol{u}\overline{f'^2}\right) = \nabla\cdot\left(\left(\frac{k}{C_p}+\frac{\mu_t}{\sigma_l}\right)\nabla\overline{f'^2}\right) + C_g\mu_t\left(\nabla\overline{f'^2}\right) - C_d\frac{\epsilon}{k}\overline{f'^2} \tag{14b}$$

$$\frac{\partial}{\partial t}(\rho\bar{c}) + \nabla\cdot(\rho\bar{c}\boldsymbol{u}) = \nabla\cdot\left[\left(\frac{k}{c_p}+\frac{\mu_t}{Sc_t}\right)\nabla\bar{c}\right] + \rho S_c \tag{14c}$$

The source term in equation 14c is defined by $\rho S_c = \rho_u U_l \Sigma$, where ρ_u is the density of the unburned gas mixture and U_l is the laminar flame speed and Σ is the flame surface density, which is computed using the extended coherent flamelet model,

$$\frac{\partial\Sigma}{\partial t} + \nabla\cdot(\boldsymbol{u}\Sigma) = \nabla\cdot\left(\left[\frac{k}{C_p}+\frac{\mu_t}{Sc_t}\right]\nabla\left(\frac{\Sigma}{\rho}\right)\right) + (P_1+P_2+P_3)\Sigma + P_4 - D \tag{15}$$

We use the models developed by Veynante and Vervisch [79] for the source terms due to turbulence interaction P_1, dilation in the flame P_2, expansion of burned gases P_3, normal flame propagation P_4, and the dissipation of flame area term D. The reader is referred to the cited publication for a full description of the closure models and associated model constants.

The laminar flame speed is computed dynamically based on the local temperature and mixture equivalence ratio. Flame speed correlations for the wide variety of mixtures of well gases and volatile oil species over the range of physical conditions encountered at the wellhead are not generally available. As a first approximation, the laminar flame speed can be estimated using correlations for more generic hydrocarbons, similar to that proposed by Amirante *et al.* [80] for high-temperature propane-air mixtures. More detailed correlations for well-specific gas mixtures could be built from one-dimensional laminar flame calculations using detailed chemical kinetics mechanisms suitable for heavy hydrocarbons if the need arises in future refinements of this two-phase flame model. Closing the turbulent flame model discussion, the source terms S_{Df_i} are the contributions to the mean mixture fractions from the discrete-phase droplets. Here, S_D is equal to zero for f_1, since the droplets only add mass to the secondary f_2 fuel stream. The source terms are computed as the average contribution over individual grid cells.

Soot Formation and Radiation Models

The turbulent spray flames considered in this study can produce a significant amount of radiative energy due to the presence of the droplets in the flow as well as soot in the flame brush. We compute the incident radiation flux G profile using the P1 radiation model,

$$\nabla\cdot(\Gamma\nabla G) - (a+a_p)G + 4\pi\left(an^2\frac{\sigma_B T^4}{\pi}+E_p\right) = 0 \tag{16}$$

where $\Gamma = 1/[3(a+a_p+\sigma_S)]$, σ_S is the scattering coefficient, σ_B is the Stefan-Boltzmann constant, n is the index of refraction, and $a = a_{gas}+a_{soot}$ is the continuous-phase absorption coefficient. The coefficient for gas-phase absorption a_{gas} is computed using the weighted-sum-of-gray-gases model (WSGGM), which allows the multi-species gas mixture to be broken up into several absorption bands, each with its own absorption coefficient [81].

The soot absorption coefficient depends on the local mass fraction of soot Y_{soot} according to $a_{soot} = b_1\rho_{soot}Y_{soot}[1 + b_T(T - 2000)]$, where b_1 and b_T are model constants. The soot mass fraction is computed using the one-step model of Khan and Greeves [82],

$$\frac{\partial}{\partial t}(\rho Y_{soot}) + \nabla \cdot (\rho \boldsymbol{u} Y_{soot}) = \nabla \cdot \left(\left(\frac{\mu_t}{\sigma_{soot}} \right) \nabla Y_{soot} \right) + \mathcal{R}_{soot} \qquad (17)$$

where $\mathcal{R}_{soot} = \mathcal{R}_{form} - \mathcal{R}_{comb}$ is the net rate of soot generation. The rate of soot formation is modeled using an empirical rate law,

$$\mathcal{R}_{form} = C_s p_{fuel} \phi^r e^{-E/RT} \qquad (18)$$

and the rate of soot combustion is modeled as the minimum of two rate laws,

$$\mathcal{R}_{comb} = min \left[A\rho Y_{soot} \frac{\varepsilon}{k}, A\rho \left(\frac{Y_{ox}}{v_{soot}} \right) \left(\frac{Y_{soot} v_{soot}}{Y_{soot} v_{soot} + Y_{fuel} v_{fuel}} \right) \frac{\varepsilon}{k} \right] \qquad (19)$$

For modeling purposes, we use the heaviest hydrocarbon in the fuel mixture as the fuel and oxygen as the oxidizer from which the stoichiometric coefficient v_{fuel} and local equivalence ratio ϕ are computed. We define p_{fuel} as the partial pressure of the predominant gaseous volatile species originating from the oil droplets and set the modeling constants C_s, v_{soot}, A, and E. As was the case for the laminar flame speed, calibrated model constants for the rate laws specific to the gas-oil mixtures of interest to well-head ignition events are not generally available. As a first approximation, generic model constants specific to smaller hydrocarbon species can be utilitized, such as those described in [80].

The secondary phase couples to the radiation transport equation through the droplet absorption coefficient

$$a_p = \lim_{V \to 0} \sum_{n=1}^{N} \varepsilon_{pn} \frac{A_{pn}}{V} \qquad (20)$$

the droplet scattering coefficient

$$\sigma_p = \lim_{V \to 0} \sum_{n=1}^{N} (1 - f_{pn})(1 - \varepsilon_{pn}) \frac{A_{pn}}{V} \qquad (21)$$

and the droplet emission

$$E_p = \lim_{V \to 0} \sum_{n=1}^{N} \varepsilon_{pn} A_{pn} \frac{\sigma_B T_{pn}^4}{\pi V} \qquad (22)$$

where $A_{pn} = \pi d_{pn}^2 / 4$ is the projected area of the nth droplet of diameter d_p and temperature T_p in a grid cell of volume V, ε_p is the droplet emissivity, and f_p is the droplet scattering factor.

The radiative heat flux couples to the mean enthalpy equation through the source term

$$S_h = -\nabla \cdot \boldsymbol{q}_r = (a + a_p)G - 4\pi \left(an^2 \frac{\sigma_B T^4}{\pi} + E_p \right), \qquad (23)$$

which in turn alters the local temperature and gas-phase species mass fractions based on the probability density functions described in the preceding subsection.

Lagrangian Droplet Dynamics and Thermophysics

We model the liquid fuel droplets as inertial particles that undergo vaporization, boiling, shear-driven breakup, and collision-mediated coalescence and exchange mass, momentum, and energy with the continuous gas-phase. The droplets are assumed to be composed of a single-component liquid that vaporizes according to a convection-diffusion-controlled model,

$$\frac{dm_p}{dt} = k_c A_p \rho \, ln(1 + B_m) \tag{24a}$$

$$B_m = \frac{Y_{i,s} - Y_{i,\infty}}{1 - Y_{i,s}} \tag{24b}$$

where m_p is the mass of the droplet, $Y_{i,s}$ is the vapor mass fraction at the droplet surface, and $Y_{i,\infty}$ is the local vapor mass fraction in the continuous phase. The mass transfer coefficient k_c is computed using a correlation for the Sherwood number, $Sh \equiv k_c d_p / D_{i,m} = 2.0 + 0.6 Re_d^{1/2} Sc^{1/3}$, where d_p is the droplet diameter, $D_{i,m}$ is the diffusion coefficient of the vapor in the bulk gas mixture, Sc is the liquid Schmidt number, and Re_d is the particle Reynolds number. We assume thermodynamic equilibrium at the droplet surface and compute $Y_{i,s}$ using the saturation pressure at the current droplet temperature.

The particle temperature is governed by

$$m_p c_p \frac{dT_p}{dt} = h A_p (T_\infty - T_p) + \varepsilon_p A_p \sigma_B (\theta_R^4 - T_p^4) - \frac{dm_p}{dt} h_{fg} \tag{25}$$

for $T_p < T_{boil}$, where T_∞ is the local gas-phase temperature, $\theta_R = (G/4\sigma)^{1/4}$ is the radiation temperature, h_{fg} is the latent heat of vaporization, c_p is the liquid specific heat, and h is the convective heat transfer coefficient obtained from the Nusselt number correlation:

$$Nu \equiv h d_p / k_\infty = \left(2.0 + 0.6 Re_d^{1/2} Pr^{1/3}\right) ln(1 + B_T)/B_T \tag{26}$$

The Spalding heat transfer coefficient is computed according to

$$B_T = c_{pv}(T_\infty - T_p)/(h_{fg} - \dot{q}_p/\dot{m}_p). \tag{27}$$

When $T_p \geq T_{boil}$, the droplet diameter decreases according to a boiling law

$$\frac{d(d_p)}{dt} = \frac{2}{\rho_p h_{fg}} \left[\frac{2k_\infty(1 + 0.23\sqrt{Re_d})}{d_p}(T_\infty - T_p) + \varepsilon_p \sigma(\theta_R^4 - T_p^4)\right] \tag{28}$$

for which the vaporization occurs at constant temperature.

The droplet velocities $\boldsymbol{u_p}$ and positions $\boldsymbol{x_p}$ are governed by Newton's laws of motion,

$$\frac{d\boldsymbol{u_p}}{dt} = \frac{\boldsymbol{u} - \boldsymbol{u_p}}{\tau_r} + \boldsymbol{F}_{VM} + \boldsymbol{F}_{PG} \tag{29a}$$

$$\frac{d\boldsymbol{x_p}}{dt} = \boldsymbol{u_p} \tag{29b}$$

where the three terms on the right-hand side represent the drag force, virtual mass force $\boldsymbol{F}_{VM} = \frac{1}{2}\frac{\rho}{\rho_p}\left(\boldsymbol{u}_p\nabla\boldsymbol{u} - \frac{d\boldsymbol{u}_p}{dt}\right)$, and pressure gradient force $\boldsymbol{F}_{PG} = \frac{\rho}{\rho_p}\boldsymbol{u}_p\nabla\boldsymbol{u}$. The droplet relaxation time is

$$\tau_r = \frac{\rho_p d_p^2}{18\mu}\frac{24}{C_d Re} \tag{30}$$

where μ is the liquid viscosity and C_d is the drag coefficient. We use a dynamic drag model that accounts for variations in droplet shape in high-speed flows for which droplet distortion and breakup occur. In this model, $C_d = C_{d,sphere}(1 + 2.632y)$ varies as a function of the local distortion factor y, which is governed by

$$\frac{d^2 y}{dt^2} = \frac{C_F}{C_b}\frac{\rho_g}{\rho_l}\frac{u^2}{r^2} - \frac{C_k\sigma}{\rho_l r^3}y - \frac{C_d\mu_l}{\rho_l r^2}\frac{dy}{dt} \tag{31}$$

where $C_{d,sphere} = 0.424$ for $Re > 1000$ and $C_{d,sphere} = \frac{24}{Re}\left(1 + \frac{1}{6}Re^{2/3}\right)$ for $Re \leq 1000$.

The impact of turbulent fluctuations on the computed droplet trajectories is approximated using a discrete random walk model [83]. Each droplet is assumed to interact with idealized turbulent eddies over the specified particle time step which alter the local gas velocity by adding a turbulent fluctuation to the computed mean value. The turbulent fluctuations are assumed to be Gaussian distributed with maximum magnitude equal to $\sqrt{u'^2} = \sqrt{2k/3}$. The turbulence-droplet interaction persists for a length of time equal to the smaller of the characteristic eddy lifetime, which is computed randomly with magnitude roughly equal to the integral time $T_L = 0.15\,k/\epsilon$, and the droplet eddy crossing time $t_{cross} = -\tau\ln\left[1 - L_e/\tau|\boldsymbol{u} - \boldsymbol{u}_p|\right]$. After this interaction ends, a new turbulent velocity is generated and the process repeated. For each droplet, the mean trajectory is then computed as the ensemble average of 5 independent trajectories.

Droplets are allowed to undergo a breakup process, characterized by the stripping of smaller child droplets from the surfaces of deformed parent droplets due to the growth of Kelvin-Helmholtz waves. We use the model of [84], which predicts the normalized wavelength Λ associated with the maximum growth rate Ω according to

$$\frac{\Lambda}{a} = 9.02\frac{\left(1 + 0.45\sqrt{Oh}\right)\left(1 + 0.4Ta^{0.7}\right)}{\left(1 + 0.87We_2^{1.67}\right)} \tag{32a}$$

$$\Omega\sqrt{\frac{\rho_1 a^3}{\sigma}} = \frac{0.34 + 0.36We_2^{1.5}}{(1 + Oh)(1 + 1.4Ta^{0.6})} \tag{32b}$$

where $We_1 = \rho_1 U^2 a/\sigma$ and $We_2 = \rho_2 U^2 a/\sigma$ are the liquid-phase and gas-phase Weber numbers, respectively, $U = |\boldsymbol{u} - \boldsymbol{u}_p|$ is the relative velocity between the droplet and the gas flow, a is the diameter of the parent droplet, and σ is the surface tension. The Ohnesorge and Taylor numbers are given by $Oh = \sqrt{We_1}/Re_1$ and $Ta = Oh\sqrt{We_2}$, respectively, with the Reynolds number $Re_1 = \rho_1 Ua/\mu_1$ defined based on the relative velocity and the liquid-phase density and viscosity. Child droplets are assumed to have a radius proportional to the most unstable wavelength, $r = B_0\Lambda$, with $B_0 = 0.61$ taken to be constant. The transfer of mass from the parent droplet to child droplets occurs according to a finite rate law,

$$\frac{da}{dt} = -\frac{a - r}{\tau_a} \tag{33}$$

where $\tau = 3.726 B_1 a / \Lambda \Omega$ with $B_1 = 1.73$ taken to be an adjustable model constant. When the mass of the collected child droplets exceeds 5% of the initial parent parcel mass, a new parcel is created with droplet diameters equal to r and velocities equal to that of the parent droplet with the addition of a random component in the plane orthogonal to the direction of the parent droplet. The velocity of the parent parcel is adjusted to conserve momentum.

In regions of the spray where the droplet volume fraction is sufficiently high, collisions between droplets can result in coalescence. The expected number of collisions between droplets in two parcels with radii r_1 and r_2 is computed using O'Rourke's model [85] as

$$\bar{n} = \frac{n_2 \pi (r_1 + r_2)^2 v_{rel} \Delta t}{V} \tag{34}$$

The probability distribution for the number of collisions follows a Poisson distribution $P(n) = e^{-\bar{n}} \bar{n}^n / n!$, which is used to determine whether or not a particular pair of droplets will collide over the specified time interval. Once a pair of droplets has been chosen for collision, a second random process is used to determine the outcome of the collision. If a random collision parameter

$b = (r_1 + r_2)\sqrt{\mathfrak{R}} < b_{crit}$, where $b_{crit} = (r_1 + r_2)\sqrt{\min\left(1, \frac{2.4f}{We_c}\right)}$ depends on the collisional Weber number We_c and an empirical function for the ratio of the droplet radii

$$f = (r_1/r_2)^3 - 2.4(r_1/r_2)^2 + 2.7(r_1/r_2), \tag{35}$$

the result of the collision is coalescence. If $b \geq b_{crit}$, the result is a glancing collision for which the post-collision velocities have been derived by [86]. Coupling between the Lagrangian phase and Eulerian continuous phase is accomplished through the source terms $S_{D,m}$, $S_{D,mom}$, and $S_{D,H}$ in Equations 10a-c. These source terms are computed by summing the individual contributions of the droplets within each continuous-phase control volume over the particle tracking period.

Crude Oil and Well Gas Surrogate Modeling
Crude oils are complex mixtures of liquid hydrocarbons and suspended solids that can vary appreciably from reservoir to reservoir, which poses a challenge for modeling their thermophysical properties. Ideally, we would like to model the oil as a single-component substance, since simulating multi-component liquids greatly increases the model complexity and resulting computational cost. Moreover, much of the physical data that would be needed to implement a multi-component liquid model (e.g., the constituent evaporation rates and relative concentrations) are not well known. In this work, we seek to model a single-component surrogate fuel for crude oil that reproduces critical thermophysical properties of the actual substance. This can be accomplished in two different ways. The first is to simply choose one of the various hydrocarbons that comprise typical crude oils as the surrogate fuel. The second is to create a fictitious surrogate liquid that utilizes empirical data to define its thermophysical state and volatization properties. While neither approach is completely satisfactory, they represent viable options for simulating practical wellhead burning scenarios. In the results that follow, we have chosen, in conjunction with our experimental team, heptane to be the single-phase surrogate liquid. An effort aimed at designing and calibrating a surrogate liquid that will model better the properties of typical crude oils is currently being planned.

A similar challenge exists for modeling the well gases that pressurize the reservoir. A more thorough description of this issue is given in a later section, and here we only wish to point out that much of the underlying flame behavior is dictated by the composition of the well gases. Ultimately, the exact composition of each reservoir could be measured and incorporated into the simulations. In the work that

follows, however, we consider only well gas surrogates composed of a single or several gaseous fuel species in conjunction with concurrent laboratory experiments.

Droplet Injection Model

The injection of liquid droplets into a gas-phase jet is a highly complex process that is, in general, poorly understood. This is particularly true for high-speed flows that occur during a wellhead blowout scenario where there is a strong stratification of the phases inside the wellbore pipe and uncertainty as to the precise nature of the internal two-phase flow. For the sake of generality, we model the two-phase flow inside the pipe as a combination of annular and misty flows. In the former region, a thin film flows along the pipe wall with an average velocity that is slower than the co-flowing well gases in the center of the pipe. The shear stress induced between the two phases causes instabilities to develop on the liquid surface and small-scale droplets to be "stripped" away and entrained into the bulk gas flow, giving rise to the internal misty flow region. At the pipe exit, the sudden expansion into the open atmosphere causes the annular liquid sheet to expand in diameter and undergo a dynamic breakup process. The resultant collection of droplets becomes entrained in the shear layer between the central jet and the ambient environment and, eventually, enters the flame zone and contributes to the overall burning rate and flame structure.

In order to simulate this injection process in a computationally-tractable, yet physically meaningful way, we have constructed a minimal geometric model that captures the basic physical processes of in-tube droplet "stripping" and external sheet breakup without explicitly resolving the kinematics of the liquid-gas interface. First, the oil film is assumed to be thin compared to the overall pipe diameter, and its effect on the internal gas-phase pipe flow is neglected. Second, we assume the internal droplet-stripping process can be described by classical Kelvin-Helmholtz instabilities, which gives a characteristic droplet size and injection rate. Third, we assume that the stripped droplets have had sufficient time to mix within the central gas flow. The long mixing length inside of typical wellbore pipes justifies this assumption [35]. Fourth, we assume that the liquid sheet dynamics can be described using linear stability theories developed for pressure-swirl atomizers, which describe sheet breakup as two separate processes: sheet rollup into filaments and filament breakup into droplets. From this analysis, we can estimate the persistence length of the liquid sheet and filaments and the characteristic size of droplets formed during the final stage of the breakup process. A conceptual drawing depicting these processes is shown in Figure 6
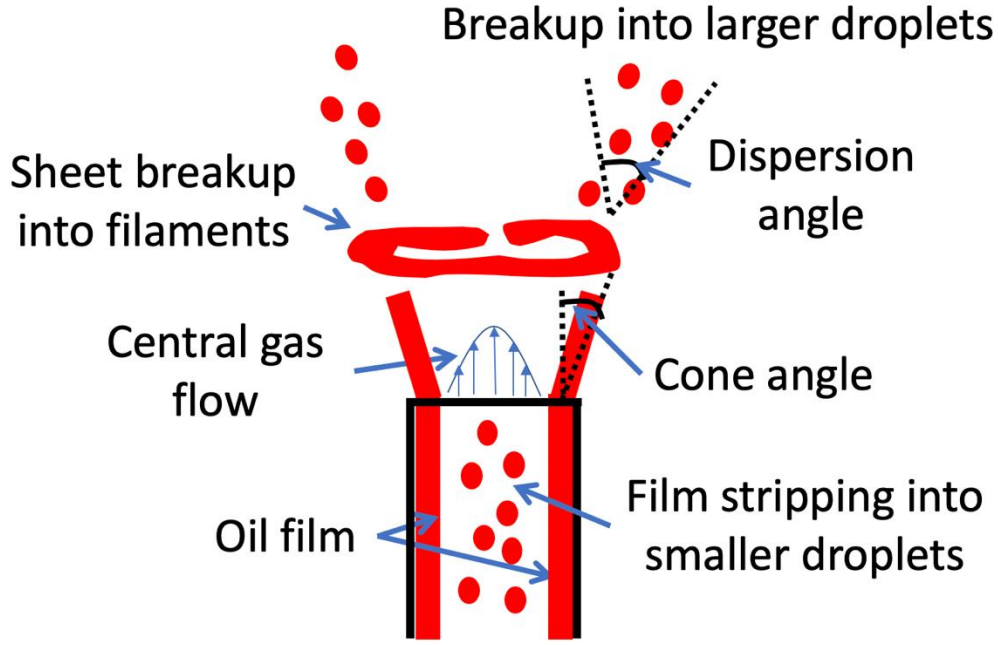
Fig. 6-Schematic diagram of the class of droplet injections models used for laboratory-scale calculations.

In our two-phase model, we define two regions inside of which droplets with distinct size distributions are injected into the system. The first region represents the distribution of droplets stripped from the liquid film on the pipe wall. Theory suggests that these droplets will be quite small (<10 microns in diameter), and we assume they are uniformly distributed across the cross section of the pipe and enter the flow with velocity similar to the average gas-jet velocity. The second region represents the external liquid sheet breakup process. We inject droplets at a short distance L above the pipe exit in an annular cross-section with outer radius r_1 and inner radius $r_1 - d_0$, where d_0 is the average droplet diameter. Together r_1 and L define a cone angle for the sheet expansion. Furthermore, the droplet velocities are randomly initialized over a predefined dispersion angle to simulate the highly unsteady filament breakup process.

Inside the tube, droplet stripping from a wall film in a shear flow is assumed to be initiated via Kelvin-Helmholtz instabilities for which the minimum wave length that produces growing waves is

$$\lambda_{min} = 2\pi \sqrt[3]{16} \left(\frac{\mu_l \sqrt{\sigma/\rho_l}}{\beta \rho_g V_g^2} \right)^{2/3} \qquad (36)$$

and the corresponding average size of the stripped droplets is $d_p = 4.5 F \lambda_{min}$, where F and β are model constants taken to be 0.14 and 0.3, respectively. While such an analysis can give a qualitative description of the average droplet diameter within the misty flow region, it cannot be used with a sufficient degree of confidence for this modeling exercise. Droplet stripping is a continuous process that can occur over a long distance within the wellbore, over which the physical properties of the flow are changing. The stripped droplets subsequently undergo evaporation, coalescence, and aerodynamic breakup processes, and accordingly the droplet diameter will be a function of its time-of-flight within the tube. Thus a distribution of droplet sizes exists at any given cross-section. It is more practical to utilize existing engineering

correlations for average droplet sizes, e.g. [34,35], although their applicability to wellhead flow conditions has not been strictly validated (see Section 1 for a discussion).

The primary external droplet formation process occurs through the breakup of an annular liquid sheet as it is ejected from the atomizer pipe into the flow field. This scenario is qualitatively similar to the flow within commonly used atomizers, such as the pressure-swirl atomizer and the air-blast atomizer, for which established linear stability theories exist [71]. We assume the radius of the liquid sheet expands as it leaves the pipe in coordination with spreading of the gas-phase jet at angle θ. The sheet breakup length can be modeled by

$$L_b = \frac{U}{\Omega} ln\left(\frac{\eta_b}{\eta_0}\right) \tag{37}$$

where U is the relative velocity between the liquid sheet and the internal gas flow, $ln(\eta_b/\eta_0)$ is a modeling constant taken to be 12, and Ω is the maximum value of growth rate allowed by the dispersion relation

$$\omega_r = \frac{1}{k_h^* + Q}\left[-2V_L k_h^* + \sqrt{4V_L^2 k^4 k_h^{*2} - (QUk)^2 - (k_h^* + Q)(-QU^2 k^2 + \sigma k^3/\rho_l)}\right] \tag{38}$$

where $k_h^* = \tanh(kh)$, V_L is the velocity of the liquid sheet, and $Q = \rho_g/\rho_l$ is the ratio of densities. The sheet breakup is a two-step process. In the first, the sheet tears to form toroidal ligaments with diameter $d_L = \sqrt{8h_{end}/K_S}$, where K_S is the wavenumber associated with Ω, and $h_{end} = r_0 h_0/(r_0 + L_b \sin(\theta/2))$ is the sheet half-thickness at L_b and h_0 is the sheet half-thickness as it leaves the atomizer pipe. Ligament breakup into droplets is assumed to behave according to Weber's theory (Weber, 1931) for capillary instability yielding droplet diameters of

$$d_0 = 1.88 d_L (1 + 3Oh)^{1/6}. \tag{39}$$

It remains to estimate the liquid film thickness and velocity, as well as the relative fraction of small droplets created inside the wellbore via Kelvin-Helmholz stripping and large droplets formed by the sheet atomization process. Turning again to engineering correlations, it is possible to obtain estimates for the stripped droplet entrainment fraction as a function of the wellbore flow conditions. Combining this information with data for the total mass flux, liquid volumetric flow rate, and gas-to-oil ratio, it is possible to obtain the necessary estimates for liquid film thickness and velocity.

Validation Progress

In the preceding sections, a minimal two-phase reacting flow model for simulating wellhead fires has been presented that represents a compromise between physical fidelity and computational efficiency. The goal has been to retain a sufficient amount of the former to provide an estimate of the oil burning efficiency for a given set of reservoir conditions. It remains now to perform a series of validation studies to provide some confidence that the proposed model captures the controlling physical processes to a sufficient level of accuracy. Validation efforts can be loosely grouped into two categories: gas-phase flame structure and droplet behavior. In reality, these effects are tightly coupled and cannot be easily measured in isolation. This is why adopting a multi-pronged validation approach, such as the one pursued in this work, is necessary. In the "Experimental Development" section, two different experimental facilities are described that differ substantially in scale. The laboratory- or bench-scale burner has an internal pipe diameter of less than a millimeter and produces flames on the order of a meter in height. The scale of this apparatus is sufficiently small to allow testing inside a controlled laboratory environment, which enables a suite of optical and laser diagnostics for simultaneous temperature and droplet measurements. The intermediate-scale facility utilizes a much larger (0.25" ID) pipe and produces flames that are 10s of meters in height.

Testing of these flames must be done outdoors in a semi-confined environment, which severely restricts the use of nonintrusive laser diagnostics but allows the measurement of fallout from actual crude oil flames.

The gas-phase flame can be described by a spatial mapping of temperature. This provides two critical pieces of information. The first is the flame anchoring position at or above the pipe exit. Correct prediction of this quantity gives confidence in the parameterization of the gas-phase flame model, particularly in the turbulent flame speed parameter that controls the reactions in regions were fuel and oxidizer have undergone some level of mixing. The second critical piece of information is the maximum temperature measured within the plume. This provides information on the balance of energy released by the gas-phase flame and the energy required to vaporize the liquid oil droplets. Additionally, mapping the radial spread of the hot product gases provides validation of the underlying fluid dynamic turbulence models.

Measurements of droplet behavior are necessary to validate both the droplet injection models and the empirical thermodynamic models. This can be accomplished by measuring the droplet size and velocity throughout the flame plume. The main quantities that need to be measured are the initial size and speed of the droplets along with a measure for the height above the pipe exit at which the droplets can be recognized as discrete entities. The average angle with respect the vertical at which the droplets enter the gas-phase is also a critical piece of information. Within the flame zone, droplet sizes are governed by the vaporization and boiling models, as well as the rate of droplet breakup induced by fluid dynamic shear stresses and droplet agglomeration caused by droplet collisions. Without simultaneous temperature measurements, it would be impossible to separate out these competing effects.

In the section that follows, we describe the flames predicted by the computational model for a variety of flow conditions used during operation of the laboratory-scale burner. Preliminary analysis of the gas-phase flame behavior in the intermediate-scale facility is then given. A complete simulation of the intermediate-scale two-phase crude-oil flame has not yet been performed and is pending the calibration of an appropriate surrogate fuel model for the crude oil used in the experiments.

Results & Discussion

Bench-Scale

Gas-Phase
The model transport equations developed in the previous subsections were used to simulate the bench-scale experimental configuration described in the Bench-Scale section of Experiment. The basic configuration is shown in Figure 7a. The well gas surrogate is injected into the system through a central feed pipe with diameter 0.84 mm (0.033 in). An annular coaxial pilot flame is anchored just downstream of the burner to assist in stabilizing the jet flame. The pilot flame is a lean hydrogen-air premixed flame operating near the flammability limit of the mixture at a nominal equivalence ratio of 0.32. This value was chosen to leave a sufficient amount of oxygen in the hot combustion products to allow reaction in the hydrocarbon jet flame downstream. Here, we do not explicitly simulate the pilot flame. Instead, we model the hot product stream from the pilot flame as a fixed inflow condition for the oxidizer stream of the propane flame. The stream consists of a mixture of water vapor, oxygen, and nitrogen with corresponding mole fractions of 0.122, 0.136, and 0.742, respectively. The temperature of the incoming stream is held constant at 1400 K with an axial velocity of approximately 2 m/s.

We exploit circumferential symmetry in the mean quantities and simulate only a two-dimensional axisymmetric slice of the domain. A triangular mesh is used to discretize the domain that has minimum grid spacing of 0.02 mm at the feed tube exit and within the shear layer downstream of the burner. Several views of the computational mesh used in this study are shown in Figure 7b and c.
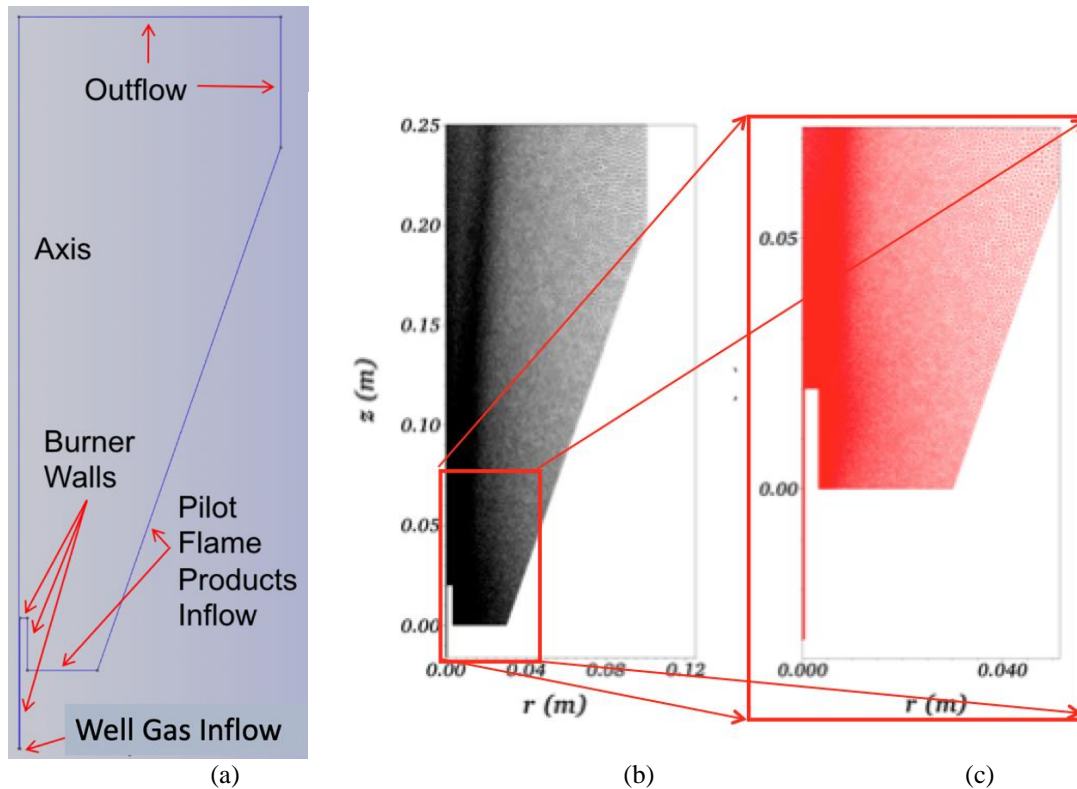
Fig. 7-(a) Model axisymmetric geometry of bench-scale burner used in simulations. Computational mesh for (b) full domain and (c) magnified view of propane feed tube.

Well gas surrogate enters the domain through the inflow plane via a pressure boundary condition for which the stagnation pressure and temperature are specified. The local pressure and fluid velocity adjust so that the inflow velocity dictated by the pressure gradient within the tube matches that required to satisfy the isentropic compressible flow relationships for the specified stagnation quantities. The other two inflow planes designated in Figure 7a model the injection of hot product gases from the pilot flame as described above. No-slip boundary conditions are applied on the inner and outer walls of the propane feed tube using standard turbulence wall functions to set the velocity in the grid cells adjacent to the walls. The $r = 0$ axis is a line of radial symmetry, and the outflow boundaries maintain the local static pressure at $P = 101325$ Pa. In all of the calculations, we used the ANSYS FLUENT steady-state pressure-based flow solver to arrive at a final converged solution. The domain was initialized with a low-speed incompressible solution and then the propane inflow pressure was slowly ramped up until we achieved the desired mass flow rate in the propane feed tube. In this work, two different well gas surrogates were tested in the laboratory-scale burner: propane and ethane. In the remainder of this section, we describe features of the gas-phase flame structure computed for the former and note that the ethane flame structure was qualitatively similar to the propane flame structure. More details regarding the ethane well gas surrogate flame will be discussed in the next sub-section.

For the propane jet flame analysis, three different mass flow rates of the well gas surrogate were tested: 0.1, 0.2, and 0.3 g/s corresponding to concurrent laboratory tests. Figures 8-10 show the results of these analyses. Magnified views of the density, Mach number, and axial velocity in the near field of the propane jet discharging from the feed tube are shown in Figure 8. Several important observations can be made. First, the boundary layer within the feed tube is rather large, occupying nearly 20% of the cross-sectional area of

the pipe. This is due to the small diameter of the feed tube and should be taken into account when converting between velocity and mass flow rate. Second, compressibility effects are important for all three jets. Even at the lowest flow rate tested (0.1g/s), the Mach number at the tube exit reaches 0.874. The two cases with higher flow rates produce supersonic jets. The density fields show the classical diamond pattern of regions of high density and pressure that form behind oblique shock waves within an underexpanded jet. Closer inspection of Figure 8 shows that the compressible jet structure consists of an inviscid core that occupies a significant portion of the jet and a viscous sheath in which mixing between the subsonic propane and co-flowing pilot flame product gases takes place. The net result is that the supersonic jets bulge out in the radial direction slightly just downstream of the burner. Further downstream, the 0.3 g/s jet remains narrower than the 0.1 g/s jet.

Figure 9 shows full-field views of the temperature and product species formation rate in the turbulent flame brush for each of the three cases. The qualitative structure of the flames agrees with our preliminary expectations. Near the burner tip, where the shear rates are largest, the flame is quenched. Farther downstream, after sufficient mixing has occurred, the flame is able to ignite and anchor. Behind the leading edge of the flame, reaction continues to occur in a trailing diffusion flame as the unburned propane from the central region of the jet mixes with the oxygen from the oxidizer stream. The resulting partially-premixed turbulent jet flame is stable and statistically-steady for all three flow rates. Note that this is only true when the pilot flame is active. Without the initial preheating provided by the pilot flame, a stable jet flame cannot be established. Figure 10 shows the mass fractions of one of the primary product species, CO_2 and the reaction progress variable. Complete oxidation of the propane jet is achieved for this configuration. From a qualitative standpoint, the turbulent flame models utilized in this study account for the predominant physical processes and are able to reproduce the features of high-speed turbulent jet flames. Quantitative comparisons with experimental data will be provided in Section *Computational and Experimental Comparison*.
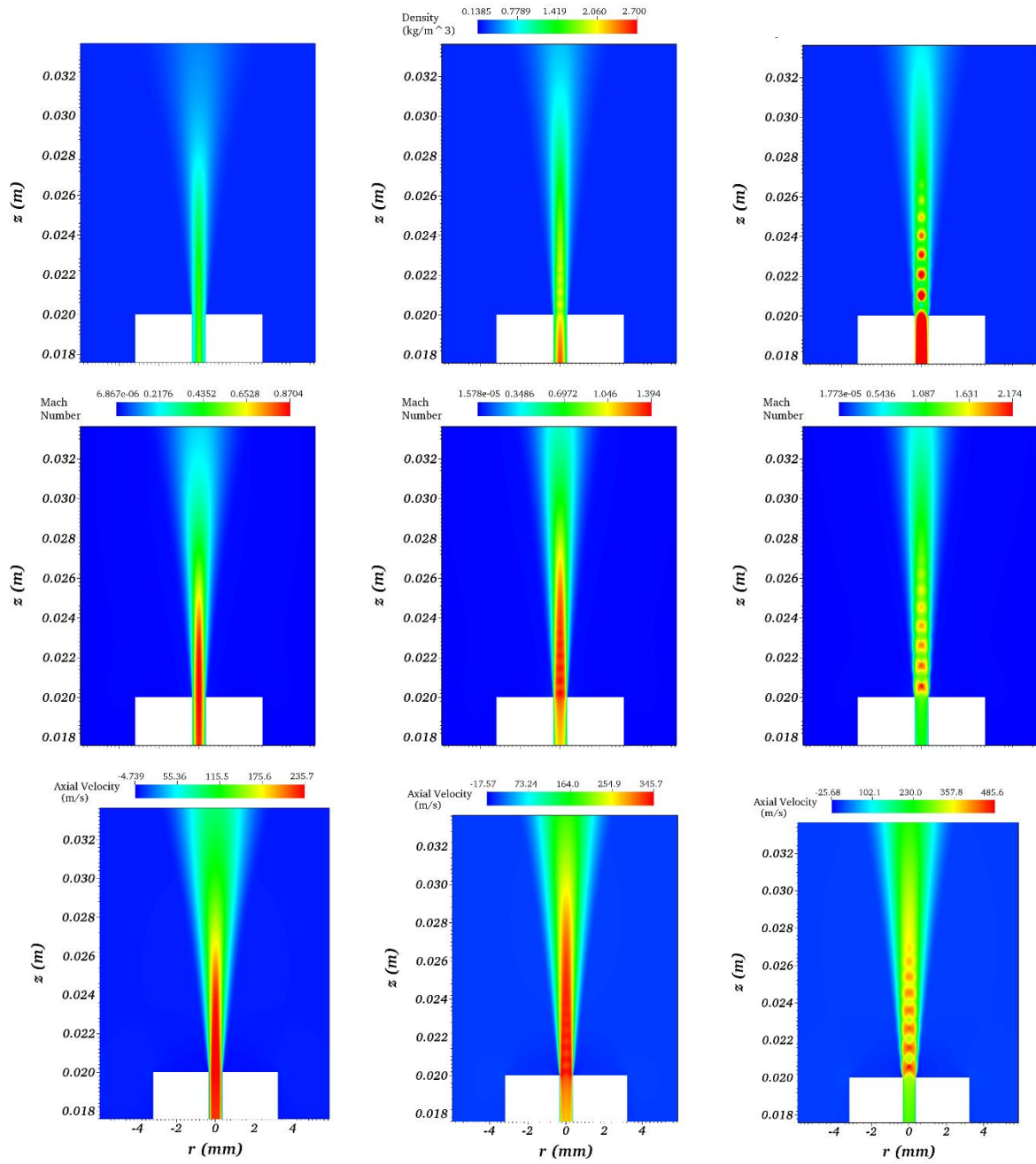
Fig. 8-Density (top row), Mach number (middle row), and axial velocity (bottom row) in the near-field of the propane discharge jet for mass flow rates of 0.1 g/s (left column), 0.2 g/s (center column), and 0.3 g/s (right column).
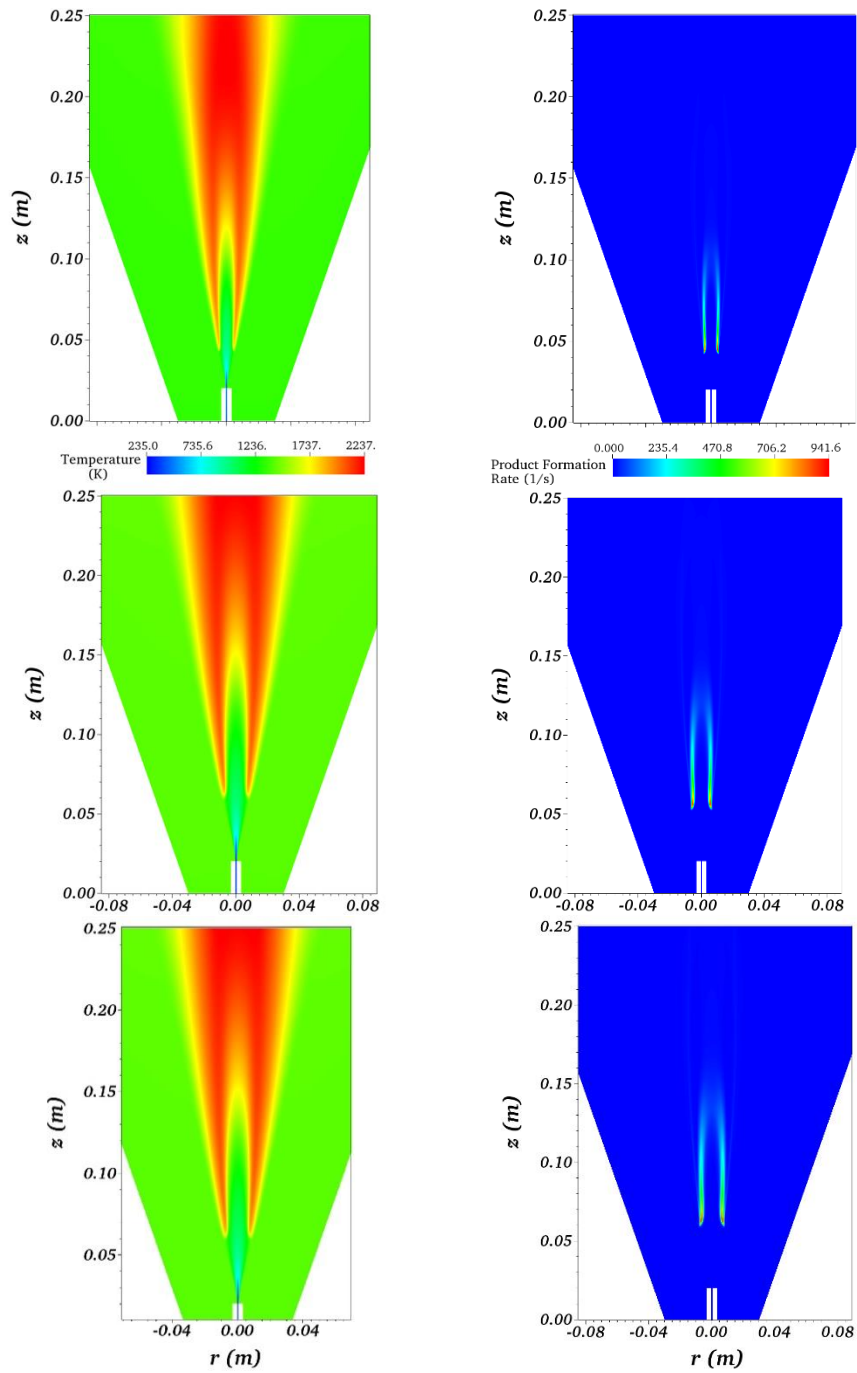
Fig. 9-Temperature (left column) and product formation rate (right column) for mass flow rates of 0.1 g/s (top row), 0.2 g/s (center row), and 0.3 g/s (bottom row).
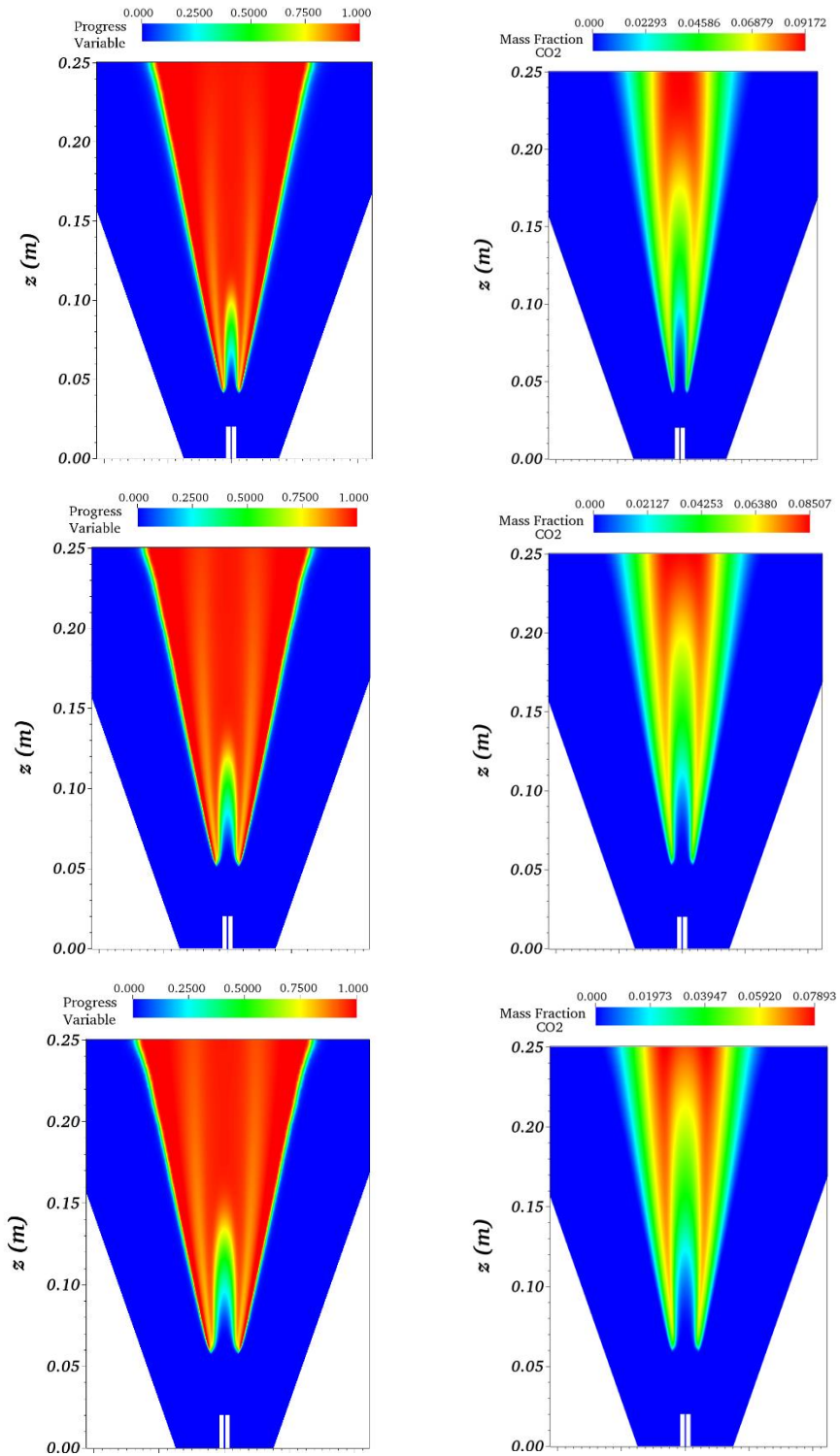
Fig. 10-Reaction progress variable (left column) and mass fraction of CO_2 (right column) for mass flow rates of 0.1 g/s (top row), 0.2 g/s (center row), and 0.3 g/s (bottom row).

Two-Phase

We turn now to our attention to a model two-phase flame system. In this exercise, we take ethane to be the well-gas surrogate and heptane to be the oil surrogate and consider a simplified model of the ethane-heptane spray burner discussed in the bench-scale experimental platform description. As for the gas-phase system described in the preceding section, the pilot flame anchors very close to the burner surface, and we set the inflow conditions for a fixed co-flow of product species oxygen, nitrogen, and water vapor, assuming a nominal pilot-flame equivalence ratio of $\phi = 0.32$. The corresponding adiabatic flame temperature is 1240 K with mole fractions of 0.134, 0.126, and 0.74 for the three species (O_2, H_2O, N_2, respectively).

Liquid heptane droplets are introduced into the system using the dual-region injection model described in the preceding section. In the outer annular region, droplets are injected into the domain around a hollow cone with radius $r_{cone} = r_0 + L_b \cos\theta$ and cone angle equal to the sheet ejection angle θ. Droplet velocities are modified to give a dispersion angle of 8 degrees with respect to θ. The velocity magnitude is assumed to be equal to the velocity of the liquid sheet, which we define based on an estimate for h_0 and the given liquid mass flow rate. In the inner region of the jet, we inject droplets that are assumed to have been stripped from the annular film on the interior of the fuel supply pipe. These droplets are smaller than those injected in the outer region, and we assume that they enter the domain uniformly distributed across the diameter of the pipe with velocity commensurate with the gas-phase velocity. In both regions, we assume the droplet diameters follow a Rosin-Rammler distribution with a mean droplet diameter of d_0 (specific to the region) and a spread parameter of 3.5.

The remaining estimates required to complete the injection model are the spreading angle of the jet θ, the film thickness, and the internal pipe flow droplet entrainment fraction. The first of these can be estimated based on single-phase flow simulations, assuming the liquid sheet expands at an angle roughly equivalent to the spread angle of the inviscid jet core. The latter two quantities are more difficult to estimate, particularly for a realistic wellhead blowout scenario. In principle, correlations can be used to estimate the average droplet diameter of the inner region, the entrainment fraction and the liquid film thickness. For the relatively low liquid Reynolds numbers associated with the laboratory-scale burner, correlations predict significantly less than 100% entrainment. In this section, we leave the specific values of these quantities as free parameters and provide a preliminary demonstration of the sensitivity of the computed two-phase flame structures to the droplet injection conditions. In this example, we assume a low entrainment efficiency and set the mass flow rate of stripped droplets to 5% of the total liquid mass flow rate, with corresponding mean droplet diameter of 0.01 mm.

We evaluate the performance of the computational model described in the preceding sections for a turbulent spray flame with ethane and heptane mass flow rates equal to 0.1 g/s for several different parameterizations of the injection conditions in the outer annular region. For the various parameters chosen, turbulent flame structures formed that were qualitatively similar to those observed experimentally. The droplet distributions at several axial locations downstream of the injection also compared favorably with experimental droplet size and velocity measurements. With that said, the details of the behavior of the liquid droplets were found to depend strongly on the choice of injection conditions. As an example, we show the temperature contours and gaseous heptane mass fraction computed for the ethane/heptane spray flame using three different injection conditions in Figures 11 and 12, respectively. In all three cases, the conditions in the central injection region, representing the stripped droplets from the internal pipe flow, and the mass flow rate and velocity magnitude of the droplets in the second annular injection region were identical. The mean diameter and the angle of the injection velocity of the droplets in the second injection region were varied. In the first case represented by Figures 11a and 12a, the droplets were injected with mean diameter of 0.05 mm with cone and dispersion angles equal to zero. In the second case (Figures 11b and 12b), the mean droplet diameter was increased to 0.1 mm, and the cone angle was taken to be 10 degrees. In the third case (Figures 11c and 12c), the mean droplet diameter was 0.065 mm, and the injection velocity was variable with a cone angle of 10 degrees and a dispersion angle of 8 degrees. The primary observation is

that the flames behave qualitatively different for the three cases. Depending on the injection properties, the flame can be relatively weak with heptane-rich conditions near the center of the jet (Figures 11a, 12a), relatively narrow with incomplete heptane combustion (Figures 11b, 12b), and relatively robust with more combustion near the burner lip (Figures 11c, 12c).

The injection parameters in the third case correspond more closely to the jet breakup theory described earlier; however, we note that the theory is imprecise and only partially applicable to the proposed annular oil-film concept shown in Figure 6. In particular, the theory neglects gas compressibility effects, which we know will be important for the high-speed jets considered in this work. These parameters also fall in line with both the Kataoka and Berna correlations described in Section 1, but it should be noted that within the range of Reynolds numbers of which the laboratory-scale burner operates, there is significant spread in the predictions made by these two correlations in terms of entrainment fraction (see Figure 2, for example). If such correlations are to be relied upon for predicting droplet distributions for certain well head flow conditions, then there is a clear need to revisit the uncertainties associated with the existing data used to develop the correlations. A first step toward achieving this has recently been undertaken for the laboratory-scale ethane-heptane flame, for which high-speed images of the spray field were taken for several different gas-liquid mass flow rate combinations that were sufficiently fast to capture the trajectories of individual droplets. This initial analysis will be described in the experimental results section of the bench-scale burner.

(a)   (b)
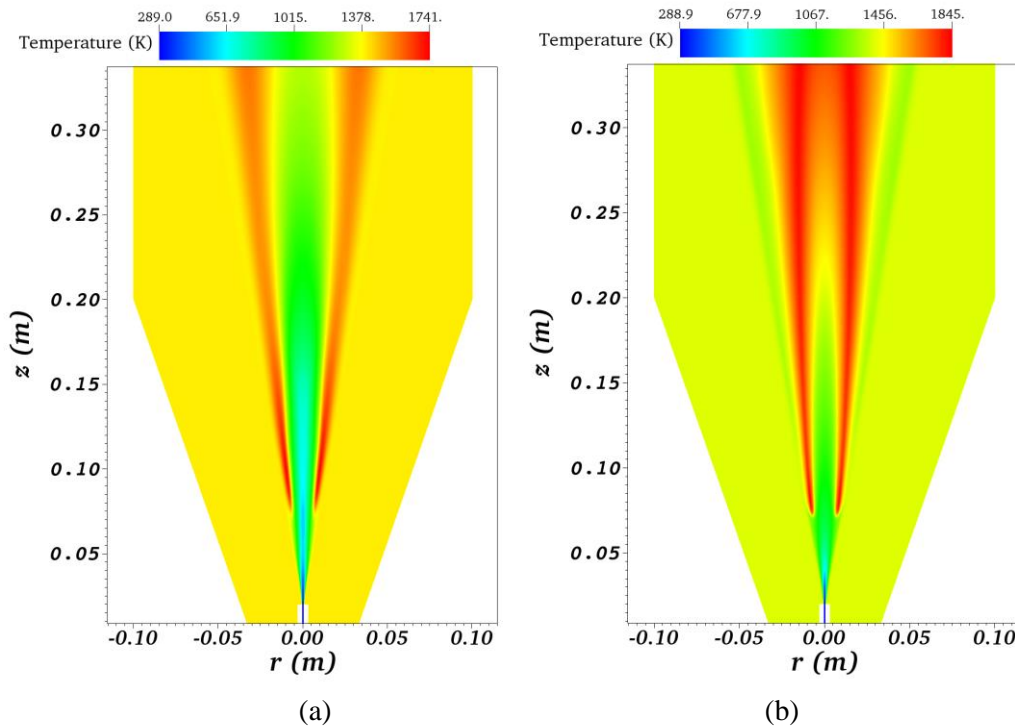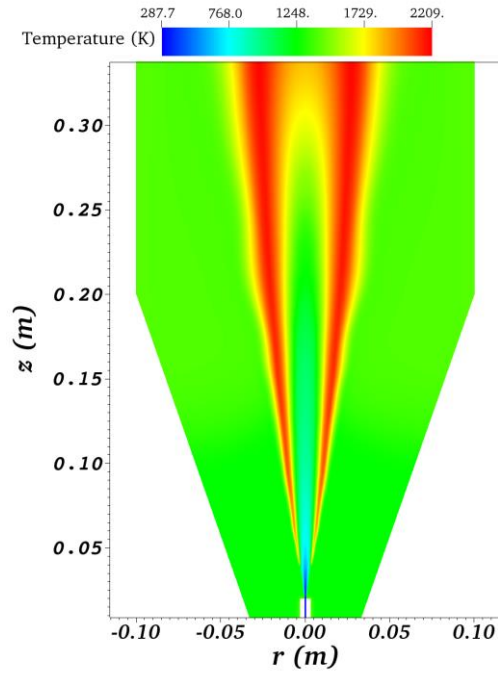
(c)

Fig. 11-Temperature contours computed for turbulent ethane/heptane jet flame using three different injection models: (a) 0 degree cone angle, 0 degree dispersion angle, (b) 10 degree cone angle, 0 degree dispersion angle, (c) 10 degree cone angle, 8 degree dispersion angle.
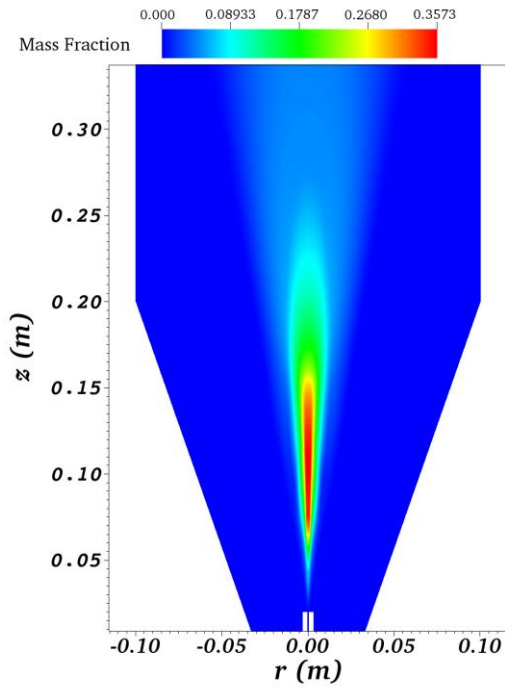
(a)
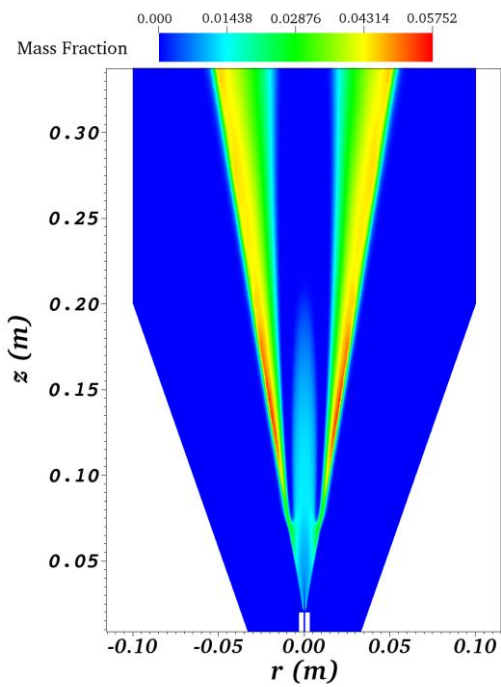
(b)
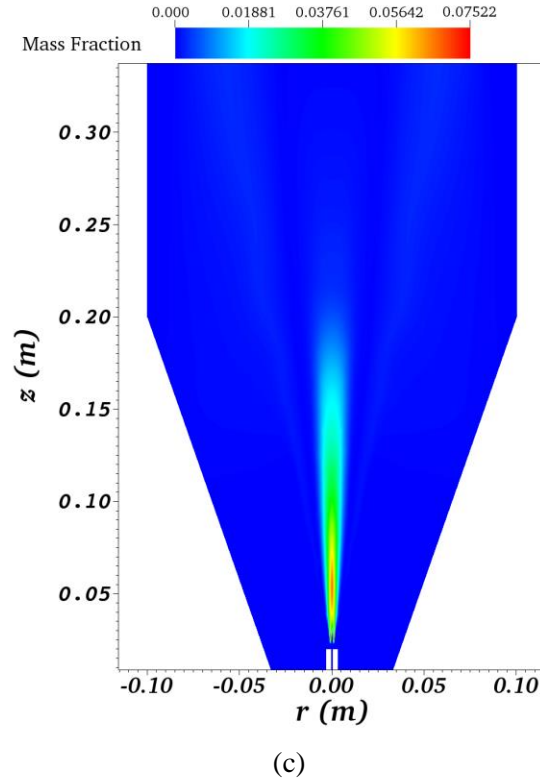
Fig. 12-Gaseous heptane mass fraction contours computed for turbulent ethane/heptane jet flame using three different injection models: (a) 0 degree cone angle, 0 degree dispersion angle, (b) 10 degree cone angle, 0 degree dispersion angle, (c) 10 degree cone angle, 8 degree dispersion angle.

Here, we show the predicted spatial distributions of droplet size and velocity computed for the case of 0.065 mm droplets injected from the outer region at a 10 degree cone angle with an 8 degree dispersion angle (Figure 11c and 12c) in order to highlight the various physical processes that are contributing to the overall droplet dynamics. Figure 13 shows the average D_{10} and D_{32} particle diameters as a function of radial distance from the burner centerline on plane slices through axial locations 10, 20, and 30 mm downstream of the atomizer pipe. Overall, the diameter distributions follow the same trend observed in experiments and described in the subsequent section: small droplets predominate near the center of the jet, rapidly increasing to larger droplets near the periphery of the jet. This is to be expected given the dual-region injection model developed in this work. The computed droplet velocities compare quite well with the experimental measurements, decreasing from a maximum of approximately 100 m/s near the center line at 10 mm to roughly 75 m/s 30 mm downstream. There are two notable observations that can be made with regard to the D_{10} and D_{32} predictions. First, the mean droplet diameters are biased toward larger diameter droplets, as evidenced by large jumps in the Sauter mean diameter relative to the mean diameter in the 1-2 mm radial locations. The strong bias at the $x = 10$ mm axial location suggests that the mean is being influenced by a subset of larger droplets that coalesced from two or several smaller droplets. A larger statistical sample would be needed to even out this behavior. Second, the rapid decrease in droplet diameter between the 10 mm and 20 mm observation points highlights the role aerodynamic breakup plays in conditioning the larger outer region droplets for vaporization. Neglecting this process could lead to overprediction of droplet fallout for a given set of flow conditions.
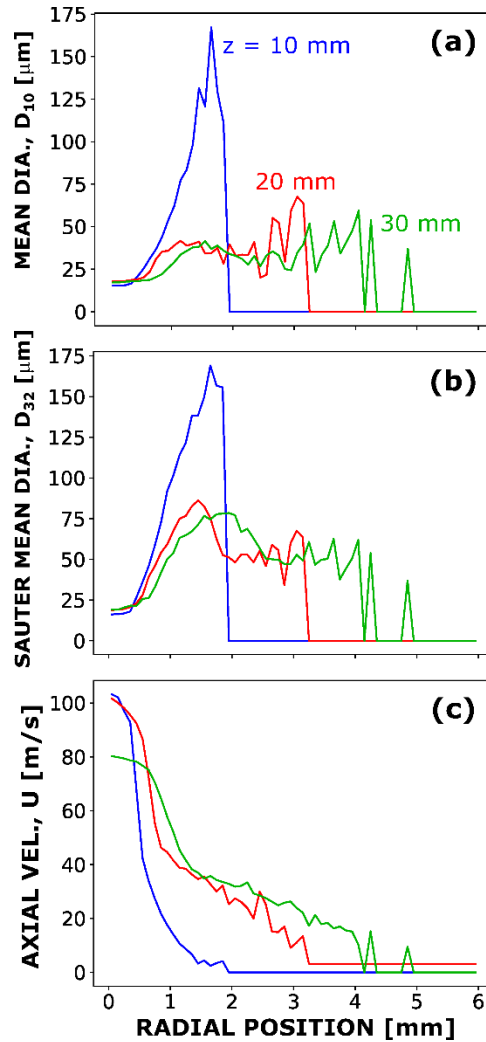
Fig. 13-(a) Mean diameter D_{10}, (b) Sauter mean diameter D_{32}, and (c) average axial velocity profiles as a function of radius at three axial locations downstream of the burner lip: 10 mm (blue), 20 mm (red), and 30 mm (green).

Intermediate-Scale

Gas-Phase

We next demonstrate the behavior of the model for a scaled-up burner configuration with mass flow rates an order of magnitude larger than the laboratory-scale configuration but still significantly smaller than an actual well head. In this intermediate-scale system, we consider two different well-gas surrogates: pure propane and a mixture of methane, ethane, and propane. The fuel supply tube is a pipe with inner diameter of 0.25 in (3.175 mm) and outer diameter of 0.375 in (4.7625 mm). In our simulations, we truncate the domain at a height of 2.5 m above the fuel supply tube, and the width tapers from 0.3 m below the propane discharge point to 1 m at the top of the domain. As in the laboratory-scale simulations, we explicitly model a short section (70 cm) of the propane feed pipe to allow for a smooth transition from the idealized pressure and velocity conditions imposed at the inflow to a fully-developed turbulent pipe flow at the point of discharge to the atmosphere. The well gas inflow, wall, and outflow boundary conditions were the same as in the laboratory-scale simulations (with the stagnation conditions in the propane feed tube scaled to give the desired mass flow rates). The significant difference between the laboratory-scale and intermediate-scale

38

simulations is the lack of an external pilot flame in the intermediate-scale device over a range of flow conditions. We model the surrounding atmosphere below and at the radial edge of the simulation domain as an inflow for the air stream surrounding the propane jet. At these boundaries, the stagnation pressure is set to 10^{-4} Pa above atmospheric to generate a low-velocity co-flow to stabilize the simulations and provide a source of air that will be entrained by the flame..

Figure 14 shows the results of an initial single-phase turbulent flame calculation of the intermediate-scale burner using pure propane as the well-gas surrogate with mass flow rate of 4.6 g/s. The temperature, mass fraction of H_2O, and product formation rate profiles shown in the figure suggest a flame liftoff height of approximately 150 mm, a total height of 1.8-2 m, and a diameter of 300-400 mm, values consistent with experimental observations.
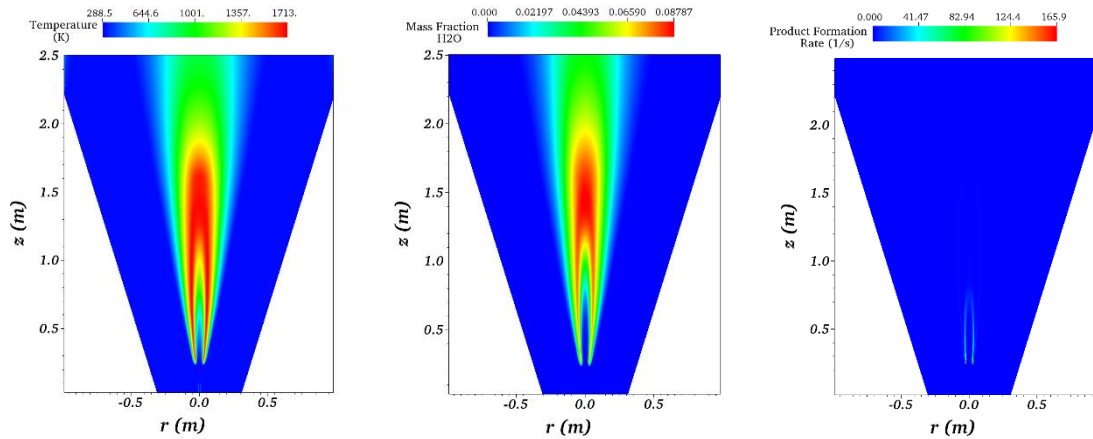
Fig. 14-Temperature (left), mass fraction of water vapor (center) and product formation rate (right) computed for a mass flow rate of 4.6 g/s in the intermediate-scale burner.

Two-Phase

We conclude this section with a demonstration of a two-phase flame calculation simulating the intermediate-scale burner configuration. In this scenario, we use a 80:5:15% blend of methane, ethane, and propane, respectively, as the well-gas surrogate and liquid heptane as the crude oil surrogate. The well-gas surrogate is delivered at a rate of 3 g/s, and the liquid heptane is injected with a total mass flow rate of 16 g/s. Here, we assume 100% droplet entrainment within the fuel supply tube in order to examine the limiting high-Reynolds-number blowout scenario. For these flow conditions, the entrained droplets are small, and we set the mean droplet diameter to 0.02 mm. As in the laboratory-scale calculations, the droplets are uniformly distributed across the inner region of the two-region injection model with a velocity close to the gas-phase velocity. Here, we assume the droplet velocity is 100 m/s and the cone angle is zero.
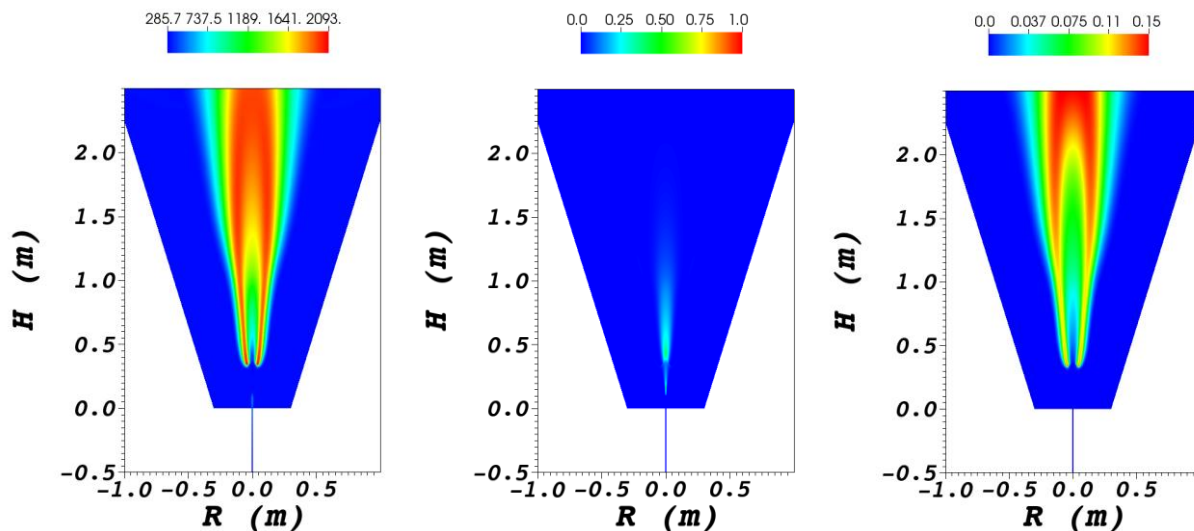
Fig. 15-Temperature (left, Kelvin), mass fraction of gaseous heptane (center) and mass fraction of carbon dioxide (right) computed for a gas mass flow rate of 3.0 g/s and liquid mass flow rate of 16.0 g/s in the intermediate-scale burner configuration.

Figure 15 shows the temperature, mass fraction of gaseous heptane, and mass fraction of carbon dioxide computed for this two-phase flow condition. While the overall flame structure is similar to that observed for the single-phase flame, the two-phase flame is significantly taller with a 300 K increase in maximum temperature. While no quantitative data are yet available for comparison, these observations are consistent with the behavior of the flames produced by the intermediate-scale burner described in the next section.

For this limiting case of complete droplet atomization within the internal pipe flow, we observe complete droplet combustion; however, in the preceding section, we observed cases for which the combustion of the oil surrogate was incomplete. Beyond the scale of the burner, the primary difference in these simulations was the relative proportion of small inner-region droplets to larger outer-region droplets, with the laboratory-scale simulations approaching the opposite limiting case of near-zero droplet entrainment. While it is still premature to extrapolate the results of these simulations to realistic well-head burning scenarios, they do highlight the important role the internal two-phase pipe flow might play in determining overall burn efficiency.

EXPERIMENTAL VALIDATION

Two different experimental platforms were developed for this program in order to capture different behavior. To measure the detailed spray combustion behavior, we developed a laboratory- or bench-scale experiment. Spray droplets, combustion chemistry, combustion temperature, and spray velocities require instrumentation that requires climate-controlled environments. Thus, these behaviors are difficult to measure in large-scale, experiments because such experiments cannot be operated indoors. To examine burn efficiency and flame heat transfer behavior, we developed an intermediate-scale experiment. Droplet fallout or burn efficiency requires size scales that accurately mimic realistic wellhead behavior, at a practical, safe scale that mimic realistic radiative and convective heat transfer with the environment. A full-scale wellhead experiment is not presently practical or safe on Naval Research Laboratory facilities. Two

40

section follow (*Bench-Scale* and *Intermediate-Scale*) that describe the respective experimental platforms and results.

It is worth noting the changes in gaseous fuel that we have explored during this investigation. Initially, we tried to use propane as the gaseous fuel for both the bench-scale and intermediate-scale experiments. Propane provides a good chemical kinetic surrogate for alkanes with carbon numbers greater than three because of the similar global chemical kinetic behavior [87]. Though readily available, liquid propane has low available pressures for the outdoor, intermediate-scale experiments, which limited our flow rates and created propane "snow" as the gas expanded and cooled through the flow system. In the laboratory experiment, propane could not provide the desired entrainment and atomization velocities. Methane, unfortunately, has a very high activation energy for ignition due to its molecular structure. The carbon-carbon bonds of larger alkanes require less energy to break; we could not anchor methane flames very easily. In the laboratory, we found that the lower ignition activation energy of ethane allowed the flames to anchor.

For our intermediate-scale experiment, our objective was to capture the high velocity of a wellhead flow while still capturing realistic chemical kinetic behavior. To this end, we adopted the use of a 50%-25%-25% blend (by mass) of methane, ethane, and propane, respectively. A survey of literature revealed that the exact blend is rarely reported and is difficult to measure [88,89]. Instead, using critical pressure data, the gas blend is back-calculated based on the assumption of what constituents are present. In particular, these are CO_2, N_2, and alkane gases from C_1 through C_6.

The 1994 paper by Ali *et al.* performs composition simulation based on the PVT analysis and slim-tube data for the Endicott reservoir, which neighbors the Liberty reservoir [89]. The gases in the well are described as solution gases, which are dissolved into the petroleum liquid, and the gas-cap gases, which are the gases above the liquid in the reservoir. A reservoir can have pressures above 31 MPa (4,500 psig) and temperatures above 366 K (200 °F), which causes significant phase separations among the reservoir gases. Carbon dioxide, Prudhoe Bay Gas (PBG), and natural gas liquids (NGL) are injected into the well to increase the reservoir pressure to help propel the petroleum out of the well. These gases and other solvents are used because they are produced from the reservoir and are not as valuable as the petroleum itself. In consideration of the high pressures, the lower molecular weight hydrocarbons are liquids in the reservoirs and act as solvents to aid in the removal of the heavier hydrocarbons. These and other enhanced oil removal (EOR) technologies are discussed by Ali *et al.* [89] and are dependent on the reservoir constituents. Therefore, the initial well chemistry constituents are revealed and discussed. Table 2 lists the mol% of the live oil, PBG, and NGL. Surprisingly, it lists 12% CO_2.

Table 2-Example gas fractions of well gas.

Gas	Endicott, Ali 1994 [89]			IHRDC [90]	
	Oil Mol%	Well Gas Mol%	Well Gas Mol%, no CO_2 or N_2	Oil Mol%	Well Gas Mol%
CO_2	12.0	18			
N_2	0.16	0			
C_1	41.8	64	77	37.5	39
C_2	5.56	9	11	9.70	9.7
C_3	2.69	4	12	7.00	20
I-C_4	0.41	1		1.44	

N-C$_4$	1.02	2		3.93	
I-C$_5$	0.36	1		1.44	
N-C$_5$	0.52	1		1.41	
C$_6$	0.80	1		4.33	

Table 2 provides the calculated gas fraction splits from the Endicott reservoir [89] and an industry training website [90], with the propane to hexane gases grouped together in the hydrocarbon gas comparison columns because of their common chemical kinetic behavior [87]. It is clear that there is a wide range of variability to the molar fraction within the well gas. To establish a canonical standard, it is necessary that a molar fraction be chosen and then used consistently in both experimental and computational work. If a validated chemical-kinetic model is adopted that includes the constituent species, adapting the molar fractions to different reservoir gas mixtures should require little significant changes to the computational model or additional experimental validation, as long as we operate within validated molar fractions.

The surrogate of 50%-25%-25% blend (by mass) of methane, ethane, and propane, respectively, fits the aforementioned criteria. It can be used consistently between experiments and computational work. The chemical models used in this study incorporate all three of these species. Furthermore, no single species concentration is so small that it might create a behavioral margin, which might be difficult to capture and model.

Bench-Scale

The objective of the bench-scale experimental platform was to isolate and examine specific physical and chemical processes either in isolation or in concert with one another, while in a controlled environment where we can use a range of non-intrusive instruments to measure aspects of those processes of interests in a repeatable manner.
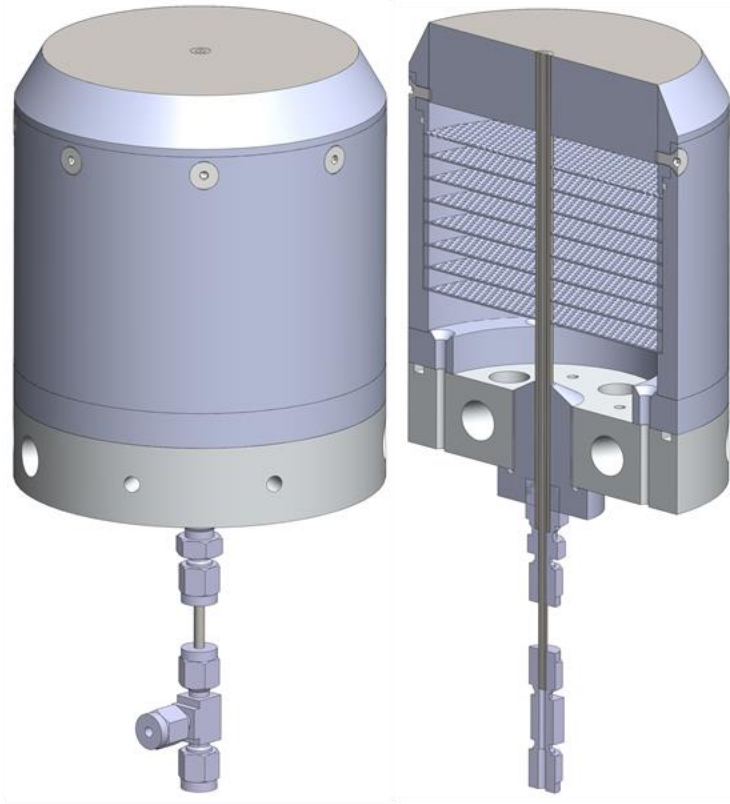
Fig. 16-External and cross-sectional view of the flat flame-stabilized jet and spray burner.

For bench-scale laboratory experiments, a tube burner with capability to have a stabilizing flat-flame pilot was used. The burner, depicted in Figure 16, is a modified version of the spray burner used in a previous BSEE-sponsored program focused on efficient atomization and combustion of emulsified crude oil [91]. In this modified burner, there is a single central tube that delivers the fuel of interest and acts, in effect, as a scaled-down wellhead. The outer section of the burner, which includes a series of perforated metal plates and a honeycomb disk (1 in thick with 0.030 in cells), delivers an approximately uniform outlet flow of either air or a flat pilot flame of hydrogen/air. If a pilot flame is not needed to stabilize the central jet flame, then a co-flow of air is used to supply needed air to mix with the central fuel and burn. If a pilot flame is required to maintain and stabilize the central jet flame, then a mixture of hydrogen and air is used to support a flat flame just above the exit of the honeycomb. The flat flame helps ignite the central fuel jet and provides a source of heat and radical species to stabilize the jet flame.

The diameter of the overall burner exit is 98.9 mm (3.9 in). The central tube, which serves as the simple open-pipe atomizer (OPA), delivers the two-phase fuel flow of interest for the spray flame. It has an outside diameter of 6.4 mm (0.25 in) and an inside diameter of 0.85 mm (0.033 in). The burner is mounted on a three-axis traverse system that enables point-wise interrogation of the region above the burner. Thus, measurements of temperature, velocity, and species concentration can be performed at any point in the region of interest. The burner is supplied by a range of mass flow controllers (MFC) and a pump system that are connected to a data acquisition computer via serial bus connections. The computer both logs and

controls the flow rates as well as recording other instrumentation variables such as temperature, heat flux, etc. Air is supplied by a building-wide air supply system. H_2, CH_4, C_2H_6, and C_3H_8, were supplied from pressurized cylinders. The instruments listed in Table 3 were used to meter and control the flow for the various gases and liquid fuels.

Table 3-List of metering instruments used for the bench-scale experiment.

Stream	Instrument	Model
Co-flow air	MFC	Alicat MCR-500SLPM-D/5M,RIN,5IN,GAS:AIR
Co-flow H_2	MFC	Alicat MCR-50SLPM-D/5M,RIN,5IN,GAS:H_2
Gaseous fuel	MFC	Alicat MCR-50SLPM-D/10M,RIN,10IN,GAS:C_3H_8
Liquid fuel	Metering Pump Motor	Ismatec ISM919A
	Piston Pump	Ismatec UX-07104-66
	Pulse Dampener	Blacoh CTS1120T

Figure 17 shows the design details of the two-phase mixing tee. This assembly needed to produce a thin film of liquid along the inside of the pipe to simulate the uniform filming of a nearly infinitely long wellbore while not introducing unsteadiness into the flow.

(a)   (b)
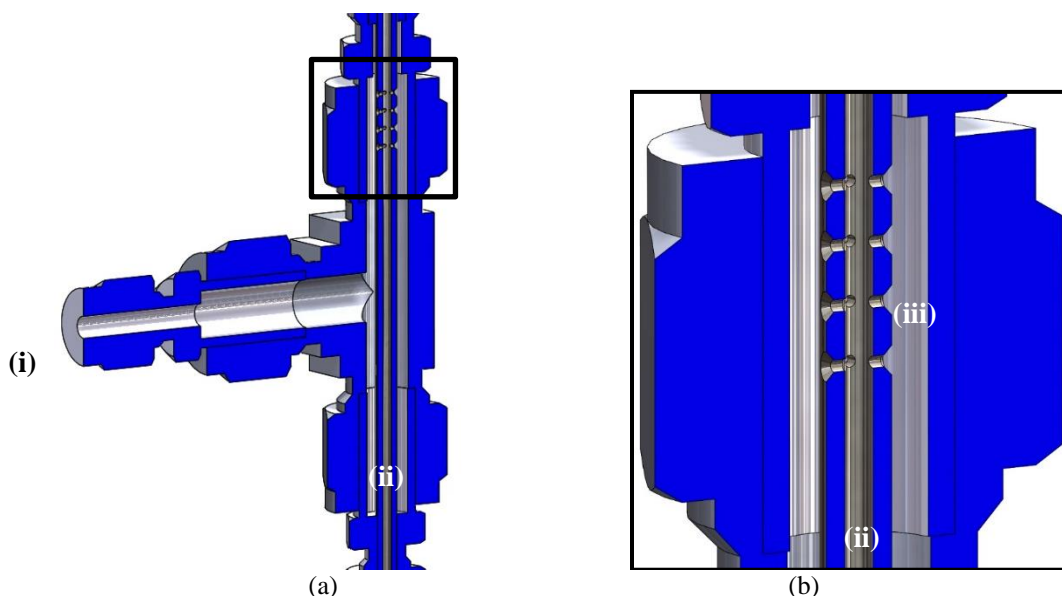
Fig. 17-Cross-sectional images of the (a) entire mixing tee and the details of the (b) mixing section. Liquid flows into the tee through the (i) side port while gas flow from the (ii) bottom along the length of the jet. The liquid then flows through several small ports drilled into the side of the jet (iii) to distribute the liquid into a thin film with a low velocity flow.

Representative photographs of the spray flame for two conditions are shown in Figure 18. The H_2/air pilot flame was, of course, not visible because it lacks any species (e.g., CH, soot, etc.) that emit visible light. The spray flame was clearly visible in both photographs, with some characteristic differences between the two conditions. For the lower ethane flow rate (0.1 g/s), shown on the left, the flame was

anchored at the burner exit and has an extremely narrow plume at the base. For the higher ethane flow rate (0.2 g/s), shown on the right, the flame was lifted and was much broader at its base. The flame was lifted, presumably, because the higher fuel velocity exiting the atomizer tube caused fuel to convect downstream much faster. This required a significant distance for entrainment and mixing with high-temperature excess oxygen (O_2) and radicals from the pilot flame and for the chemical-kinetic reactions to occur. When the fuel velocity was low at the lower ethane flow rate, there was sufficient residence time for fuel-O_2 mixing and chemical reactions such that the flame anchored immediately at the burner exit.
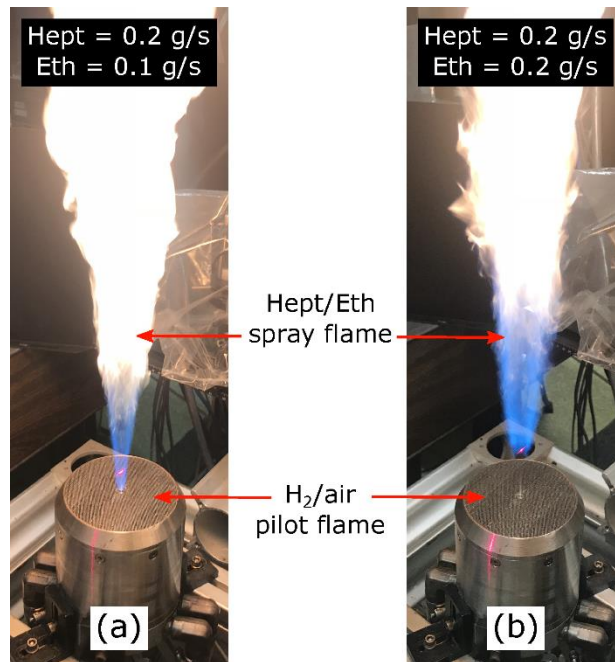
Fig. 18-Photographs of spray flame for two operating conditions: ethane flow rate = (a) 0.1 g/s and (b) 0.2 g/s. For both conditions, heptane flow rate = 0.2 g/s.

Diagnostics Methods
A range of instruments were used to measure spray and combustion behavior. The most important aspects of these behaviors are the droplet behavior and the temperature. A section is devoted to each.

Droplet Behavior

Phase Doppler Anemometry
Phase Doppler Anemometry (PDA) operates using light scattered by a spherical droplet or particle as it passes through a measurement volume formed by crossing two laser beams. The laser beam is first split into two equally powered beams; one beam passes through a Bragg cell oscillating at 80 MHz, which modulates the wavelength for that beam before interacting with the other beam to form the measurement volume. As a result, the interference pattern formed where the beams cross translates in space at a constant rate. When a droplet or bubble passes through the measurement volume, it refracts the light, which is gathered by the receiver and amplified by a photomultiplier. The same applies when a solid particle passes through the measurement volume, except the light is reflected instead of refracted. The signal processor uses the frequency shift in the scattered signal to calculate the velocity.

A schematic of the PDA measurement system is shown in Figure 19. Item (ii) in the diagram is a transmitter that sends out the laser beams, but it also acts as a receiver with optics that collect reflected light. The transmitter actually puts out a total of four laser beams – two 660-nm beams that cross in the vertical plane and provide vertical velocity information (z direction) and two 785-nm beams that cross in the horizontal plane and provide horizontal velocity information (x direction). Item (iii) is a similar dual-purpose unit that transmits two 632-nm beams that cross in the horizontal plane and also collects reflected light to provide additional horizontal velocity information (y direction). The signal processor can also use the phase differences between three spatially separate detectors in a receiver to calculate and validate droplet/particle diameters. This measurement is known as Phase Doppler anemometry (PDA).
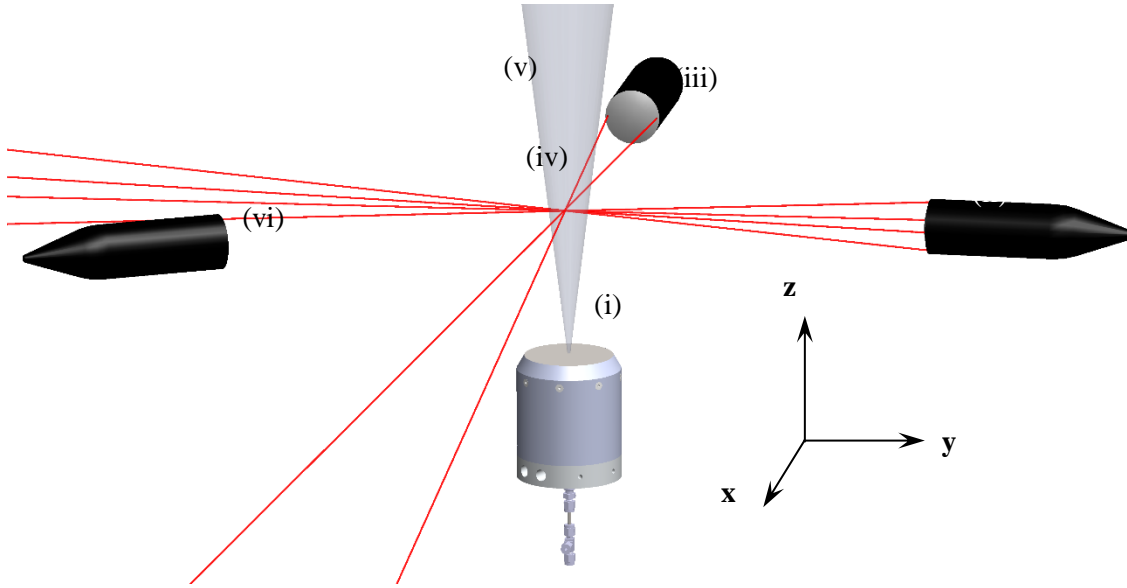
Fig. 19-Phase Doppler anemometry layout of the (i) flat flame jet spray burner with the (ii) two-dimensional PDA measuring in the x and z directions and the (iii) one-dimensional PDA measuring in the y direction at a single (iv) measurement volume, where the lasers intersect, within the (v) plume. The (vi) receiver collects the scattered light.

A two-dimensional phase Doppler anemometry (PDA) system was used to measure droplet diameters and velocities in the spray flame. Measurement principles of PDA are well-documented in the literature and thus are not discussed here. The details of the PDA system used in this study also can be found in the literature [92]. The PDA software was configured to collect 10,000 samples at each spatial location, but with a 10-second time limit. Typically, a precipitous decrease in data collection rate is observed when the measurement reaches and goes beyond the outer boundary of the spray cone. The diameter statistic of particular interest is the Sauter mean diameter (D_{32}), calculated as:

$$SMD = D_{32} = \frac{\sum N_i D_i^3}{\sum N_i D_i^2}$$
(40)

Where N is the number of droplets in a particular statistical bin of the probability distribution and D is the diameter of that bin. Sauter mean diameter (SMD) statistically represents the volume-to-surface area ratio of the droplet distribution, and is an important spray parameter. The two velocity components measured by the PDA system are the vertical (axial) component and one of the horizontal components. The horizontal velocity component is considered to be a radial velocity, since the spray plume is nominally axisymmetric.

This symmetry was examined and confirmed by measuring droplet sizes and velocities for orthogonal horizontal directions at height $z = 20$ mm above the burner.

Diffuse Back-Illumination Imaging

We also implemented a high-speed spray imaging system to complement the PDA droplet studies and to provide insight into the spray breakup and development processes for the OPA. The setup is shown in Figure 20, both in a schematic diagram (top) and a photograph (bottom). The diffuse back illumination (DBI) imaging system implemented in this study comprised of four main components in Figure 20: a high-speed camera (Photron SA-5); a high-speed pulsed LED (ISSI); beam-shaping optics; and a long distance microscope (Navitar Resolve4k). The beam-shaping optics consisted of a 62-mm spherical convex lens (mounted to the pulsed LED), a Fresnel lens, a 1-degree engineered diffuser (RPC Photonics), and a final 400-mm spherical convex lens (not shown). This optical arrangement directed a ~10 × 10 mm^2 beam of light through the multi-phase flow, which was ultimately collected by the long distance microscope and imaged by the camera. The magnification of the long distance microscope was such that each pixel on the camera corresponded to ~5 μm, which allowed liquid objects with a "diameter" of ~20 μm to be resolved.

The principle idea of DBI imaging is simple: A strong, diffuse beam of light is directed through the multi-phase flow and is subsequently imaged by a camera. Due to index of refraction differences between the gaseous and liquid phases, droplets scatter and redirect the light such that it is represented by dark regions on the collected image (i.e., the shadow of the liquid is what is imaged). The diffuse nature of the light, achieved by employing engineered diffusers, serves to mitigate beam-steering and Schlieren effects that result from index of refraction gradients that form between the separate phases of flow as well as where steep temperature variations exist (e.g., near flame fronts) [75]. By equipping the camera with a long-distance microscope lens [75-78,93], liquid objects that are on the order of microns can be resolved and characterized.

1. LED
2. PCX lens (f = 62.90 mm)
3. Fresnel lens (f = 71.12 mm)
4. Engineered diffuser (5° div. angle)
5. Spray burner
6. Zoom lens assembly
7. High-speed camera
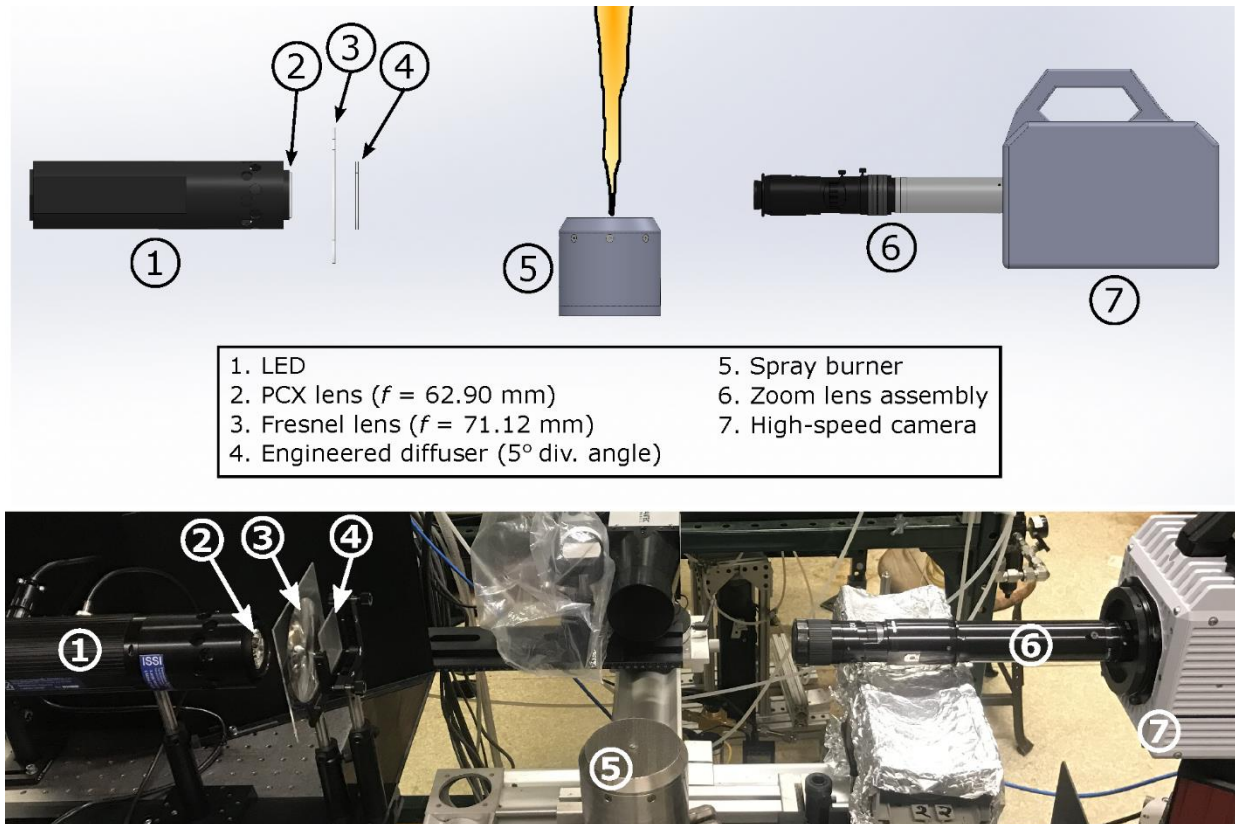
Fig. 20-Schematic diagram (top) and photograph (bottom) of diffuse back-illumination (DBI) high-speed spray imaging setup.

One of the chief advantages of DBI imaging is that it can provide size and velocity information of the liquid phase within optically dense regions of the flow. Moreover, unlike classical liquid phase characterization techniques (such as PDA) DBI imaging can provide detailed information pertaining to non-spherical liquid objects, which tend to dominate in terms of both liquid volume and object number density within the initial injection region of multi-phase flows (i.e., sprays). Accurately characterizing this region is crucial to understanding how sprays evolve downstream (i.e., how they break up, atomize, and ultimately evaporate), which significantly dictates combustion behavior. Since the OPA employed in this study features a very dense and complex multi-phase region at its opening, DBI imaging is an ideal diagnostic t

A unique feature of the specific DBI imaging system employed in this study is that it facilitates the continuous acquisition of images at rates as high as 525,000 frames per second (fps). Laser-based systems, such as those employed in Ref. [78], are not capable of permitting such high framing rates. The advantage of having such high framing rates is that it permits tracking of the temporal evolution of liquid objects (e.g., how their shape and volume changes in time). Also, for slower moving droplets, these imaging rates are sufficient to estimate their velocities. Additionally, high framing rates are needed to resolve and characterize instabilities that may develop as a result of two fluids with vastly different densities moving past each other.

Temperature

Coherent Anti-Stokes Raman Spectrometry-based Thermometry
Coherent anti-Stokes Raman scattering (CARS) spectroscopy is a four-wave mixing technique whereby the Raman active transitions of a molecule are stimulated by a pump and Stokes beam and a signal is scattered by a probe beam [94]. The spectrum in the CARS signal carries a signature of the temperature and concentration of the molecules in the probe volume. Measurements for this program are expected to include temperature and concentration of N_2 in the flame. Since the burner is mounted on a 3D traverse system, spatially-resolved measurements will be made in both the radial and axial directions. In dual-pump CARS (DPCARS) the concentration of other molecules can be interpreted with respect to the concentration of N_2 [95]. DPCARS makes use of a tunable, narrowband dye laser in combination with a broadband dye laser to pump and probe the Raman-active transitions of a secondary, and sometimes tertiary, molecule and simultaneously generate its spectrum in the vicinity of the N_2 spectrum. Using this technique, it may be possible to measure concentrations of CO_2, O_2, and H_2, depending on availability in the flame and the signal-to-noise ratio achieved with the DPCARS system [96,97].

The schematic diagram in Figure 21 illustrates the generation of the Stokes beam and the tunable, narrowband probe beam from the dye lasers which are pumped by the second harmonic (532 nm) of two synchronized Nd:YAG lasers. In addition, a third beam is split from one of the Nd:YAG lasers to provide the pump beam. The energy and polarization of the beams are controlled by half-wave plates and polarizers. Three prisms are mounted on two-axis tilt and rotation stages with high sensitivity to carefully orient the three beams into the flame. A lens with focal length of +300 mm converges the beams creating a probe volume within the flame. The CARS signal (purple beam) is generated from the probe volume and another lens with a focal length of +300 mm is used to realign the beams. Finally, the CARS signal is collected with a spectrometer and CCD camera system. A Stanford Research Systems digital delay generator (DG535) is used to synchronize the Nd:YAG laser lamp and Q-switch triggers as well as the Andor iStar CCD camera.
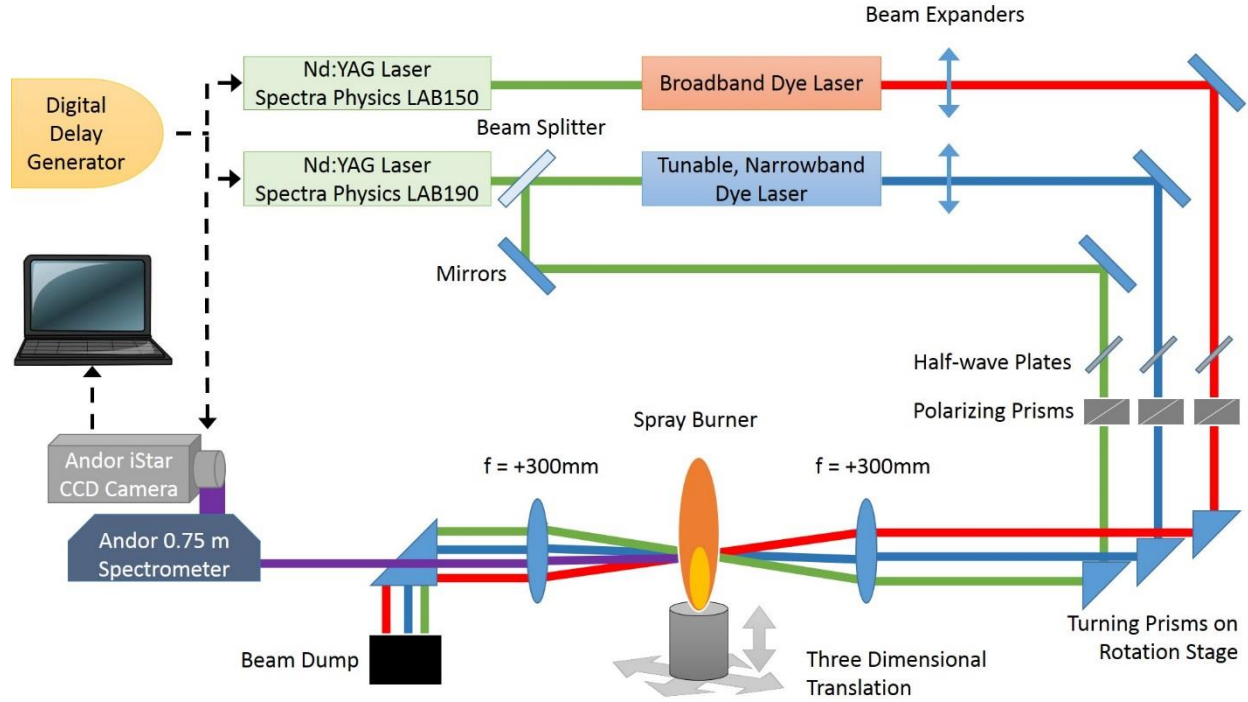
Fig. 21-Schematic diagram of the DPCARS and burner system.

3-Color High-Speed Pyrometry

As part of another program at NRL, Dr. Jacob adapted a spatial thermometry method, which he developed to study nanothermite combustion [98], to measure the temperature of metal particles in a dust flame. We have termed this method 3-color high-speed imaging pyrometry (3CHIP). In contrast to the gas-phase thermometry being done with CARS (or TDLAS described in *Appendix A*), this method measures temperature of *condensed-phase* particles in a flame, such as soot, dust, or powder [98]. Thus, the method is being applied to measure temperature of the soot in the spray flame, which can be compared with gas-phase temperatures obtained via CARS. The method uses Planck's Law to determine temperature based on the relative red, green, and blue intensities of each pixel on the sensor of a conventional or high-speed camera [99-102]. The ratios of the RGB values must be corrected using the camera sensor's known RGB spectral response curves. In addition, to ensure accuracy the method must be calibrated using a blackbody radiation source.

In this method, images recorded with a high-speed color camera (Vision Research, Phantom v310) are processed to extract soot temperature at each pixel, thus providing time-resolved temperature maps. Soot emission is assumed to follow Planck's law, as shown in Equation 41, where L is spectral radiance, λ is wavelength, T is temperature, ε is emissivity, h is the Planck constant, c is the speed of light, and k is the Boltzmann constant.

$$L(\lambda, T) = \varepsilon \left(\frac{2hc^2}{\lambda^5} \right) \left(e^{\frac{hc}{\lambda k T}} - 1 \right)^{-1} \qquad (41)$$

While it is important to characterize the exact dependence of spectral emissivity on wavelength, this would be difficult for the highly turbulent spray flame used in this study. Furthermore, any reasonable emissivity approximation is likely to result in at most 10% deviation in the resulting flame temperature.

Thus, for this work, soot emissivity ($\varepsilon(\lambda)$) is assumed to have inverse wavelength dependence, which is the most commonly assumed relationship.

The 3CHIP method is summarized in Figure 22. A schematic of the imaging setup, which is simply the high-speed color camera and a standard lens capturing images of the spray flame, is shown in Figure 22a. In digital color cameras, the sensor used to capture light is sensitive to wavelengths extending from the ultraviolet to infrared, with a mosaic color filter array placed in front of the sensor to serve as a bandpass of extraneous wavelengths for later reproduction of color via a demosaicing algorithm (see Figure 22b). The most common filter array used in color cameras is of the Bayer pattern, which has filters with peak sensitivities corresponding to the red, green, and blue portions of the visible color spectrum (see Figure 22c). The intensity of the signal captured by the sensor is dependent on the channel gain, pixel area, solid angle, exposure time, lens transmission, spectral power density of the source, and spectral sensitivity of the filter array integrated over the entire spectrum of sensitivity for the camera. As a result, solving for temperature based on intensity of a single color channel becomes inherently difficult as the level of knowledge required for accurate estimations of temperature is prone to error. Alternatively, provided that the aforementioned variables (excluding filter sensitivity) remain constant for images being collected, a ratio of the color channel intensities recorded by the camera can be used to back-solve for temperature as shown below in Equation 42, where χ_i is the normalized spectral response of the camera and ψ_i is the gain of channel i.

$$\frac{I_i}{I_j} = \frac{\psi_i \int L(\lambda,T)\varepsilon(\lambda)\chi_i(\lambda)d\lambda}{\psi_j \int L(\lambda,T)\varepsilon(\lambda)\chi_j(\lambda)d\lambda} \tag{42}$$
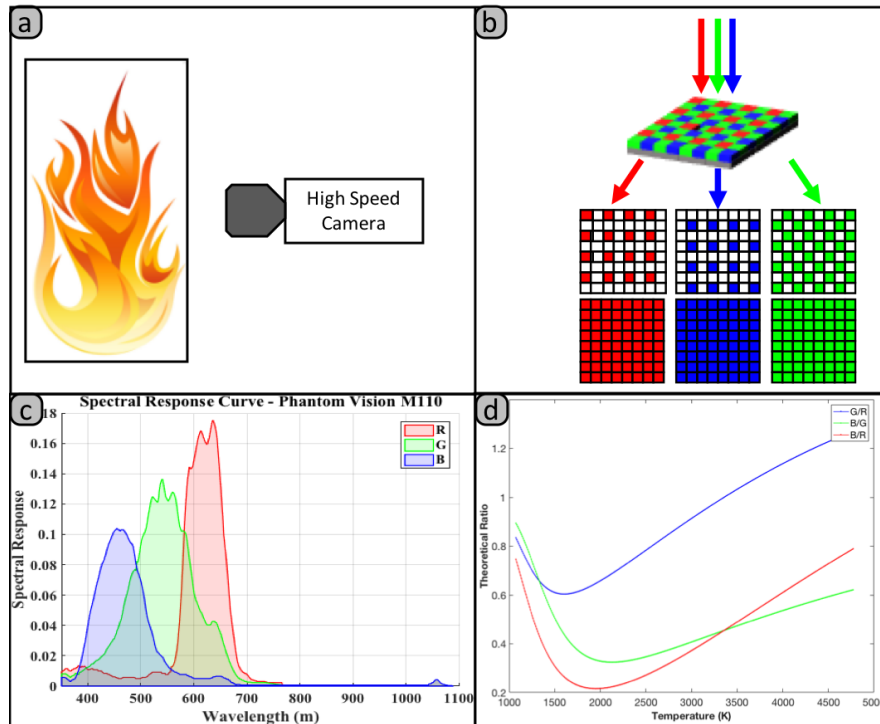
Fig. 22-Illustration of 3-color high-speed imaging pyrometry (3CHIP) method, including: (a) a schematic of the color camera imaging soot emission from the multiphase flame; (b) the Bayer filter on the camera sensor that transmits light within specific bands; (c) spectral response curves of the camera sensor; and (d) theoretically predicted color ratios as a function of temperature using an inverse wavelength dependence on emissivity.

This calculation is performed for a range of temperatures to determine theoretical values for intensity ratios between color channels. A "calibration factor" ($C_{ij} = \psi_i / \psi_j$) for the specific camera/imaging components is then determined by comparing the expected ratios of intensity to those collected from a standardized radiating temperature source. With the assumed inverse wavelength dependence for emissivity, calculation of temperature is then reduced to matching of the calibration factor-corrected ratio of the color channels to the theoretical ratios predetermined for the apparatus (see Figure 22d). This entire operation is carried out for each pixel to assemble a temperature map for each recorded image. While color camera pyrometry does allow for spatiotemporal measurements of temperature, corruption of raw data due to molecular emission is a strong source of error in calculations that are performed. Of the many elements that emit in the visible region of light during thermal relaxation, sodium is often the most noticeable with strong, persistent lines seen as a doublet at ~589 nm. Such emission contributes to the red and green channel intensities, therefore changing the observed ratios in those channels and leading to error in temperature calculations. The simplest way to deal with such interference is through the use of appropriate optical filters. The details of the calibration and image processing method are covered in more detail in a recently published paper [98].

Gas Phase Flame

We will first present the gas-phase flame measurements. Though not strictly similar to oil wellhead fires, they are similar to gas blowout fires and the ability to accurately model and predict gas-phase combustion needed to be verified before proceeding to the two-phase fuel spray flames.

Conditions

We established three experimental conditions for the single-phase gas flame flow rate: 0.1, 0.2, and 0.3 g/s of propane, as shown in Table 4. The hydrogen and air flow rates are 4.2×10^{-2} g/s and 4.4 g/s, respectively, for the co-flowing flat flame. The flow rates vary approximately 1% over time. This combination of flow rates yields a premixed flame with an equivalence ratio (ϕ) of 0.32, which is quite lean and leads to a relatively low pilot flame temperature, as shown below in the results.

Table 4-Experimental matrix of propane jet flame.

Propane Flow Rate (g/s)	Flame Anchor Height from Visible Inspection (mm)	Measurement Profiles Above Burner, z (mm)
0.1	35 – 40	25, 45, 80
0.2	45 – 50	25, 60, 80
0.3	55 – 60	25, 70, 80

Results

CARS – Gas Phase

Figure 23 shows the co-flow flame, propane jet, and CARS measurement in operation. The hydrogen-air flame does not exhibit chemiluminescence in the visible spectrum, thus it is not visible. The propane flame is lifted, as expected. In this image, the CARS beams are focused and directed to a measurement volume above and behind the jet.

N_2 CARS thermometry was demonstrated in a propane jet flame based on the visible flame height produced at three flow rates. As shown in Table 4, the experimental matrix includes flow rates of 0.1, 0.2 and 0.3 g/s of propane. At each flow rate, the flame height was visually approximated by using a ruler held up to the burner. The flame height increased with flow rate and fluctuated approximately ±5 mm. The increase is due to the higher momentum in the jet, which delays mixing and therefore leads to ignition further downstream. For all three flow conditions, radial scans were performed 25 and 80 mm above the

surface of the burner to probe positions under and well above the flame anchor points. In addition, a third radial scan was performed just above the flame anchor point for each condition.
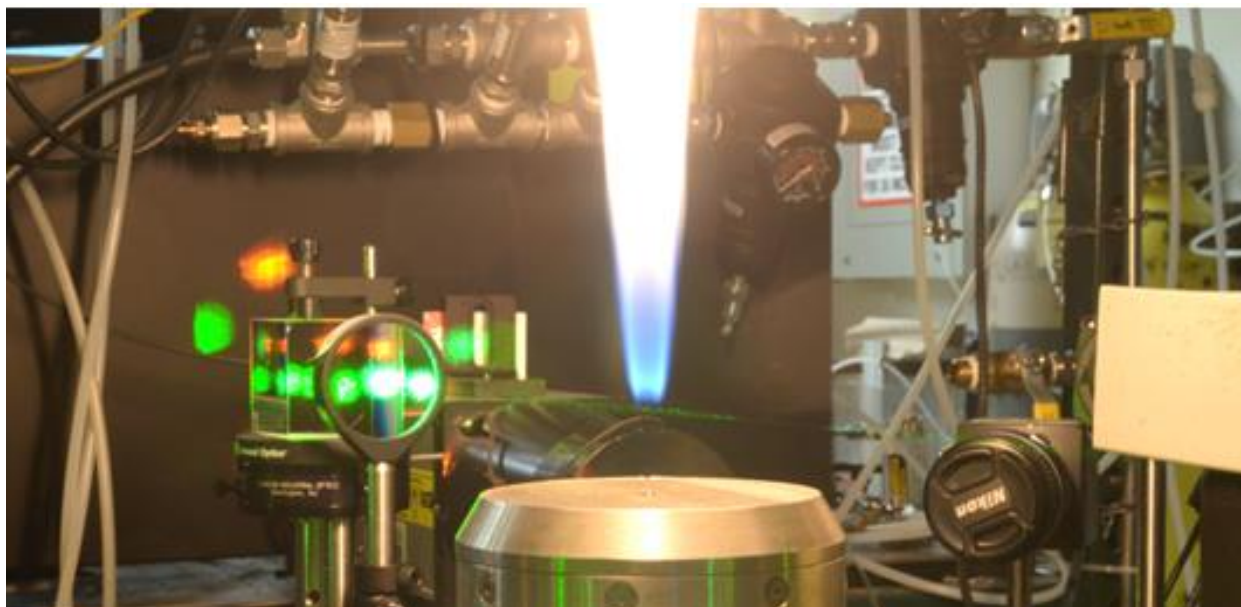
Fig. 23-Photograph of the lifted propane flame from a jet with a 0.838 mm (0.033 in) inside diameter, flowing at 1.00×10^{-4} kg/s, stabilized by a premixed air-H_2 flame at $\phi = 0.31$. The dual-pump CARS beams are visible in the lens and prism in the background.

Because of the interest to capture the thermal gradients at the flame front and because signal to noise ratio decreases with temperature, the grid spacing was set to 0.2 mm and the number of shots averaged was set to 500in the vicinity of the flame front. At positions away from the flame front, the grid spacing was wider and averaged number of shots were lower (1 mm and 300 shots, respectively).

Figure 24 illustrates some of the results obtained using the CARSFT fitting routine, developed by Sandia National Laboratories [6], to fit our experimental data (i) near the center of the propane jet (r = 0.8 mm) under the flame anchor point (z = 25 mm) and (ii) at the flame front (r = 8.0 mm) well above the flame anchor point (z = 80 mm). For this case, propane flow rate was 0.1 g/s and its flame anchor point (liftoff distance) was estimated at 35 – 40 mm.
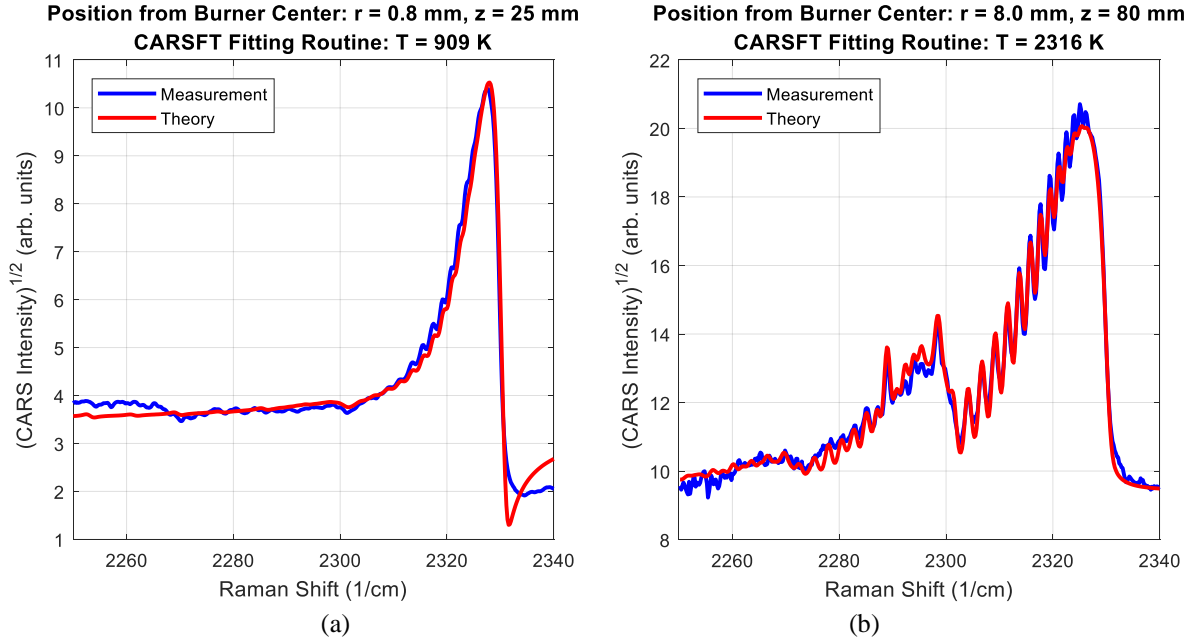
Fig. 24-Sample spectra of N_2 CARS signal with 0.1 g/s of propane (a) near the center of the propane jet under the flame anchor point and (b) at the flame front above the flame anchor point.

In Figure 24a, the CARSFT fitting routine yields a temperature of 909 K at the center of the propane jet. This is at a distance that is below the propane flame anchor point. There are fitting discrepancies toward each end of the profile near 2260 and 2340 1/cm. In Figure 24b, the fitting routine results in a temperature of 2316 K at the flame front. Some minor discrepancies can be appreciated near 2260, 2295 and 2320 1/cm.

The discrepancies in the fitting routine are a result of several factors: averaging spectra in highly fluctuating temperature fields, variable number density, and the shot-to-shot profile differences of the Stokes beam create a changing profile of the non-resonant susceptibility. To remedy these discrepancies we increase the intensity of the Stokes beam so that less shots need to be averaged and increase the breadth of the Stokes beam so that changes in its profile are less problematic.

The discrepancies, however, do not appear to result in major errors in thermometry especially at higher temperatures. The average temperature at each grid point across the radial scans, for the conditions listed in Table 4, was determined and results illustrated in Figures 25-27. These figures show the grid distribution for each radial scan. Scans in the negative direction in increments of 1 mm from the center of the jet up to −5 mm were also performed in an attempt to create a symmetric profile and confirm the location of the center of the flame.
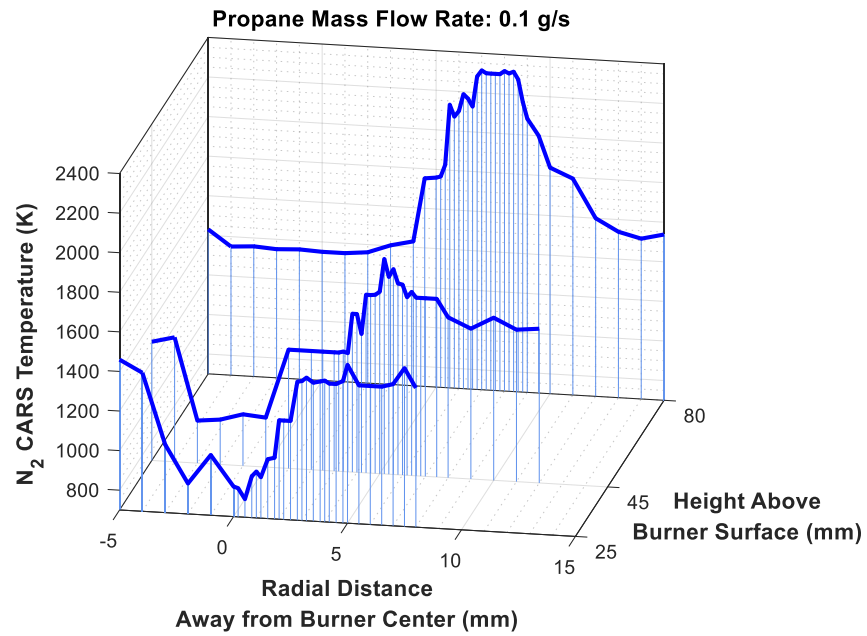
Fig. 25-N$_2$ thermometry results of a jet flame at 0.1 g/s of propane at 25, 45 and 80 mm above the burner surface.
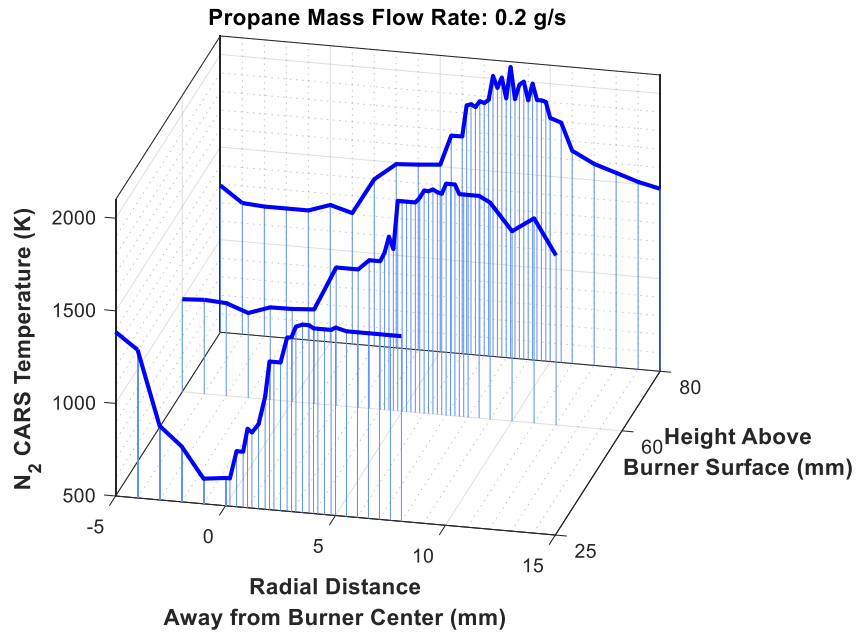
Fig. 26-N$_2$ thermometry results of a jet flame at 0.2 g/s of propane at 25, 60 and 80 mm above the burner surface.
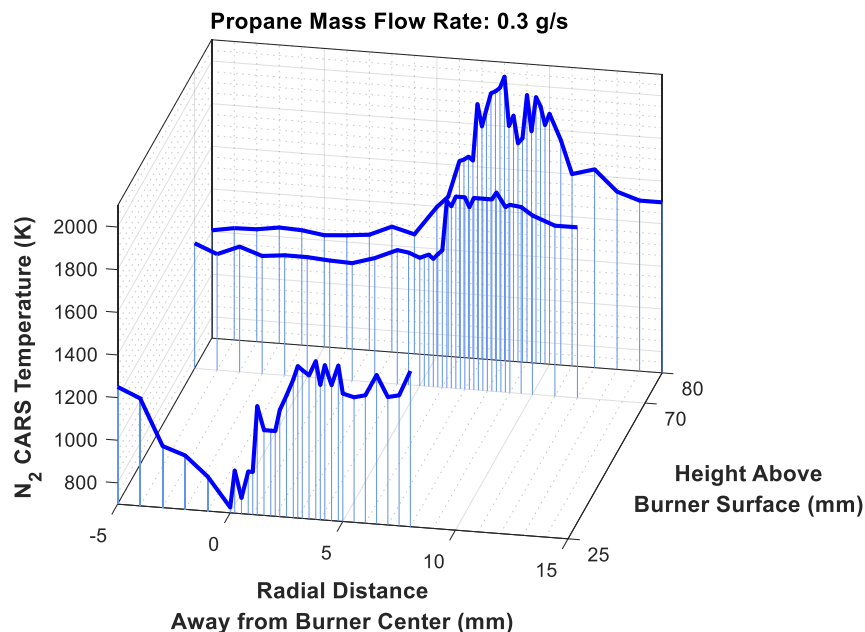
Fig. 27-N$_2$ thermometric results of a jet flame at 0.3 g/s of propane at 25, 70 and 80 mm above the burner surface.

Scans at a height of 25 mm appear to show that the center is approximately −1 mm with respect to the coordinate chosen for these measurements. This is more clearly appreciated in Figure 28a which shows the temperature distribution for each propane flow rate at a height of 25 mm. The region between −2 and +1 mm demonstrated higher discrepancies in fitting theory to measurement. Quantitatively, these results are less reliable. Qualitatively, however, the results can be used to determine the center of the flame.

The results in Figure 28a for the three propane flow rates are very similar. Although the flow rates vary, the temperatures at a height of 25 mm are expected to be relatively the same because these measurements are below the anchor point of the propane flame and it is expected that the premixed H$_2$/air flat flame is the primary thermal influence in this region. The temperature is lowest near −1 mm and increases radially outward reaching a maximum at about −5 and +3 mm to 1400 K. In the region from +3 to +8 mm, the temperature is between 1300 and 1500 K. There is a ±100 K error in these measurements.

At a distance downstream of the fluctuating flame anchor point, the temperature profiles are also expected to be qualitatively similar. This is illustrated in Figure 28b where the thermometric results for the three propane flow rates at a height of 80 mm are shown. The three profiles demonstrate similar shapes with a peak and valley in the same regions having similar widths. With 0.1 g/s of propane, however, the temperature is noticeably higher than at 0.2 and 0.3 g/s. Near the flame center and flame front, the temperature with 0.1 g/s of propane is about 150 K and 350 K higher, respectively. The higher momentum in the profiles with 0.2 and 0.3 g/s of propane may carry colder mass further downstream than the profile with 0.1 g/s of propane resulting in lower temperatures. However, there is no significant difference in the profiles between 0.2 and 0.3 g/s of propane. The three profiles reach 1500 K at +15 mm towards the outward edge of the flame front.

55
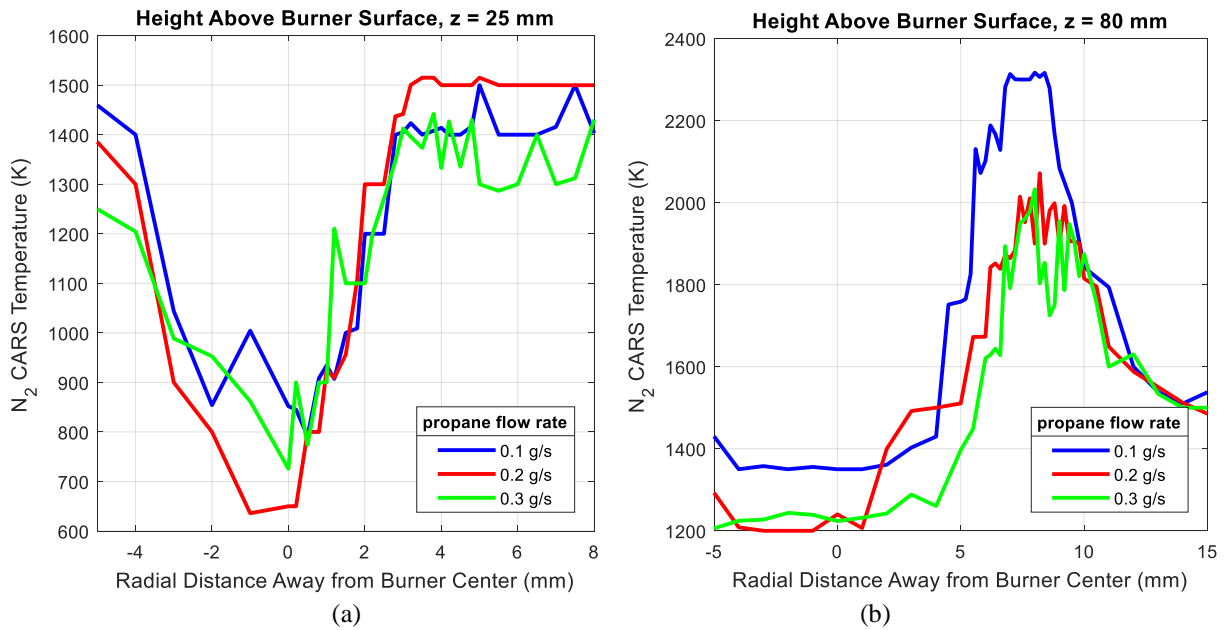
Fig. 28-Thermometric results at a height of (a) 25 mm and (b) 80 mm for all three propane flow rates.

CARS and 3-Color Pyrometry Comparisons

As alluded to earlier, accurate modelling of the combustion dynamics of a two phase system requires estimations of the condensed phase and gas phase temperature measurements as the presence of such temperature gradients would determine the evaporation rate of the suspended droplets in the spray plume. The diagnostics presented in the previous sections are individually capable of measuring the temperatures of the gas and condensed phase soot but before doing so, it needs to be seen whether the two measurements can be corroborated. Therefore, in order to validate the two diagnostics, we used 3CHIP to measure the same sooting propane gas jet flame, operating at 0.01 g/s. The resulting flame structure is shown in Figure 29 along with the regions that were probed using the beam. Also shown in Figure 29 is the processed condensed phase temperature map using 3CHIP technique, incorporating the inverse emissivity approximation, for a single frame.
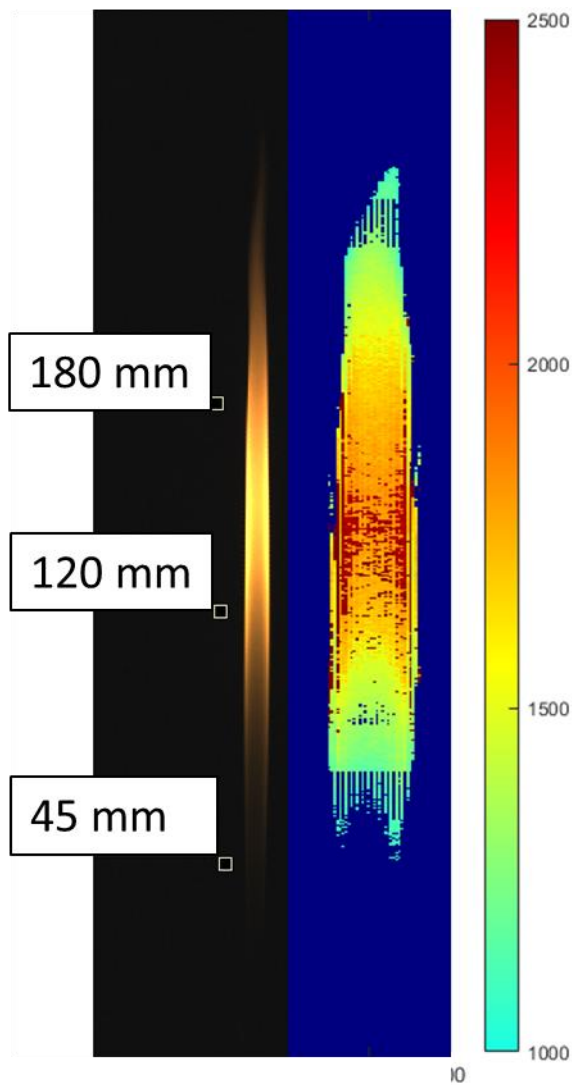
Fig. 29-(left) Propane 0.01 g/s- Air 4.4 g/s jet flame used for comparisons between 3CHIP and CARS measurement with the respective datatips showing the height above burner at which CARS was used to probe the gas phase temperature. (right) 3CHIP processed condesed phase temperature map of the image on the left with the colorbar representing the temperature range.

As can be seen the condensed phase temperatures are observed to rise initially with height till about 120-150mm after which it appears to cool off. Owing to the poor signal at 45mm location, 3CHIP measurements at this location was not validated against CARS measurement. Given that CARS measurement involves averaging the spectra from 1000 shots, we found it necessary, for the sake of an accurate comparison, to average the 3CHIP temperature map over 1000 images and the results are presented in Figure 30 for 120 and 180mm above gas inlet in the burner. As can be seen the results show reasonable overlap at 120 mm for the two measurements, with the CARS technique probing the N_2 gas temperature and 3CHIP probing the condensed phase temperature from soot radiation. The 3CHIP measurement, being a line of sight integration method, displays abnormally high temperature artifacts at the flame edge and subsequently drop off, mainly due to the poor signal at these radial positions. Currently we are working on employing inverse Abel transforms to deconvolute the line of sight integrated signal so that the edges could be better resolved. As we move further up to 180 mm, the gas phase temperature is observed to rise by ~

200 K whereas the condensed phase temperature is observed to drop, which is expected as the soot conducts heat to the surrounding gas thereby heating the ambient gas. Further work needs to be done to understand the heat transfer dynamics of soot during this cool down period, which could help explain the observed differences in temperature.
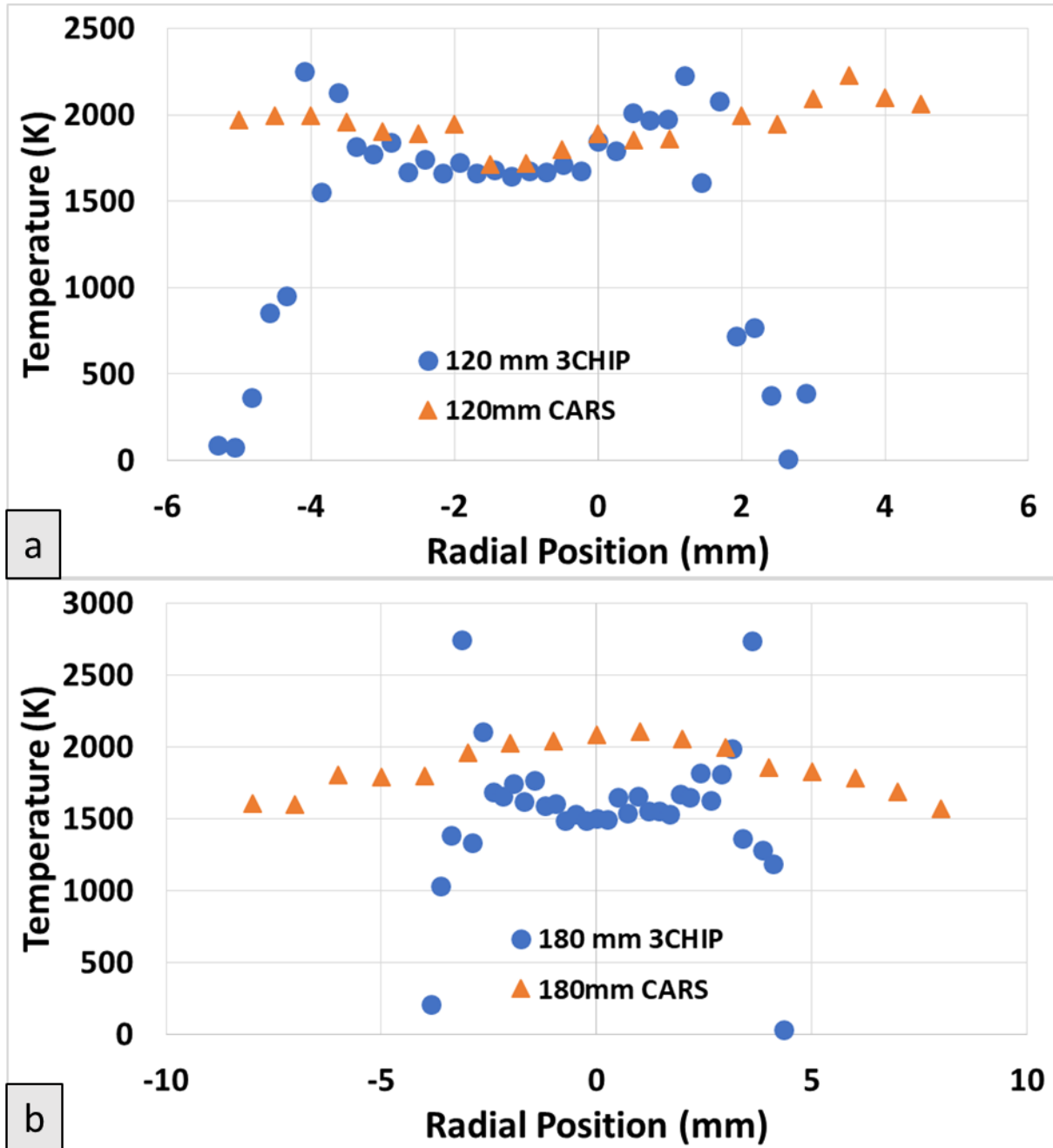
Fig. 30-Radial 1D temperature plots of Propane jet flame using CARS and 3CHIP for (a) 120 mm and (b) 180 mm.

Spray Flame

Once we had validated the gas-phase temperature measurement techniques, we focused our attention and time on the bench-scale spray flames. The following sections outline the conditions and results.

Conditions

The spray flame conditions are described in Table 5 for the two-phase spray flame conditions. In addition to the reacting or burning conditions, we also examined fundamental spray behavior using air and water. Though not comparable for the spray far downstream ($Z/D > 20$) of the jet, the near-field air and water behavior is analogous to that of the ethane and heptane behavior where little mixing or reaction has taken place. Table 6 describes the axial and radial locations where PDA measurements were made.

Table 5-List of spray burner operating conditions for PDA and DBI. L:G represents the liquid to gas loading ratio, U_G is the superficial velocity of the gas, Re_G is the superficial gas Reynolds number based on U_G and the diameter of the pipe, Re_L is the superficial liquid Reynolds number

Gas (g/s)	Liquid (g/s)	(L:G)	$U_{G,S}$ (m/s)	Re_G	Re_L	HRR[1] (kW)
Air	Water					
0.1	0.2	2.00	151	8677	314	-
	0.4	4.00			629	-
	0.6	6.00			943	-
	0.8	8.00			1257	-
	1.0	10.0			1572	-
0.2	0.2	1.00	303	17354	314	-
	0.4	2.00			629	-
	0.6	3.00			943	-
	0.8	4.00			1257	-
	1.0	5.00			1572	-
0.3	0.2	0.67	344	26031	314	-
	0.4	1.33			629	-
	0.6	2.00			943	-
	0.8	2.67			1257	-
	1.0	3.33			1572	-
0.4	0.2	0.50	344	34708	314	-
	0.4	1.00			629	-
	0.6	1.50			943	-
	0.8	2.00			1257	-
	1.0	2.50			1572	-
Reacting						
Ethane	Heptane					
0.1	0.0	0.0	146	16401	0	4.75
	0.1	1.0			378	9.24
	0.2	2.0			756	13.7
	0.4	4.0			1512	22.7
0.2	0.0	0.0	292	32802	0	9.50
	0.1	0.5			378	14.0
	0.2	1.0			756	18.5

[1] HRR = heat release rate, assuming LHV of 47.489 MJ/kg for ethane
and 44.926 MJ/kg for heptane [103]

Table 6-Descriptions of PDA data profiles acquired for each burner condition.

Profile description	Spatial locations
Axial, along radial centerline ($r = 0$ mm)	$z = 6$ mm; $z = 8$ mm $z = 10$ mm to $z = 50$ mm, in 2.5-mm increments
Radial, at height $z = 10$ mm	$r = -4.5$ mm to $r = +4.5$ mm, in 0.5-mm increments
Radial, at height $z = 20$ mm	Outer zone: $r = -5.5$ mm to $r = -2$ mm, in 0.5-mm increments Central zone: $r = -2$ mm to $r = +2$ mm, in 0.2-mm increments Outer zone: $r = +2$ mm to $r = +5.5$ mm, in 0.5-mm increments
Radial, at height $z = 30$ mm	$r = -6$ mm to $r = +6$ mm, in 0.5-mm increments

Results

Phase Doppler Anemometry

Five experimental cases for the ethane and heptane from Table 5 were studied for PDA. Two ethane mass flow rates were studied (0.1 g/s and 0.2 g/s), with multiple heptane flow rates studied for each to examine different liquid/gas mass ratios. For the higher ethane flow rate of 0.2 g/s, it was not possible to operate above a heptane flow rate of 0.4 g/s due to the high heat release rate (HRR) and limitations on laboratory exhaust capabilities. Idealized compressible-flow calculations suggest that the lower ethane flow rate (0.1 g/s) leads to subsonic flow conditions inside and exiting the OPA tube, while the higher ethane flow rate (0.2 g/s) approaches a choked condition and possibly leads to supersonic flow exiting the OPA tube.

For each flame condition listed in Table 5, several droplet measurement profiles were acquired. Descriptions of the profiles are included in Table 6. An axial profile was recorded along the burner radial centerline ($r = 0$ mm), from $z = 6$ mm to $z = 50$ mm in 2- to 2.5-mm increments. Radial profiles were recorded at three different heights: $z = 10$ mm, 20 mm, and 30 mm above the burner. For the profiles at $z = 10$ mm and $z = 30$ mm, a constant increment size of 0.5 mm was used. For the profile at $z = 20$ mm, however, a finer increment size of 0.2 mm was used in a "central zone" from $r = -2$ mm to $r = +2$ mm to more closely examine the spray for any interesting behavior or details. It was not possible to make measurements closer than 6 mm above the burner because of the geometry of the laser beams used for the PDA measurements. For distances closer than 6 mm, one of the two laser beams that propagate and cross the measurement point in the vertical plane would be blocked, thus preventing PDA measurements.

In order to understand and model a turbulent spray flame, it is important to have an understanding of the basic size, shape, and structure of the spray. This can be accomplished through several different experimental methods, including PDA of the spray droplets and different types of high-speed spray imaging. In this study, spray geometry and structure were inferred from PDA measurements. Shown in Figure 31 are radial profiles of droplet concentration, at three different heights and for two different flame conditions; shown in Figure 32 are radial profiles of droplet trajectory angle at three different heights for all five of the flame conditions. Concentration is not a primary measurement made by the PDA system, rather it is derived from a count of droplets passing through an estimated measurement volume. Thus, there is a high degree of uncertainty in the concentration measurement. Nevertheless, even ignoring the absolute concentration values, spray structure can be inferred from these profiles. Droplet trajectory angle was calculated using the following relationship:

$$Traj.Angle = \ tan^{-1}\left(\frac{V}{U}\right) \qquad (43)$$

Where *U* is the axial velocity component and *V* is the radial velocity component, thus the computed trajectory angle is with respect to the vertical direction.
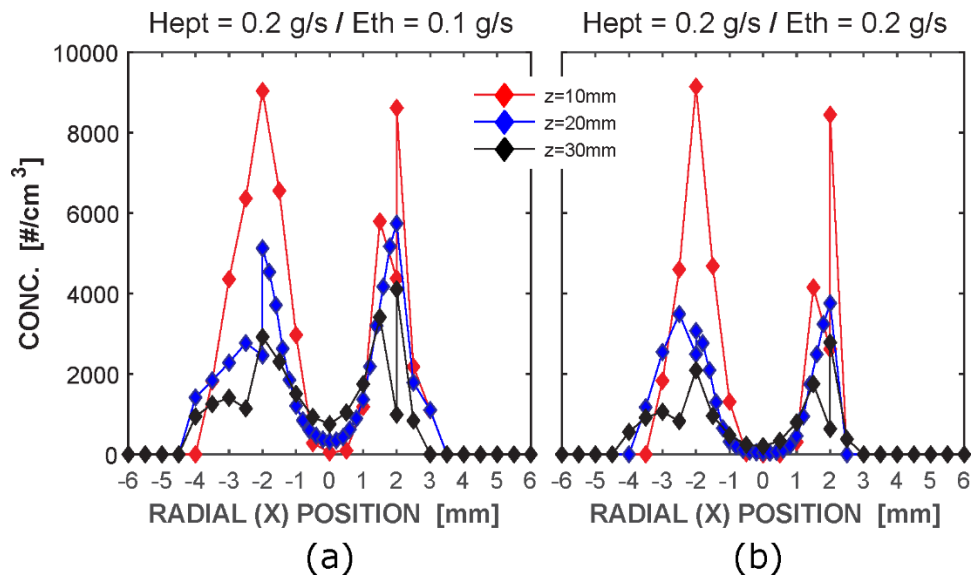
Fig. 31-Radial profiles of droplet concentration for two flame conditions: ethane flow rate = (a) 0.1 g/s and (b) 0.2 g/s. For both conditions, heptane flow rate = 0.2 g/s.
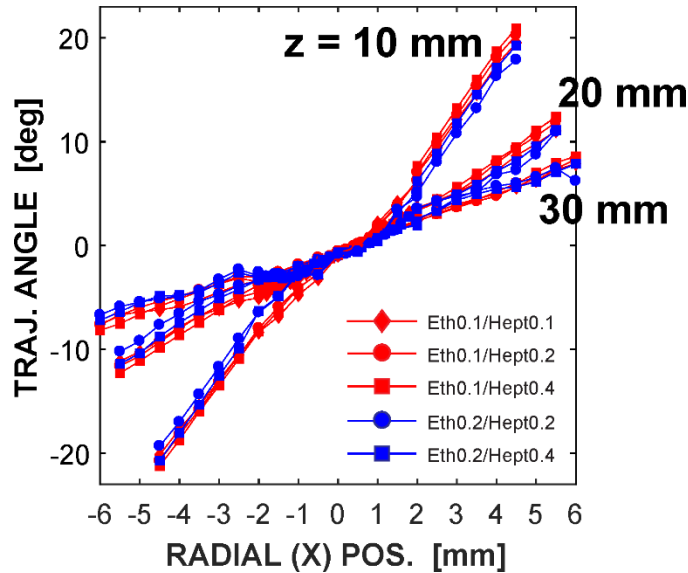
Fig. 32-Radial profiles of droplet trajectory for all five flame conditions.

For both flame conditions, and at all heights, droplets are concentrated in an annular region spanning from approximately *r* = ±1 mm to *r* = ±3-4 mm, as shown in Figure 31. The highest concentrations are generally found at *r* = ±2 mm. Outside of *r* = ±4 mm, regardless of height, there are essentially no droplets at all, which indicates a very narrow spray plume that does not broaden or diverge much with distance from

the exit. Near the center axis, within the central zone between the high concentration peaks, PDA suggests that the droplet concentrations were non-zero but very low. From the DBI results, we will see that it much more likely that the PDA system was not able to reliably measure the central droplets because of their high speed and the high optical density. This will be corrected by using a higher speed PDA system to capture the faster droplets with a higher power laser that will increase the signal to noise of droplets in high optical density regions of the flow that would have been previously much lower and rejected. We will explore the spatial distribution of the liquid in our discussion of the DBI results. The concentration profiles suggests that the OPA is, in fact, characterized by annular flow, with liquid mainly concentrated in an annular film around a central gas core. The lower concentration of droplets in the center is consistent with the concept of entrainment of droplets due to wave instability of the liquid film and shear interactions between the high-velocity gas and the low-velocity liquid [34,35].

Trajectory angles in Figure 32 reinforce the observation that the spray plume is quite narrow. At the lowest height, $z = 10$ mm, the spray included angle is only approximately $\pm20°$, and it only gets narrower from there. At $z = 20$ mm, the included angle has narrowed to $\pm12°$, and at the highest height, $z = 30$ mm, the included angle has narrowed to $\pm7°$. In addition, there appears to be little influence of flow/flame conditions on the spray width. There is a tendency for the spray to be slightly narrower for higher ethane flow rate, and for it to be slightly wider for higher heptane flow rate, but these trends are minimal.

Spray behavior is characterized by droplet sizes and velocities, and how these quantities vary throughout the spray. Axial profiles of droplet size (both Sauter mean diameter and arithmetic mean diameter) and axial velocity (U) along the spray centerline ($r = 0$ mm) are shown in Figure 33 for all five flame conditions. Droplet sizes are only shown for heights at and above $z = 10$ mm, as measurements below this height were unreliable due to sparsity of droplets. The same characteristic velocity behavior is seen for all five conditions: droplets decelerate with increasing axial distance, as expected for a high-pressure jet issuing into atmospheric conditions. There is little difference in centerline droplet velocity with changes in heptane (liquid) flow rate, but there is clearly a strong dependence on the ethane (gas) flow rate. There was no direct measurement of gas-phase velocity in these experiments, but there must be a significant increase in velocity associated with the significant increase in ethane flow rate. Since the spray exits to atmosphere, it is assumed that the ethane gas density, at the relevant heights for these measurements, remains the same for different flow rates. Mass flow rate is the product of density, velocity, and area, thus if gas density and flow area remain nominally constant, velocity must increase at the same rate as mass flow rate. The velocity does not quite double along with the flow rate, so there is likely a slight increase in ethane density for the higher flow rate condition.
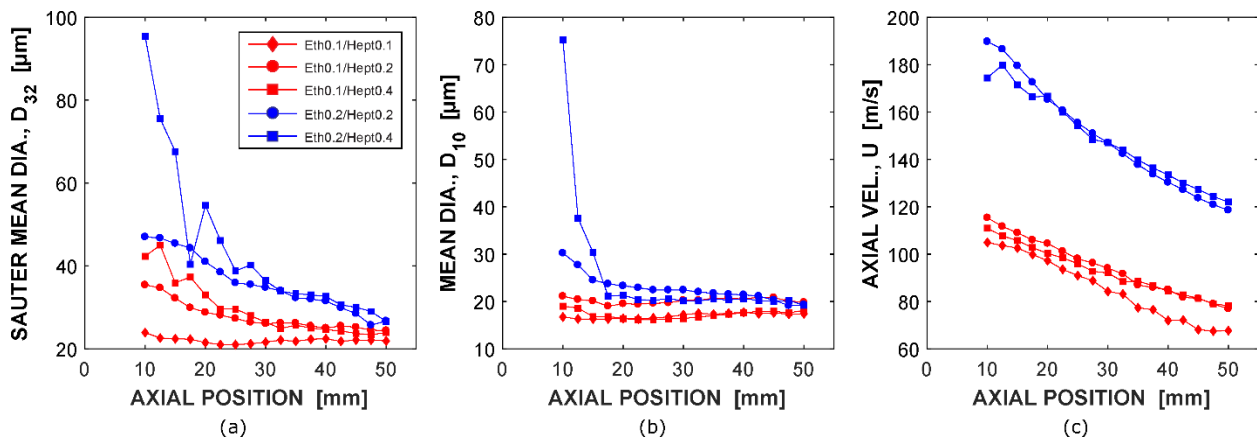
Fig. 33-Axial profiles of droplet (a) Sauter mean diameter (D_{32}), (b) mean diameter (D_{10}), and (c) axial velocity (U) along the radial centerline of the spray plume ($r = 0$ mm), for all five flame conditions.

Based on the Sauter mean diameters shown in Figure 33, it is tempting to conclude that droplets steadily decrease in size with increasing axial distance. Sauter mean diameter can be misleading, however, as it can be skewed by a small number of very large droplets. That is exactly the case here, as it is clear that the arithmetic mean diameters, with few exceptions, are nearly constant with respect to axial distance. Just as with velocity, centerline droplet diameters are affected very little by heptane (liquid) flow rate. Unlike with velocity, however, centerline droplet diameters are also relatively insensitive to ethane (gas) flow rate.

Radial profiles of droplet size (both Sauter mean diameter and arithmetic mean diameter) and axial velocity (U) at three different heights and for all five flame conditions are shown in Figure 34. With respect to the ethane and heptane flow rates, the same basic trends are seen in these profiles as were observed in the axial profiles in Figure 33. The influence of heptane (liquid) flow rate on droplet size is minimal, and the influence of ethane (gas) flow rate is stronger but still not appreciable. Ethane flow rate only affects droplet size in the outer zones away from the centerline. Ethane flow rate has a strong effect on droplet axial velocity at and near the centerline, but in the outer zones velocities are nearly identical for all conditions. In addition, the inner zone around the centerline, within which droplet sizes are nearly identical for all conditions but droplet velocities are strongly influenced by ethane flow rate, widens as axial distance (i.e., height) increases. At $z = 10$ mm, the inner zone spans approximately ±1.5 mm; at $z = 20$ mm, it spans approximately ±2 mm; at $z = 30$ mm, it spans approximately ±3 mm.

It is also seen in Figure 34 that as height increases, droplets in the inner zone decelerate but change little in size. These inner zone droplets are not evaporating quickly, presumably, due to the abundance of surrounding cool fuel vapor. In the outer zone, on the other hand, mean and Sauter mean diameters slightly increase and axial velocity remains nearly the same as height increases. The slight increases in D_{10} and D_{32} are, counterintuitively, due to droplet evaporation, as the smallest droplets evaporate quickly and the larger remaining droplets skew the size distribution. Evaporation occurs in the outer zone because these droplets are exposed to heat from the spray and pilot flames and to product gas from the pilot flame that has no fuel vapor.
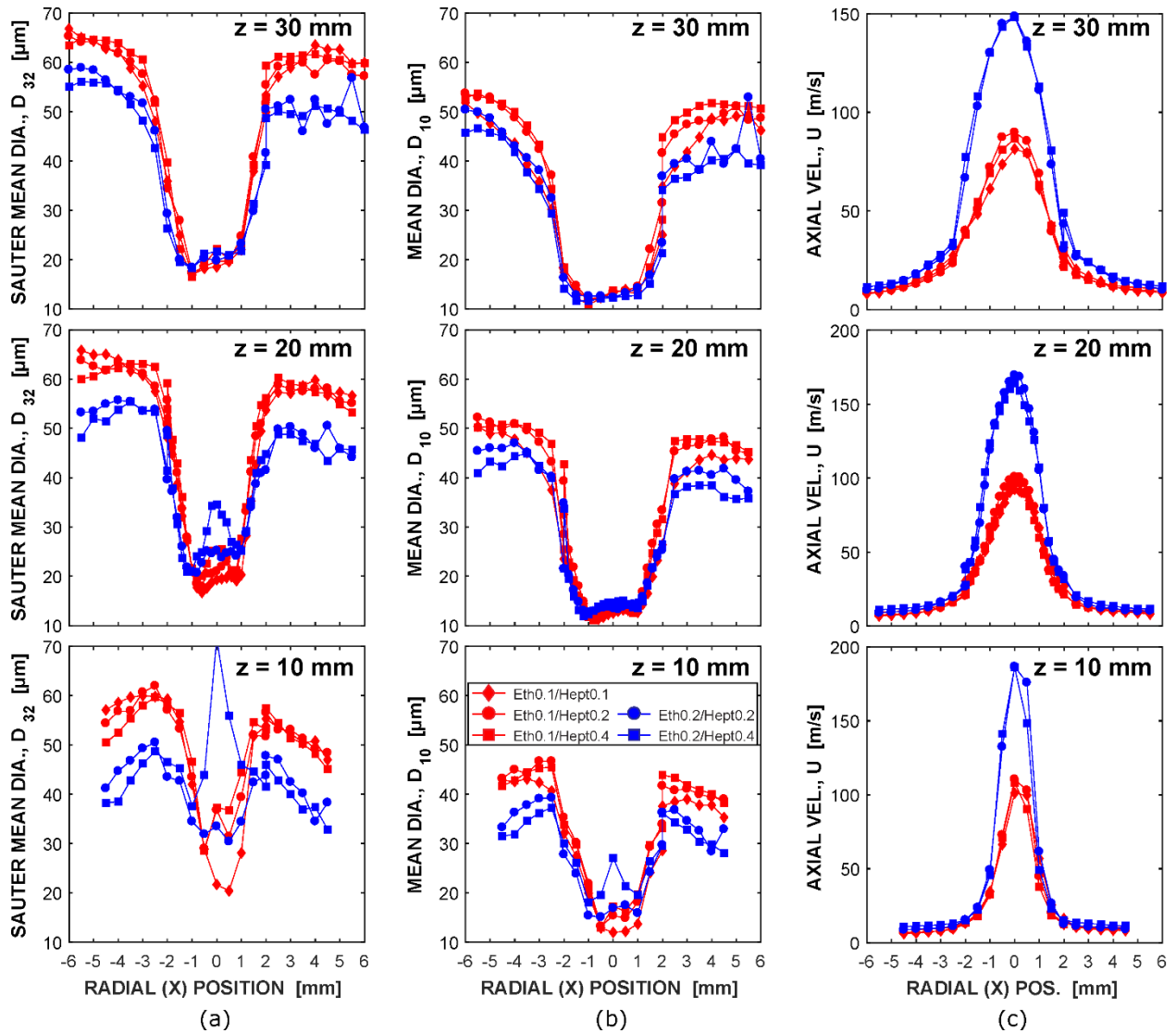
Fig. 34-Radial profiles of droplet (a) Sauter mean diameter (D_{32}), (b) mean diameter (D_{10}), and (c) axial velocity (U) at three heights ($z = 10$ mm, 20 mm, 30 mm), for all five flame conditions.

For a closer examination of the spray characteristics, droplet size and velocity histograms are shown in Figures 35 through 37. Results for three flame cases are included to illustrate behaviors across a range of conditions; results for the other two conditions are similar. For each height, distributions are plotted for three radial locations: in the central zone ($x = -1$ mm), in the transition region ($x = -2.5$ mm), and in the outer zone ($x = -3.5$ mm). At each radial location, an increase in velocity is observed with increasing height. This is expected based on the radial profiles in Figure 34, despite the fact that the centerline velocity decreases with increasing height. The velocity profiles broaden, with radial locations away from the centerline experiencing increasing velocity with increasing height. More importantly, it is clear from these distributions that there are two distinct zones, just as the previously discussed profiles suggest. The central zone, near the centerline, is occupied by droplets that are very small and fast-moving. In contrast, the outer zone is occupied by droplets that are significantly larger and moving much more slowly. At the lower heights ($z = 10$ mm and 20 mm), there is a sharp transition between central and outer zones. Both the droplet

sizes and velocities at $x = -2.5$ mm, which appears to be in a transition region in the radial profile plots (Figure 34), are nearly identical to those in the outer zone at $x = -3.5$ mm.

It is noted that a bimodal velocity distribution is sometimes observed, such as in the middle panel of Figure 37b ($z = 20$ mm, $x = -1$ mm). In such cases, it appears that the two observed velocity modes are simply the characteristic velocities in the central and outer zones, and they are both observed because turbulence causes both modes to intersect with the finite probe volume during the seconds-long data acquisition process. At the highest height ($z = 30$ mm), there is more of a gradual transition of droplet sizes and velocities with increasing radial distance. This is expected, since the spray jet decelerates, spreads out, and entrains pilot flame product gas with increasing height. These experimental results provide strong supporting evidence that there is annular flow inside the atomizer tube, with smaller droplets in the central zone shedding from the liquid film and entraining into the central flow and larger droplets in the outer zone forming due to atomization of the liquid film itself.
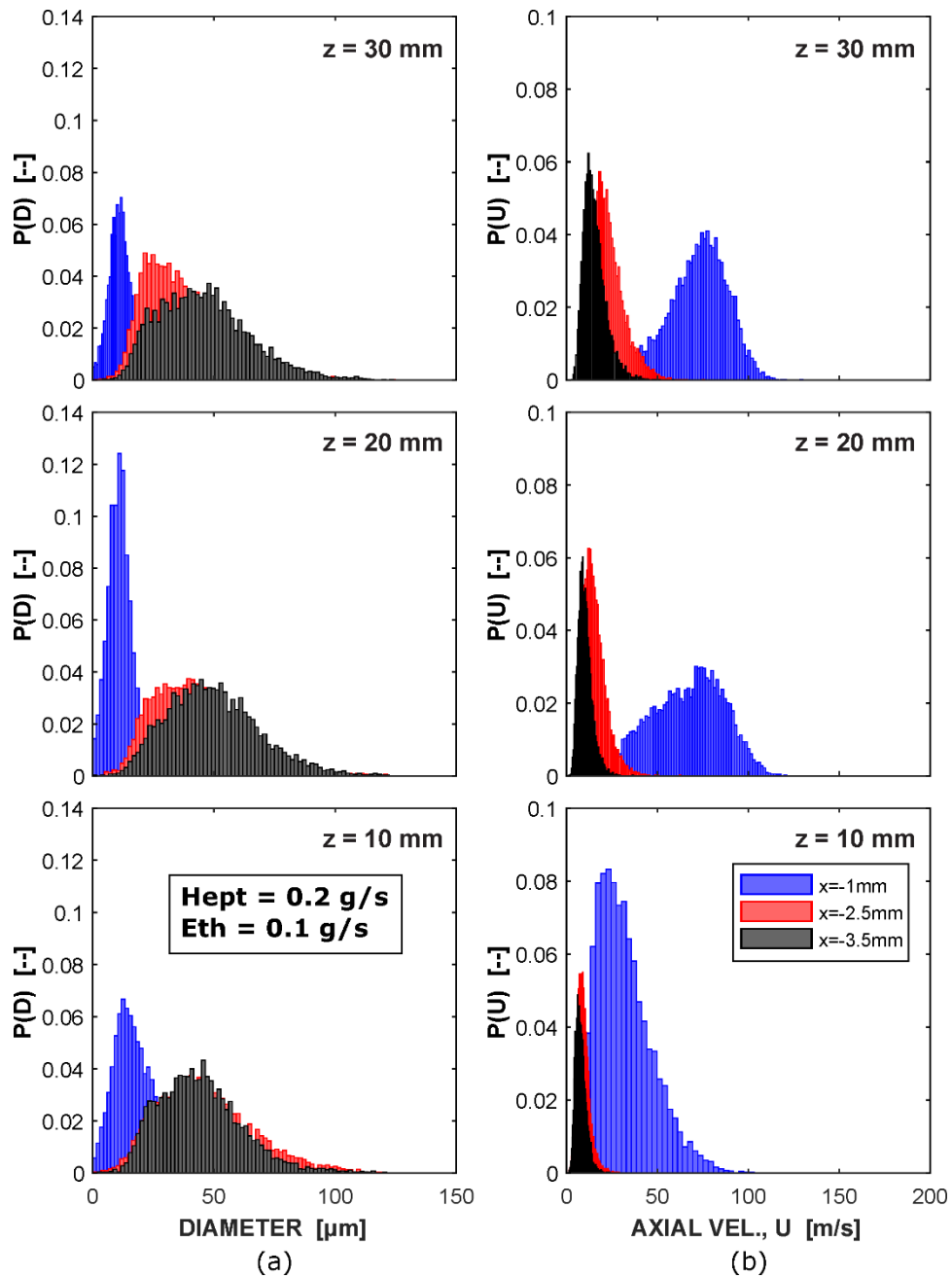
Fig. 35-Histograms of (a) droplet diameter (*D*) and (b) axial velocity (*U*) for selected radial locations, at each of three different heights (*z* = 10 mm, 20 mm, 30 mm). Heptane flow rate = 0.2 g/s; ethane flow rate = 0.1 g/s.
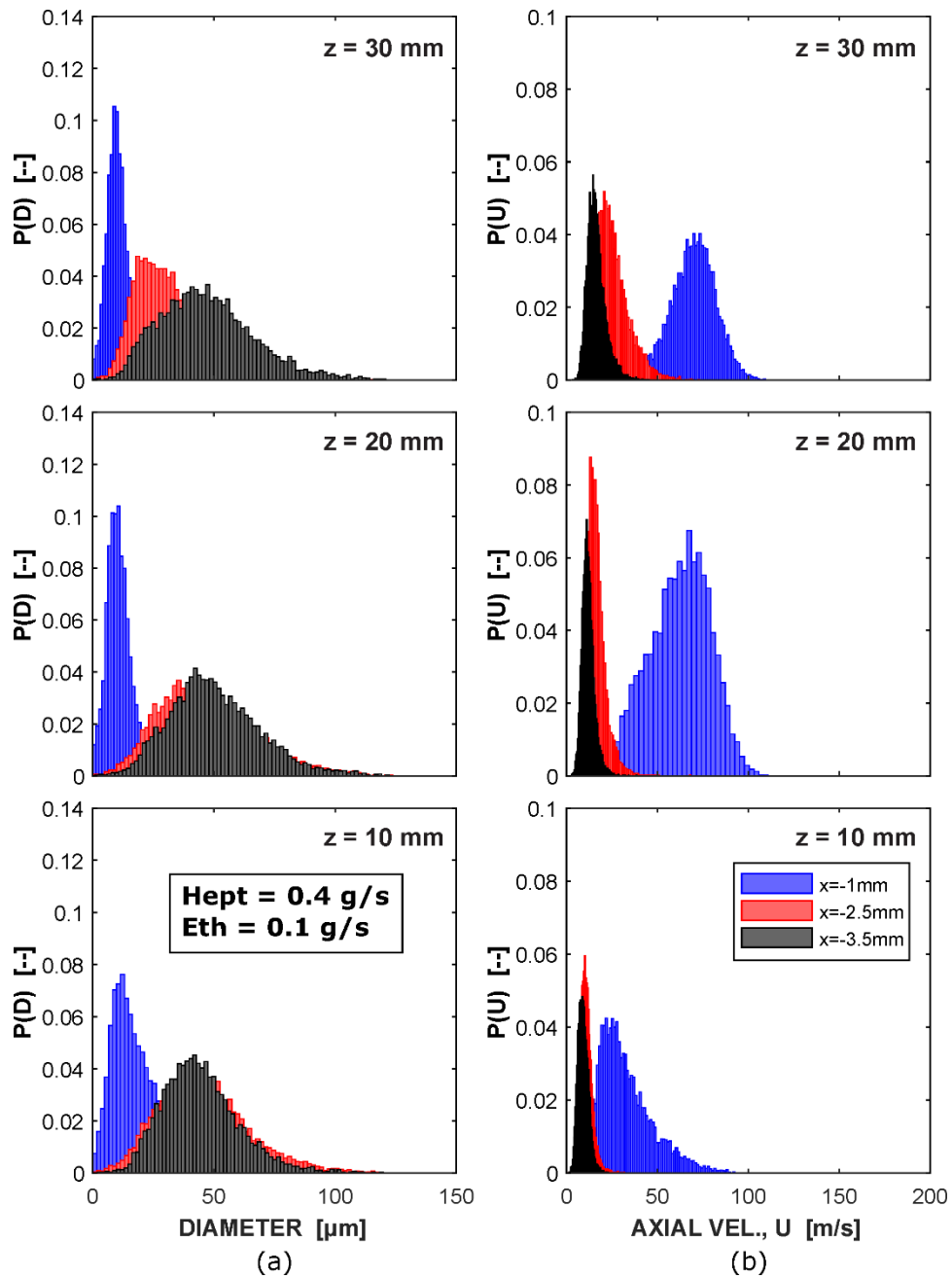
Fig. 36-Histograms of (a) droplet diameter (*D*) and (b) axial velocity (*U*) for selected radial locations, at each of three different heights (*z* = 10 mm, 20 mm, 30 mm). Heptane flow rate = 0.4 g/s; ethane flow rate = 0.1 g/s.
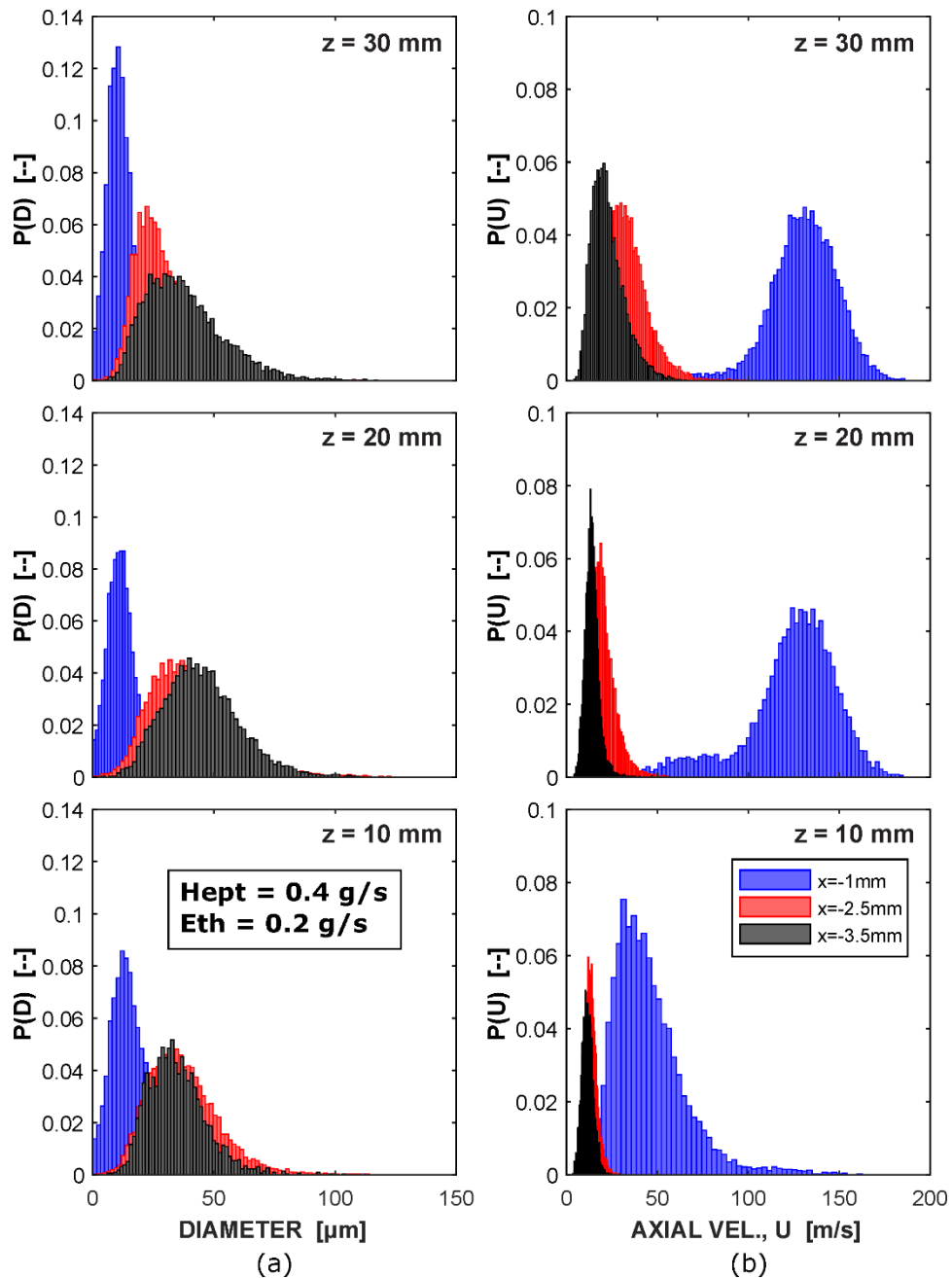
Fig. 37-Histograms of (a) droplet diameter (*D*) and (b) axial velocity (*U*) for selected radial locations, at each of three different heights (*z* = 10 mm, 20 mm, 30 mm). Heptane flow rate = 0.4 g/s; ethane flow rate = 0.2 g/s.

Diffuse Back-Illumination Imaging

Using this instrumentation, a series of liquid and gas flow rates were considered under both non- and reacting conditions. A list of these conditions is provided in Table 5. For non-reacting conditions, the gas-phase flow consisted of air and the liquid phase flow was comprised of water. In the reacting cases, the gas-phase flow consisted of ethane fuel and the liquid was heptane. The flows that issue from the OPA have bulk velocities in excess of 100 m/s. Stabilization of flames produced by such high-speed flows, is achieved

by implementing a large-diameter (99 mm), lean (equivalence ratio of 0.3), premixed H_2-air pilot flame that surrounds the OPA [104].

Initial measurements were gathered using a wide view to both validate the method and provide a view of the behavior between the exit of the OPA and the region 10 mm above the nozzle where PDA measurements were possible. We gathered these data at six conditions relevant to the current laboratory-scale research: two ethane (gas-phase fuel) flow rates (0.1 and 0.2 g/s); three heptane (liquid-phase fuel) flow rates (0.1, 0.2, and 0.4 g/s) for each ethane flow rate. These conditions overlap with those used in the PDA droplet study described above. Figure 38 shows one sample image from each of the six conditions. The top of the burner and atomizer tube are visible near the bottom of each image. For some of the conditions, namely for ethane flow rate of 0.1 g/s, the spray flame was attached to the burner. In the images, however, no flames are visible for any of the conditions. This is because DBI imaging is an extinction method where liquid droplets scatter and/or block light, while gas molecules, flames, etc. have no discernible effect.
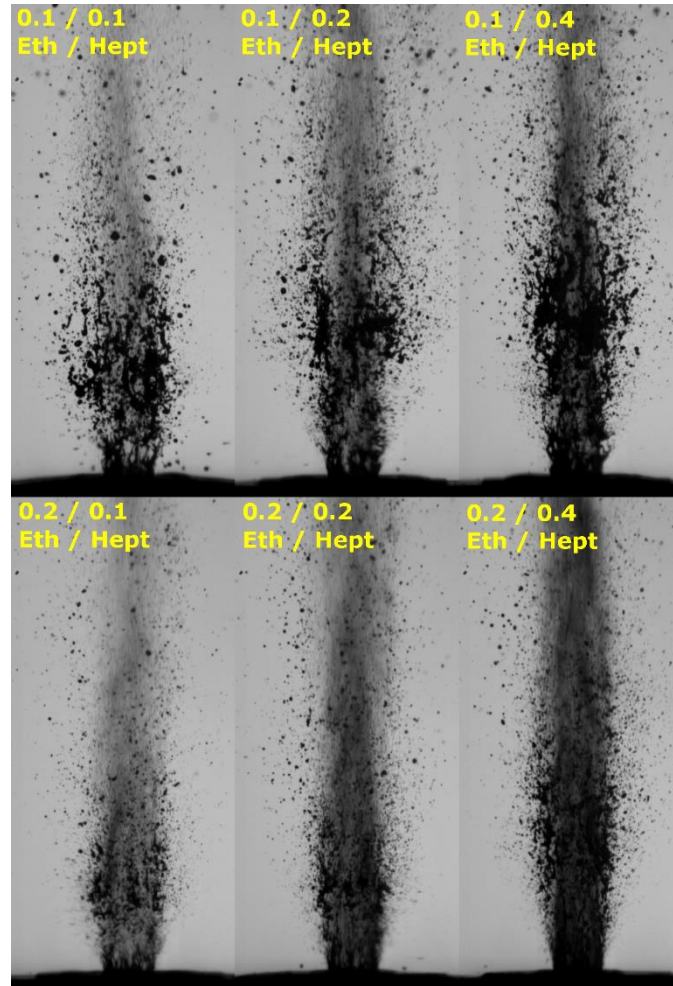
Fig. 38-Sample images from high-speed videos recorded for each of the six test conditions. Top row: ethane flow rate = 0.1 g/s. Bottom row: ethane flow rate = 0.2 g/s.

The images shown in Figure 38 support the idea that these sprays result from annular flow within the atomizer tube. There are clearly two zones of behavior visible in the images – an inner zone with tiny droplets that cannot be individually distinguished at the current spatial and temporal resolution, and a surrounding outer zone with large liquid fragments, ligaments, blobs, and droplets. These images also illustrate differences between the experimental conditions. For the higher ethane flow rate (0.2 g/s, bottom row), the central zone appears darker, suggesting higher droplet concentrations or greater entrainment rates. In addition, the central zone is progressively darker as heptane flow rate increases (from left to right), also suggesting higher droplet concentrations. On the other hand, the outer zone appears somewhat less dark for the higher ethane flow rate, which would seem to suggest perhaps a thinner liquid film inside the atomizer tube for those conditions. This trend is consistent with the film correlation in Equation 2 that shows a decreasing film thickness with increasing Re_G and increasing film thickness with increasing Re_L [31].

Figure 38 shows images that represent snapshots of the spray behavior for each experimental condition. The sprays, however, are transient and turbulent, which is precisely the motivation for performing high-speed imaging. Figure 39 shows a time sequence of images recorded for ethane and heptane flow rates of 0.1 g/s and 0.4 g/s, respectively. To save space, the particular sequence shown only includes every other image captured, as indicated by the time stamps that increment by twice the period between each recorded image (35.7 µs).
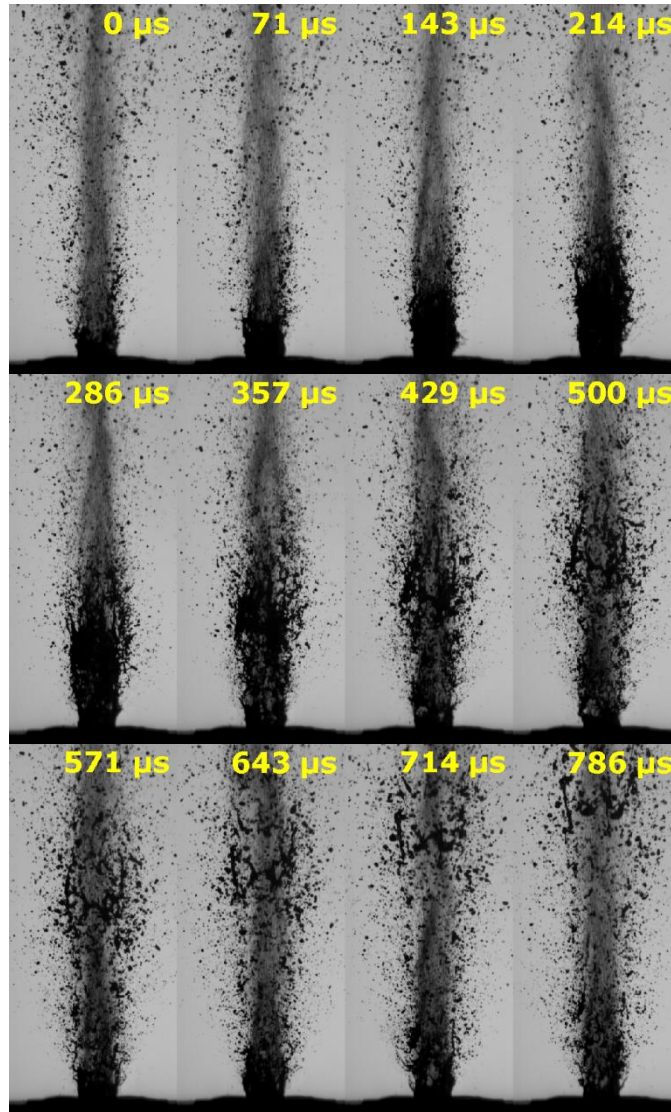
Fig. 39-Time sequence of images. Ethane flow rate = 0.1 g/s; heptane flow rate = 0.4 g/s.

The image sequence shown in Figure 39 was chosen to illustrate a repeating cycle of behavior observed in the high-speed spray videos. We are developing post-processing methods to analyze the behavior and its variance with experimental conditions, and a qualitative description is given here. Periodically and with apparent regularity, the annular liquid film exiting the atomizer tube surges upward, giving the appearance of continuous liquid over a much longer distance. In Figure 39, the liquid surge begins in the second image ($t = 71$ μs) and progresses up through the fifth image ($t = 286$ μs). In the sixth image ($t = 357$ μs), the dense annular liquid has begun to shear into large ligaments, fragments, and blobs. In the next 3 images, up to $t = 571$ μs, these ligaments progress upward and gradually break apart. In the final images, the ligaments break up significantly and progressively more large droplets are seen. This completes the cycle, and after some period of time where the images appear similar to the first image in Figure 39, the cycle begins again. This cyclic behavior, in general, was observed for all conditions, though the frequency and "strength" appears to vary between conditions. We expect to formulate a scientific journal paper describing the spray behavior for this atomizer in the near future.

71

A comparison of the spectra for the different air-water conditions from Table 5 is shown in Figure 40. The field of view (FOV) focused on ½ of the atomizer and was further cropped to only consider a ~1.5 mm^2 region near the exit of the pipe. Each image was thresholded (to distinguish the liquid from the gas/surroundings) and subsequently converted into a binary image where liquid regions were represented by 1s and the rest was set to 0. Then the total liquid area in each image was summed to produce a unique value for that image. For each case a total of 28,125 images were considered, which corresponds to a total sample time of 1.125 seconds. Spectral analysis was then performed via application of fast-Fourier transforms to the total area vs. time data of each case. Results from this analysis are plotted Figure 40.
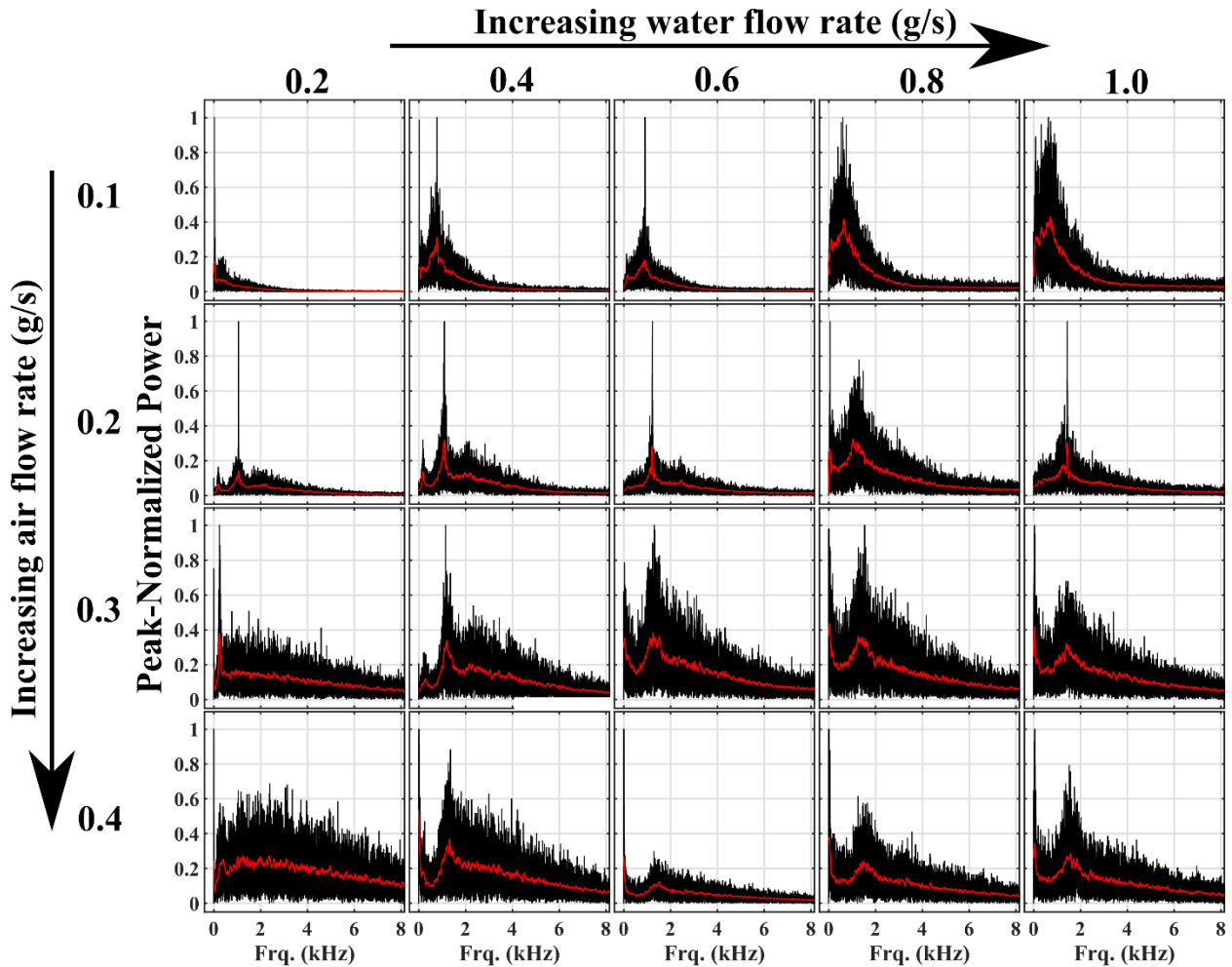
Fig. 40-Spectra for the separate cases considered. Not that the red line is a filtered version of the black line.

From Figure 40, it is clear that the cases exhibit a range of features. Some cases exhibit one strong peak near ~ 1 kHz, others exhibit a strong peak only at low frequencies (< 100 Hz), many exhibit both features, and the peaks observed near 1 kHz then to be broad. While no clear trend is apparent from Figure 40, if we plot the frequency associated with the two most power peaks observed in the filtered spectra in Figure 40 (i.e. the red lines) as a function of the liquid bulk velocity (U_L) a slight trend emerges, shown in Figure 41.
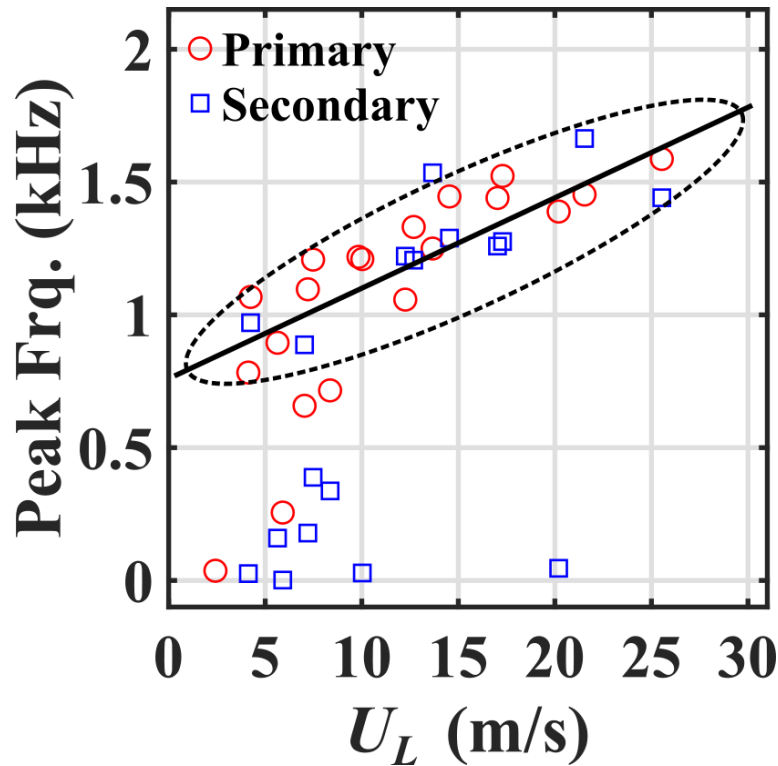
Fig. 41-Primary (largest) and secondary (2nd largest) peak frequency values from spectra in Fig. 1 vs. the liquid bulk velocity derived using the film thickness correlation from Berna *et al.* [31].

In Figure 41, red circles and blue squared represent the frequency of the most and second most powerful peaks in the spectra of Figure 40, respectively. These are plotted against U_L, which is derived based on the mass flow rate and density of the liquid as well as the area it flows through. Here, the latter is estimated by obtaining the film thickness from the correlation proposed by Berna *et al.* [31].

From Figure 41, it is clear that many of the data points exhibit a positive correlation with increasing U_L. There are exceptions/outliers, however. For instance, the peak frequencies at lower liquid velocities almost appear to follow a separate trend than those at larger U_L. This may be the result of: 1) a "regime" change (e.g. from sub- to supersonic gas flow, primarily entrained to fully annular, etc.), 2) failure of the above correlation to accurately capture the film thickness at low liquid velocities, or 3) inadequacies in the measurements/experiment.

In addition to examining the atomizer effluent from a view that also included a large section of the near-field plume, we also zoomed in to where the liquid was ejected from the OPA. In this region, the initial droplets are formed and then they are convected downstream. A sample image from the application of the aforementioned diagnostic system to multi-phase flows issuing from the OPA is displayed in Figure 42. The liquid objects are depicted as the dark regions. Such regions outlined in red represent liquid that is still attached to the exit of the OPA. While objects outlined in purple have separated and dispersed from the atomizer. To identify and characterize individual droplets, a novel images processing algorithm was developed. A schematic representation of the steps involved in this algorithm is presented in Figure 43.
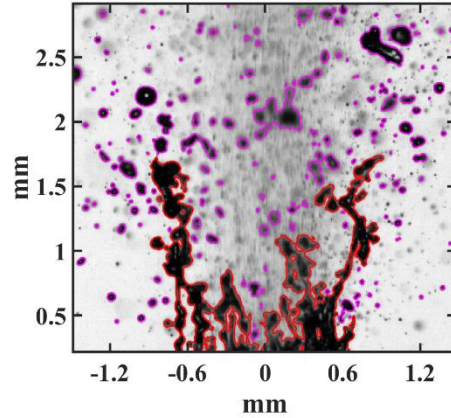
Fig. 42-Sample DBI image take near the exit of the OPA for a condition with 0.2 g/s of air and 0.4 g/s of water.
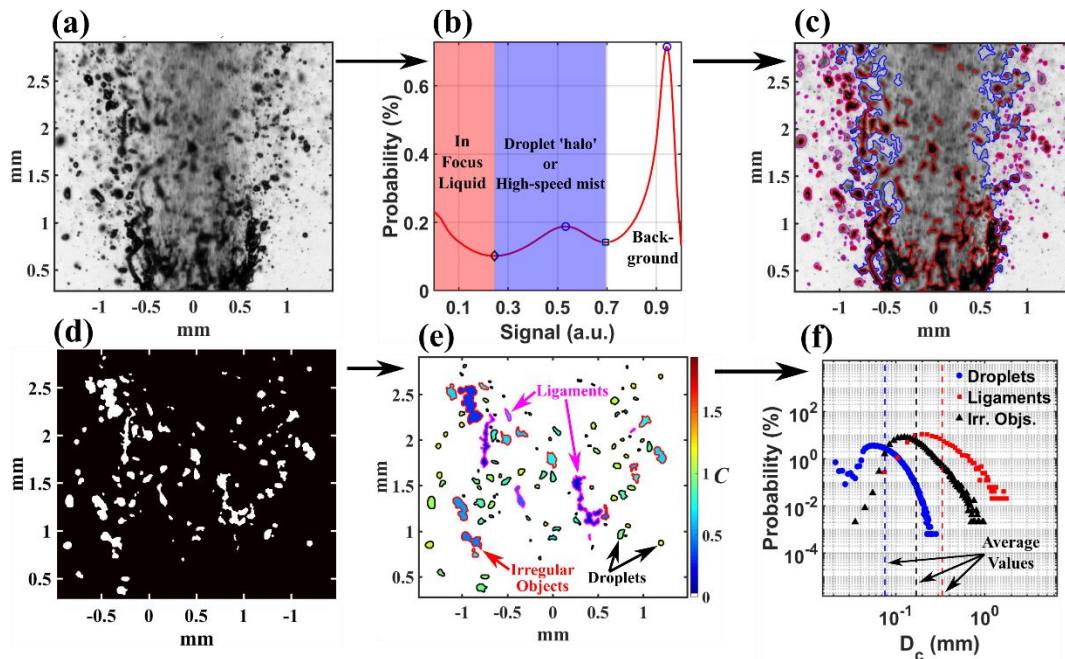
Fig. 43-Depiction of thresholding and binarization scheme applied to diffuse back-illumination images. (a) Raw spray image, (b) PDF of image intensity from entire data set, (c) Raw images with in-focus and 'halo' droplet regions outlined in red and blue, respectively, (d) binarized image, (e) binarized image where the color indicates the circularity (C) and the black, magenta, and red boundaries outline droplets, ligaments, and irregular objects, respectively, and (f) example PDF of the characteristic diameters associated with the separate objects in (e).

By applying the steps outlined in Figure 43 to the images collected in these efforts, statistics pertaining to the size of liquid objects, conditioned on their geometric features, can be obtained. Additionally, statistics regarding the average dispersion angle and breakup distance of the liquid phase is determined from the result of these efforts. Combined, such information serves to increase understanding of the influence primary and secondary liquid break-up has on combustion phenomena. Moreover, it provides a high-fidelity database which numerical models can be developed from and validated against.

74

A large dataset of DBI images has been obtained for the conditions listed within Table 5 and the primary algorithms to process these data have been developed. Thus, the next step is to finish processing of the collected data (which exceeds 2 TB) and to consolidate the information into multiple manuscripts. Additionally, through the course of the prior efforts, a novel approach to tracking the temporal evolution of droplet information was discovered. Namely, the fact that the DBI imaging system employed here permits measurements at ultra-high-speed framing rates (>500 kfps) allows individual droplets to be tracked in time. An example of this is provided in Figure 44, which presents a sequence of DBI images collected at a rate of 75,000 fps. It is clear from this figure that individual liquid objects can be observed in at least 5 consecutive frames, allowing statistics to be generated as a function of time. Additionally, liquid object pairs can be identified in two successive frames through the use of non-rigid image registration algorithms [105,106]. This has the potential to permit estimations of the velocity of the individual liquid objects. However, further work is necessary to finalize algorithms capable of exploiting the high temporal frequency of the collected images.
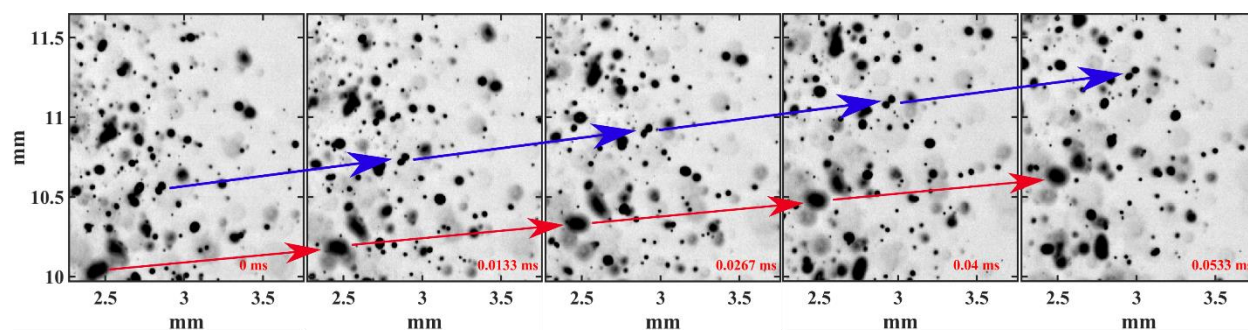
Fig. 44-Sample sequence of DBI images obtained at 75,000 fps, highlighting the potential to track liquid objects in space and time.

CARS – Two Phase

We have also gathered and processed CARS-N_2 thermometry data to measure the temperature distribution within the spray plume for a number of conditions. A good portion of the data has been processed, but the complete set is still pending. For reference, we have provided example profiles in Figure 45. If we examine the lowest profile, at 5 mm above the burner plan, we see that the temperature hovers around 1400 K. There is some radial and temporal variation, but the temperatures are at or above that of the H_2-air co-flow flame. If is unclear if the variation is due to measurement uncertainty, but it seems more likely that the jet produces a static pressure depression that both pulls in the hot products from the co-flow burner as well as drives a toroidal mixing that brings spray combustion hot products back down to the burner. Some particle image velocimetry would confirm or deny that hypothesis.

At 50 mm, Drs. Skiba and Tuesta collected data at two different resolutions on either side of the flame. This allowed us to see the sharp temperature jump across the flame as well as the increased temperature at the center of the plume. We can see that the highest temperature (1918 K) approaches the adiabatic flame temperature of around 2200 K, but as we can expect with non-adiabatic conditions, the temperature is appreciably lower. We can attribute the large amount to scatter in the measurement to the turbulent variation of both the temperature and the location of the flame.

The z = 200 mm profile shows similar scatter, but we did not gather a high-resolution gradient. We observe significant asymmetry in this profile that we have yet to explain or understand, because the flame appeared symmetric visually.
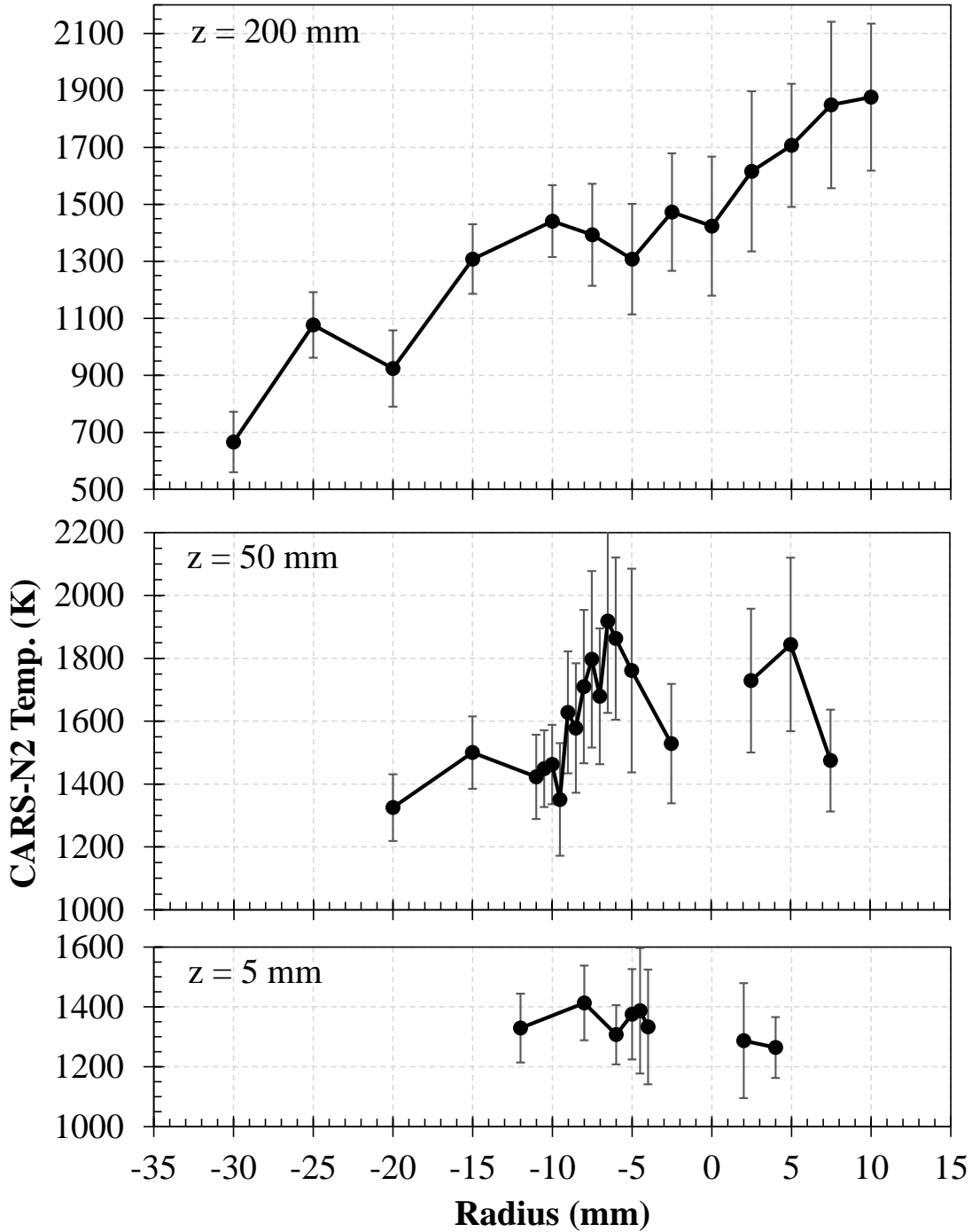
Fig. 45-Radial temperature profiles from the burning spray plume, produced by 0.1 g/s of ethane and 0.2 g/s of heptane.

3-Color High-Speed Pyrometry

High-speed color movies were recorded for a total of four flame conditions, with a representative snapshot of each shown in Figure 46. The conditions included flow rates (in g/s) of ethane at 0.1 and heptane at 0.2 (E1H2), 0.2 and 0.4 (E2H4), and baseline gas-only cases with ethane at 0.1 (E1) and 0.2 (E2) that provide comparative baselines. As Figure 46 shows, the observed flames were highly turbulent and

luminous due to soot emission in all cases except for the E2H0 flame. Due to the lack of any Planck emitters (soot particles), the E2H0 flame is a barely visible faint blue color and cannot be processed using the 3CHIP method. The images of the luminous flames display expected behavior, with the typical vortical structures of the E1H0 gas-jet flame, the highly folded structure of both turbulent spray flames (E1H2 and E2H4), and the noticeably higher turbulence for the spray flame with higher gas and liquid flow rates (E2H4 vs. E1H2).

Fig. 46-Sample high-speed color images of four flame conditions: (a) E1H0, (b) E1H2, (c) E2H0, and (d) E2H4.

Processed images and corresponding condensed-phase temperature maps are shown in Figure 47 for the E1H0, E1H2, and E2H4 flame cases. Although these are single snapshots, the images and temperature maps shown are representative of the overall behavior for each condition. As shown in Figure 47, the E1H0 flame exhibits minimal turbulence and also has the highest soot temperature of the three cases. The spatially averaged temperature for the E1H0 flame image (Figure 47d) is approximately 2700 K, which is significantly higher than the adiabatic flame temperature of a stoichiometric ethane/air flame (approximately 2220 K). A possible reason for this difference is that the oxidizer in this case is the exhaust products from the lean H_2/air pilot flame which is used to ignite and anchor the spray flame. As reported above, coherent anti-Stokes Raman scattering (CARS) spectroscopy measurements showed a temperature of approximately 1300 K for the hydrogen/air pilot flame [107]. Thus, the reactants for the spray flame include entrained gas with much higher enthalpy than ambient, which should increase the temperature of the spray flame. For the spray flames, relative to the gas-phase flame, Figure 47 shows that the level of turbulence is significantly higher, while the soot temperatures are significantly lower. While the spatially averaged temperature of the E1 flame is 2700 K, temperatures of the E1H2 and E2H4 flames are approximately 2130 K and 2240 K, respectively. This is an expected result, given that increased turbulence increases entrainment of ambient gas, thus creating a spray flame with a higher level of partial premixing. This, in turn, results in a leaner and therefore lower-temperature flame. In addition, evaporative cooling of droplets in the spray flame represents a heat sink that is not present for the gas-only flame. The difference in soot temperature between the two spray flame cases (E1H2 and E2H4) is not considered significant, given that the uncertainty in these measurements is approximately 150 K. These soot temperatures are somewhat higher than the gas-phase temperatures measured using CARS-N_2 thermometry that were reported from the corresponding CARS measurements. In the CARS study, peak gas-phase temperatures were approximately 1850 K at a height of 100 mm above the burner. The readers should consider that CARS-N_2 thermometry and 3CHIP are measuring two different temperatures. The former is measuring gas temperature while the latter is measuring the condensed-phase soot temperature, though the difference between them is not substantially larger than the sum of the measurement uncertainties (~150 K for 3CHIP,

~100 K for CARS) and the methods probe two different components of the same flame. Further measurements would be needed to finely resolve and reconcile the differences in the measured temperature from the two diagnostic techniques.
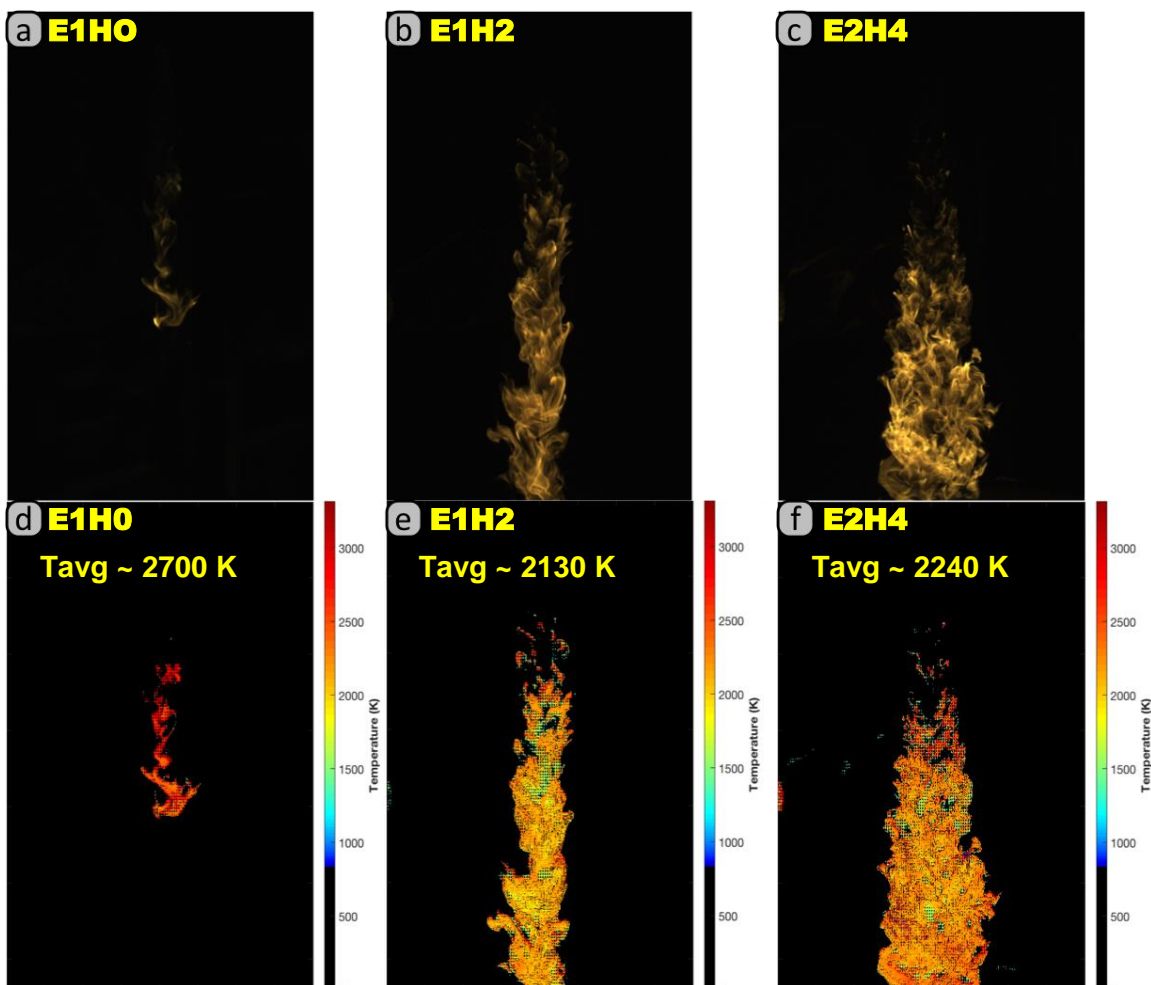
Fig. 47-3CHIP processed images for three flame conditions: (a,d) E1H0; (b,e) E1H2; (c,f) E2H4.

Intermediate-Scale

Experimental Platform

For this work, we designed a simple burner that creates flow conditions similar to a petroleum wellhead, but at much smaller scale. As shown in Figure 48, overall the burner consists of a long, straight stainless steel tube with inner diameter (ID) of 8.5 mm (0.335 inches) and outer diameter of 9.5 mm (0.375 inches). In terms of the open area for fluid flow in the pipe, this intermediate-scale burner represents a 103-fold increase relative to the bench-scale burner. The gas enters at the bottom, while the liquid enters through a tee slightly above the gas entry point. From the point of liquid entry, the length of the burner tube is 116 cm (45.7 inches). There are two ports designed for measurement of static pressure, at heights of 19 cm (7.5 inches) and 112 cm (44 inches) above the point of liquid entry. Each of these pressure ports consists of a row of four small holes (1-mm diameter), spaced equally around the circumference of the burner tube, contained within a bored-through tee fitting.

In designing the burner, the main focus was the mixing tee, shown in detail in Figure 48b. Liquid enters through the side-arm of the tee fitting and is forced through a series of small holes into the burner tube that is already carrying the gas flow. The holes are 1-mm diameter and are arranged in four rows, each having eight holes that are equally spaced around the circumference of the tube. With this design, the total entry area is ~25 mm^2 for the liquid, which is slightly less than half of the cross-sectional area of the main burner tube (~57 mm^2). Visual observation of the resulting spray flame suggests that this configuration successfully prevents acoustic effects and large-scale oscillations in the two-phase flow. The length of the tube available for the combined two-phase gas-oil flow, which is equivalent to ~136× the inner diameter of the tube, is considered sufficient for the gas and oil to mix and develop into an annular two-phase flow.
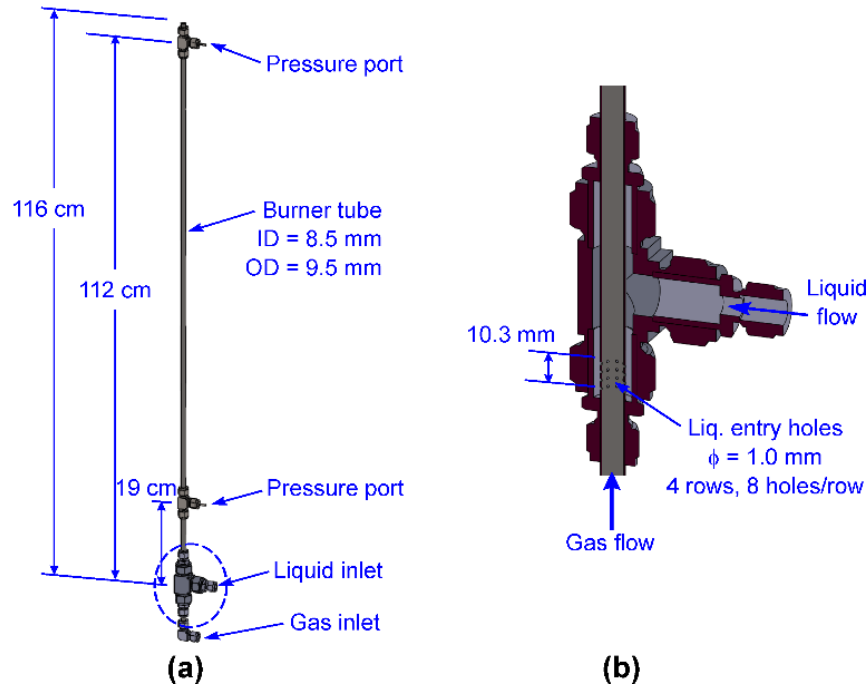
Fig. 48-Schematic of (a) overall burner and (b) gas-liquid mixing tee.

Experiments at this scale require large gas and liquid reservoirs and high-capacity flow-control equipment compared to what is typically used in a laboratory setting. A schematic of the plumbing setup is shown in Figure 49. Gas reservoirs consist of the following: six compressed methane (CH$_4$) cylinders connected to a manifold and regulator; four compressed ethane (C$_2$H$_6$) cylinders connected to a second manifold and regulator; and a 120-gallon propane tank with a regulator. Each of the regulated gas lines is equipped with a manual ball valve, a check valve, and a computer-interfaced mass flow controller (MFC). The MFCs, all supplied by Alicat Scientific, were chosen to provide relevant flow ranges for each of the gases: 0 – 3000 slpm for methane; 0 – 250 slpm for ethane; and 0 – 1000 slpm for propane. The three gases are mixed together downstream of the MFCs and sent to the burner. While the majority of the propane flow goes through the MFC to the burner, a portion is split off and regulated to provide fuel for a small pilot flame (described later). Crude oil is pumped out of a 5-gallon bucket by a spur gear pump (Viking Pump, SG-40514) with flow rate and pressure capacities of 21.2 lpm and 34 bar (500 psi), respectively.
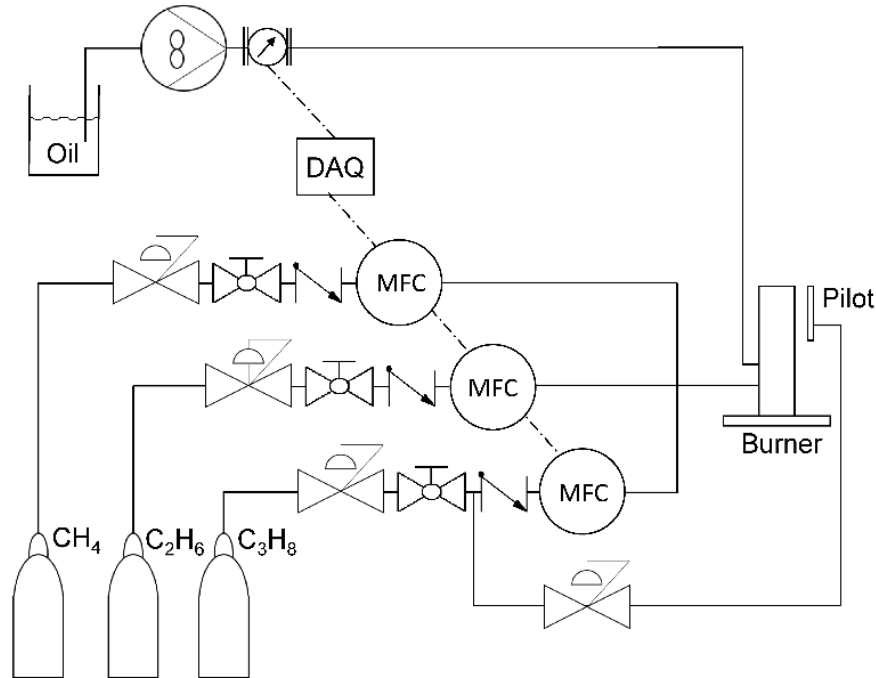
Fig. 49-Plumbing schematic for burn efficiency experiments.

A custom LabVIEW program and National Instruments CompactDAQ hardware are used for experimental control and data acquisition (DAQ). Desired gas flow rates are communicated directly to the MFC units and actual flow rates are communicated back to the DAQ computer as the MFC adjusts to the setpoint. Desired liquid flow rate, converted to a voltage, is communicated to a variable-speed drive system, which controls the motor that is connected to the gear pump. A positive-displacement flow meter (FLOMEC, OM015) measures and reports liquid flow rate, though there is no closed-loop control system.

Experiments were conducted at the NRL Chesapeake Bay Detachment (CBD) facility, which is designed for large-scale fire testing. The burner was initially set up outdoors, but it became quickly obvious that consistently strong and gusty winds would make it impossible to maintain a stable flame. Therefore, the burner was moved into a test chamber that mimics a shipboard machinery space, known as an "IMO box". A standard IMO box has dimensions of 10 m × 10 m × 5 m, but the one at NRL-CBD is actually 9.1 m × 9.1 m × 4.3 m (30 ft × 30 ft × 14 ft) with a total volume of 360 m^3. The chamber has three doors, one on the east side near the northeast corner and two on the south side near the corners. Only the two doors on the south side remained open during these experiments for personnel to enter and exit and to enable safe direct observation of the flame from outside. In addition, several of the panels that normally form the chamber roof were removed to create a large opening (3 m × 3 m), which allowed the flame to establish its own natural height without interference from the roof and allowed small combustion residuals (e.g., small particulates) to disperse into the outside air. Operation of the burner in the IMO box resulted in a stable flame, and thus repeatable burn efficiency measurements even under highly variable outdoor weather conditions.

Diagnostics Methods

Burn Efficiency Measurement
The intermediate scale burner affords the ability to take burn efficiency measurements using crude oil. A novel approach to gathering oil fallout from the flame was devised, and this is detailed in the attached manuscript by Fisher *et al.* [108]. This approach allows a reasonable estimate of burn efficiency of the flame. Further burn efficiency measurements will be performed, after which more conclusions can be drawn regarding the burner scales, different flow conditions, and in-field wellhead fires.

Experimental Results

There are some significant findings that we observed from our intermediate-scale work that should be mentioned. During preliminary pump system shakedown with water and air, we observed indications that the flow behavior was consistent with the laboratory experiment. In particular, we observed that the bulk of the liquid flow was in an annular region surrounding the core gas flow. We also observed the formation of expansion shocks in the plume with only air flow.

Figure 50 shows a photograph of a typical burning, two-phase spray plume of simulated well gas and crude oil. It is lifted above the nozzle 20-30 cm and extends just beyond the roof of the building, but there is not enough wind to impact the flame anchoring and general plume geometry. The liquid flow is not fully entrained in the gas flow. As with our laboratory tests, the combined diameter and velocity are not great enough to fully entrain the liquid to form a misty flow. This behavior is similar to those we would expect at flow rates much less than the WCD of any new well, where there is either an obstruction in the pipe, low reservoir pressure, or a low gas-oil ratio. Second, we see that there are many droplets of oil escaping the plume and falling toward the ground, leaving trails of smoke in their wakes. These are the heaviest, largest droplets that are too large to be entrained by the momentum of the plume and surrounding gas and instead fall down onto the ground. These are droplets that would dominate and decrease the burn efficiency of any intentionally ignited wellhead. This observation shows that a dominant mechanism of inefficient burning is not whether or not the asphaltene is burned, but whether or not the oil has been atomized to sufficiently small diameters that will be dominated by the OPA jet momentum and will burn. In this case, we see that the unentrained portion of the liquid flow produces the largest droplet diameters.

Fig. 50-Photograph of the burning spray plume operating with 3.0 g/s of 80:5:15% of CH_4, C_2H_6, and C_3H_8 and a blend of crude oils flowing at 16 g/s.

If we relate this flow to the entrainment correlations from Kataoka *et al.* [30] vs. Berna *et al.* [35], we obtain very different results. The Kataoka *et al.* [30] correlation predicts an entrainment fraction of 1.8%, if we account for the length of the tube (see Equations 3 and 5). In contrast, the Berna *et al.* [35] correlation predicts entrainment of 100%. This suggests that entrainment correlation development has some significant gaps.

Burn Efficiency

As of the writing of this report, a paper has been submitted to the journal Fuel that details the method we have developed to measure burn efficiency. The draft manuscript can be found in *Appendix B*.

3-Color High-Speed Pyrometry

We also gathered 3CHIP data for two flame conditions, both at 3 g/s of gas and one each at 16 and 32 g/s of Endicott crude oil. The image was acquired at 10,000fps using a Phantom high speed camera with an exposure of 25 us. A Nikon 105mm Macro lens was used to image the frame. The image on the left depicts the temperature map of the two phase spray combustion and was obtained employing an inverse wavelength emissivity dependence. As can be seen the core of the spray is much cooler (~1200K) compared to the periphery (~2000K). A caveat in these measurements is that the flame is assumed to be optically dense. More work is currently underway in temporally averaging the spray field so as to develop an axisymmetric field which could be deconvolved through Abel inversion techniques to obtain in plane soot emission.
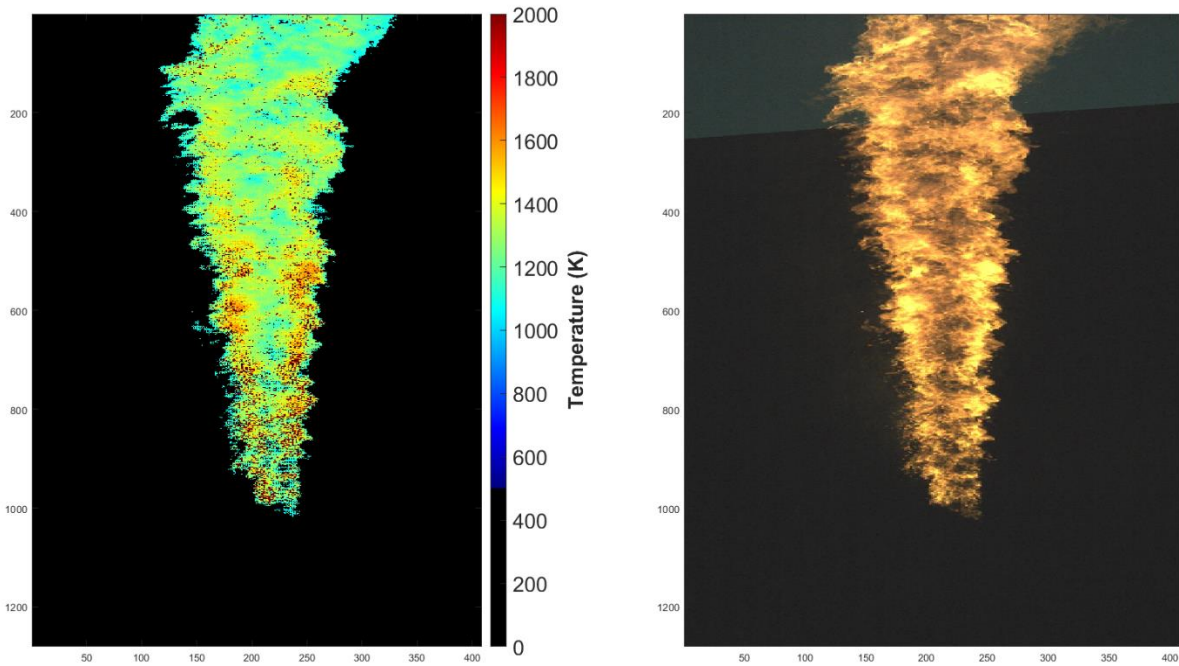
Fig. 51-3g/s of gas (CH4:C2H6:C3H8 = 80:5:15) and 32g/s of Endicott Crude oil.

The use and validation of this technique with the intermediate-scale experiment and the validation efforts currently underway, as described in the section *CARS and 3-Color Pyrometry Comparisons*, show that the 3CHIP method can be applied to measure plume temperature in the field for any sooting flame. Not only can we apply this method to the platforms described here, but also pool fires and other sooting flames.

COMPUTATIONAL AND EXPERIMENTAL COMPARISON

We have hitherto separated the computational and experimental results, since they each merit discussion and analysis. This section is devoted to comparison of each to one another.

Bench-Scale Gas-Phase Temperature Measurement and Prediction Comparison

The three mass flow rates of propane used in this study generate a compressible subsonic jet ($\dot{m}$ = 0.1 g/s), a weakly choked jet with maximum Mach number approximately equal to one ($\dot{m}$ = 0.2 g/s), and an under-expanded jet that has a well-developed shock-wave structure in its inviscid core ($\dot{m}$ = 0.3 g/s), as shown in Table 4. Despite the differences in the core jet dynamics, the turbulent flame brush is quite similar for all three cases, as illustrated by the simulated mean temperature fields shown in Figure 9. In all three cases, the jet velocity is sufficiently large to lift the flame off of the burner. The lift-off heights computed for these cases are approximately 30, 40 mm, and 55 mm, respectively, which correspond well to the experimental observations listed in Table 4.

The CARS thermometry measurements are shown along with the computed radial temperature profiles in Figure 52. Each column corresponds to a fixed $\dot{m}$ = 0.1, 0.2, and 0.3 g/s (from left to right). In all cases, the bottom and top frames correspond to measurements taken at heights of z = 25 mm and z = 80 mm above the burner, respectively. The data in the middle frames correspond to a position just above the anchoring point of the turbulent flame brush, which varies with the flow rate. The solid lines in the figures represent simulations performed using the baseline pilot flame inflow conditions discussed in the description of the temperature measurements in *CARS – Gas Phase*. The dotted lines correspond to the φ = 0.36, T = 1311 K and φ = 0.435, T = 1482 K inflow conditions and give a measure for the uncertainty of the pilot flame used to stabilize the laboratory flames.

There is generally good agreement between the CARS measurements and the numerical simulations for z = 25 mm profiles for the three cases, which gives some indication of the suitability of the realizable k-ε model for these flows. This particular location is below the propane flame lift-off height, so these temperature profiles correspond to the mixing of the cold propane jet (prior to ignition) and to the combustion products of the premixed H_2-air pilot flame. At $\dot{m}$ = 0.1 g/s, the temperature increases radially from 800 K to 1400 K. The propane jet at the center of the burner is cooler than the surrounding hot product gases from the premixed pilot flame. At z = 45 mm, near the flame lift-off height, there is also reasonable agreement between the measurements and simulation. Temperature increases radially from the jet center at 1000 K to the flame front near r = 6 mm at 1700 K. Then, the profile decreases to the temperature of the pilot flame, approximately 1400 K. The data taken farther downstream at *z* = 80 mm show a significant increase in temperature that was not predicted by the simulation, both at the center of burner and at the position of the flame front. We note, however, that the maximum temperature in the simulation reaches approximately 2250 K, which agrees with the experimental measurements. The temperature rise to this level begins several centimeters downstream of the 80 mm measurement location.
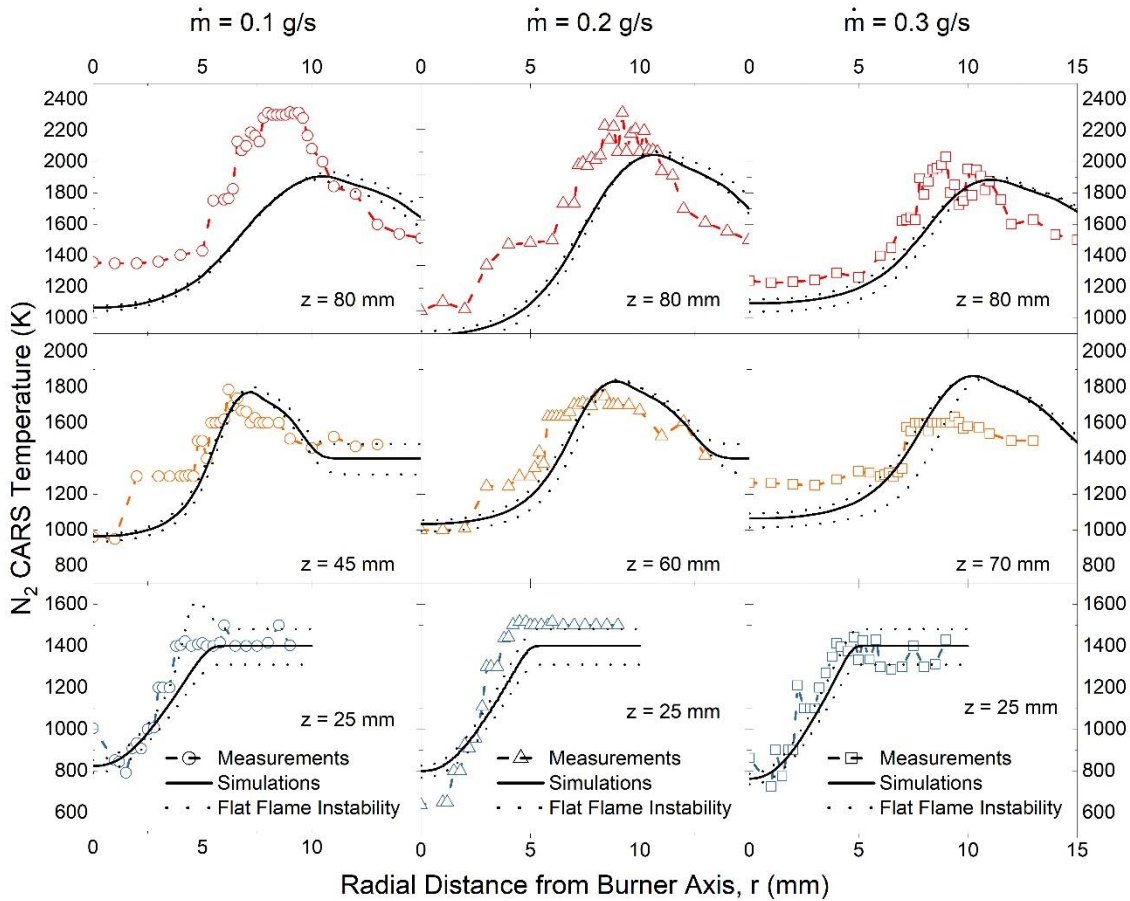
Fig. 52-Temperature profiles of propane gas jet from numerical simulations (solid lines) and N_2 CARS thermometry (dashed lines) for a propane flow rate of 0.1 g/s, 0.2 g/s and 0.3 g/s.

For the weakly choked case ($\dot{m}$ = 0.2 g/s), illustrated in the middle column of plots in Figure 52 the temperature of the propane jet is experimentally measured to be near 650 K, which is cooler than the corresponding temperature of $\dot{m}_{Propane}$ = 0.1 g/s due to compressibility effects. The pilot flame temperature was measured to be approximately 1500 K, which is 100 K higher than that measured for the $\dot{m}$ = 0.1 g/s. For this particular case, it is likely that the laboratory airflow rate was suppressed, which resulted in an increase in the equivalence ratio of the H_2-air mixture. This would account for the systematically high temperature measurements at large radial distances. The upper dotted line in each of the frames in the middle column of Figure 52 (φ = 0.435, T = 1482 K pilot flame inflow conditions) correspond to the experimental conditions better than the baseline (solid) simulation data. At all three measurement locations, the agreement between the simulation data and experimental measurements is reasonable.

The right column of plots in Figure 52 illustrates the underexpanded jet case, $\dot{m}$ = 0.3 g/s. Upstream of the flame (z = 25 mm), we see good agreement between measurement and simulation. The temperature increases radially from the jet center at 800 K to the premixed pilot flame temperature of approximately 1350 K. In this case, the measured pilot flame temperature lies within the uncertainty in the experimental measurements (discussed below), and the potential deviation of the true pilot flame conditions cannot be conclusively ascertained. Regardless, the simulation predictions at the z=80 mm location are consistent with the experimental measurements with deviations of ±100 K. The comparisons are worse at the z = 70

mm location. The peak simulation temperatures are 300 K larger than the measured temperatures, and the simulated jet core temperature is 200 K lower the measurements. This is expected, however, since the location of the flame anchoring position is highly dependent on the pilot flame conditions. The maximum experimental temperatures of approximately 1600 K suggest that z = 70 mm location was quite close to this location. The simulated flames anchored several mm upstream of this location, which explains the marked difference in maximum flame temperature.

Although the error in the CARS measurements cannot be easily calculated, the distribution in temperatures of the 300 to 500 shots that were taken per data point in the plots of Figure 52 can be measured. The signal-to-noise ratio in the CARS spectra for some of the conditions in Table 4 was sufficient to perform a shot-to-shot analysis of the distribution in temperature. The most favorable data for this analysis corresponded to cooler temperatures because of their more highly populated ground vibrational band of N_2 resulting in better signal-to-noise ratios. Figure 53 illustrates the results for a normal distribution fitted to the histogram of the shot-to-shot analysis at some of the locations in the temperature profiles at z = 25 mm. The empty box symbols represents the center of the normal distribution while the vertical error bars represent the standard deviation of the distribution. Results with flow rates of 0.1 and 0.3 g/s are shown. The center locations follow the same trend as the averaged profiles. The spread in the distribution appears to decrease radially from approximately ±100 K near the jet center to ±50 K outside of the jet in the pilot flame combustion products. This illustrates more consistent results for the fitting routine and less uncertainty in the pilot flame region.
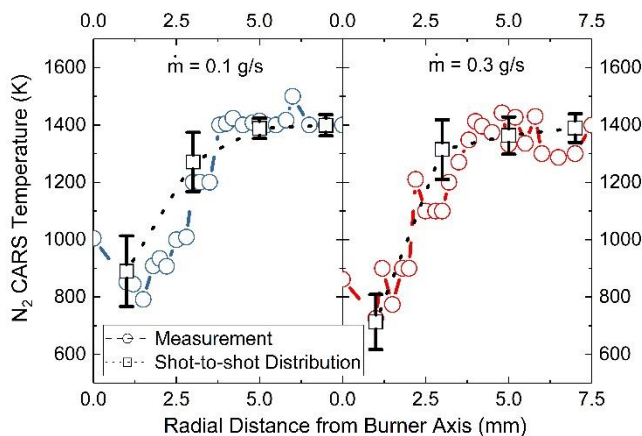
Fig. 53-Shot-to-shot analysis of the distribution in temperature at various locations in the radial profile at z = 25 mm for two flow rates.

SUMMARY AND CONCLUSIONS

A computational model and parallel experimental and analytical efforts have been underway to predict and examine the fundamental and practical spray combustion behavior for scenarios relevant to oil/gas wellhead fires. An analysis of the basic physical principles that control the structure and dynamics of two-phase turbulent gas-oil jet flames has been presented. A minimal computational model was constructed that encompasses the most critical of these processes to enable high-fidelity simulation of an in-situ well head burning event. Such a model could be used to evaluate the conclusions drawn from lower-fidelity engineering models for predicting the oil combustion efficiency for a set of reservoir conditions. We have provided a basic validation of the underlying gas-phase turbulent flame structure and identified a significant sensitivity of the two-phase flow model to the details of the oil droplet atomization process. A semi-

empirical model was developed to estimate proper droplet injection conditions, and this model is currently being validated against bench-scale flame diagnostics. The models are qualitatively compared to an intermediate-scale blowout, as limited by current diagnostics on the larger experiment. The intermediate-scale experiment allows the complexity of using real crude oil and natural gas and creates an opportunity to use a novel method for in-situ burn efficiency measurement. A path forward for incorporating the physical properties of more representative crude oil surrogates into the modeling framework has been identified, and this will form the basis of future model validation efforts. Analysis of relevant literature has been performed in order to understand current knowledge gaps with wellbore flow and oil blowout spray behavior.

From this work, we have made a number of significant accomplishment and findings that further the state of the art of both computational capability and of fundamental understanding of burning wellhead plumes. One of the most significant accomplishments from this program was the development of computational model that captured both gas phase and liquid phase behavior. Though not yet comprehensive in its scope or validation, it couples the liquid and gas phase mechanics, thermodynamics, and chemistry in a way not previously attempted for this problem until now. Previous models have isolated the gas mechanics from that of the spray, which uncoupled these behaviors that couple their momentum, energy, and mass transport and reaction. As this model matures, it may be adapted to wellhead conditions to examine the effects of WCD and to perform parametric studies that will provide insight into scenarios with much more severe consequences [32,109,110].

Another significant accomplishment from this work has been the development of an experimental architecture and method to measure burn efficiency from flows that emulate wellhead blow out [108]. The development and validation of the experimental measurements have revealed that it is possible, repeatable, and relevant to such flows. From this experiment, we were also able to observe the mechanisms that reduce burn efficiency. In particular, the fallout of large droplets that were formed at the periphery of the plume from the annularly distributed spray, which appeared to provide most of the liquid that fell to the ground. Based on the our laboratory observations, we hypothesized that these droplets were formed from the un-entrained film of the wellbore flow.

Corresponding laboratory spray measurement and visualization revealed the magnitude of the discontinuity of the liquid distribution across the plume. In particular, we discovered that depending on the gas and liquid flow rates, a large portion of the liquid remained in the un-entrained film of the pipe. Upon exiting the pipe (wellbore), a film formed that rapidly formed ligaments and then droplets. The droplets formed from the annular film were much larger than those at the center or core of the flow. This behavior corresponded with our observations of the spray plume made during the burn efficiency measurements of the much larger droplets at the plume periphery [32,33,107,108,111].

Finally, we discovered from the analysis of wide range of flow rates that the WCD is not be the worst-case spill scenario for a wellhead. In the case of the aforementioned Liberty project, which had a very high reservoir pressure and flow rate, it is highly likely that the resulting flow will atomize and burn fairly well. In contrast, as the flow rate decreases, the entrainment fraction decreases and the film thickness increases. The corresponding experimental observations reveal that in such cases, the increasing film thickness will produce increasingly large droplet diameters at the periphery of the plume, which will be the most likely to fall, unburned, back to the ground [44].

ACKNOWLEDGEMENT

PERSONNEL

The Navy Technology Center for Safety and Survivability of the Naval Research Laboratory has an established history of successfully supporting the combustion and fire testing of the Navy's facilities and operations.

Dr. Steven Tuttle is a Mechanical Engineer and Section Head in the Combustion and Reacting Transport Section of the Navy Technology Center for Safety and Survivability (NTCSS) at the U.S. Naval Research Laboratory (NRL). Dr. Tuttle worked in the gas turbine industry for seven years while managing and conducting his doctoral research at the University of Connecticut. As an engineer, he developed and validated heat transfer, thermoacoustic, and spray combustion stability models for main burners, afterburners, and nozzles in the engine technology development and demonstration organizations. At the same time, he directed and managed funding to the University of Connecticut that supported his research and that of others. As a student, he designed and built an afterburner combustion experiment and the associated electronic fuel control and safety systems. For his postdoctoral studies, he was the principle investigator for velocity measurements of a reacting scramjet cavity and shear layer at the U.S. Air Force Research Laboratory. He joined the staff at NRL in 2011, where he is the principle investigator of a Department of Interior-sponsored program examining combustion behavior of emulsified crude oil slicks and sprays. He also collaborates with other NRL investigators in projects ranging from novel fuels to fire characterization and instrumentation.

Dr. David A. Kessler is a mechanical engineer in the Laboratories for Computational Physics and Fluid Dynamics at the Naval Research Laboratory (NRL), where he is involved in research in multiphase reacting flows, high-speed propulsion systems, detonation dynamics and shock-flame interactions, data-driven modeling of reaction chemistry, deflagration-to-detonation transitions, and shock-droplet interactions. David has been a member of the research staff since 2008, and prior to that was a National Academy of Science Postdoctoral Research Associate at NRL from 2006 to 2008. Before coming to NRL, David was a student at the University of Illinois at Urbana-Champaign in the Department of Theoretical and Applied Mechanics, where he did his PhD research on the physics of combustion in microscale devices. Details of his work have appeared in Combustion and Flame, Combustion Theory and Modeling, Journal of Fluid Mechanics, the Philosophical Transactions of the Royal Society of London, and the Proceedings of the Combustion Institute.

Dr. Brian Fisher's research interests include engines, rocket propulsion, combustion, alternative fuels, and the application of laser-based and optical diagnostics in thermal sciences. After completing his Ph.D. at the University of Florida in 2004, he held a National Research Council post-doctoral appointment at the Naval Research Laboratory, followed by a post-doctoral appointment in the Combustion Research Facility at Sandia National Laboratory. Dr. Fisher was an associate professor in the Department of Mechanical Engineering at The University of Alabama for three years (2011-2014) before joining the Combustion & Reacting Transport Section (Code 6185) at the Naval Research Laboratory as a full-time scientist/engineer in 2015. His research focuses on characterization of multiphase reacting flows, namely spray and solid-fuel combustion, with particular emphasis on understanding fundamental chemical and physical behaviors relevant to practical combustion systems. Dr. Fisher's current efforts include basic research programs on metal particle and composite solid fuel combustion mechanisms, and an applied research program on petroleum wellhead fires.

Mr. Christopher J. Pfützner is a Mechanical Engineer in the Combustion and Reacting Transport Section in the Navy Technology Center for Safety and Survivability (NTCSS) at the U.S. Naval Research Laboratory. Mr. Pfützner has worked in a technical capacity with an oil and gas blending company in Houston, Texas, in addition to working in the refrigeration and automotive industries since 2009. At Colorado School of Mines, he studied Mechanical Engineering, contributed to research involving heat

transfer and oxidation in concentrated solar cells, and managed the school's battery-electric vehicle efforts throughout its lifecycle. He joined NRL in 2017 and serves in various design and test engineering roles in support of internal and external programs.

Dr. Aaron Skiba is an ASEE Postdoctoral Fellow in the Combustion and Reacting Transport division at the US Naval Research Laboratory (NRL). His research primarily focuses on employing high-speed imaging techniques to measure the primary and secondary atomization behavior of two-phase flows issuing from an open-pipe atomizer. Aaron is also assisting with the application of advanced laser-based diagnostics, such as Coherent Anti-Stokes Raman Spectroscopy (CARS), to such flows as a means to accurately measure their gas phase temperatures. Prior to his employment at NRL, Aaron was a Research Associate in the Department of Engineering at the University of Cambridge, UK. While there, his research primarily focused on employing laser-based imaging techniques to elucidate the effects turbulence, fuel-type, and dilution level have on the production and oxidization of soot within a model aero-engine. Aaron received his Bachelors, Masters, and Ph.D. degrees from the department of Aerospace Engineering at the University of Michigan. During his Ph.D., Aaron studied the effects extreme turbulence levels have on the structure and dynamics of premixed flames. A significant portion of his dissertation research was carried out in collaboration with Dr. Campbell D. Carter at the Air Force Research Laboratory (AFRL). Aaron assisted Dr. Carter with the application of an array of state-of-the-art, laser-based diagnostics to highly turbulent premixed flames. The most notable of which involved the simultaneous acquisition of stereo-PIV data with PLIF images of $CH2O$ and OH at a rate of 20 kHz. Overall, Aaron's interests lie in developing and utilizing advanced laser-based and imaging diagnostics to understand the fundamental physics of flow-chemistry interactions. Ultimately, this understanding will facilitate the development of accurate models for predicting the dynamics of turbulent reacting flows as well as the concentration of species they produce.

Dr. Rohit Jacob is a Mechanical Engineer and works as a National Research Council post-doctoral associate in the Navy Technology Center for Safety and Survivability (NTCSS) section of the U.S. Naval Research Laboratory (NRL). Dr. Jacob obtained his Ph.D. in Mechanical Engineering and Chemical and BioMolecular Engineering at the University of Maryland, where he worked on developing high speed optical diagnostics for nanoscale energetic materials, which are a relatively new class of reactive materials that have a high energy density and fast reaction timescales. His research interests include rocket propulsion, combustion, reactive materials and optical diagnostics. Dr. Jacob's current research focuses on developing and characterizing highly energetic solid fuels for air breathing/ hybrid propulsion, particularly with metallic additives. Concurrently, he is also working on characterizing turbulent, reactive multiphase flows through optical diagnostics, which aids in the fundamental understanding of oil wellhead fires.

REFERENCES

[1]   Amer, M., "Well Ignition and Capping Experience," *Well Ignition as a Blowout Response: A Peer Review Workshop for Dialogue*. Ocean Energy Safety Institute, Houston, TX, 2017.
[2]   Garner, J., "Well Capping While Burning," *Well Ignition as a Blowout Response: A Peer Review Workshop for Dialogue*. Ocean Energy Safety Institute, Houston, TX, 2017.
[3]   Zdeb, C., "Lodgepole sour gas well blowout finally capped," *Edmonton Journal*. Edmonton, Alberta, 1982.
[4]   "Emergency Preparedness and Response Requirements for the Petroleum Industry," *ERCB DIRECTIVE*. Vol. 071, Alberta, Canada, 2017.
[5]   Ross, S. L., "Decision-Making Aids for Igniting or Extinguishing Well Blowouts to Minimize Environmental Impacts," *Environmental Studies Revolving Funds,* Canada Oil and Gas Lands Administration. Waterloo, Ontario.
[6]   EPA. "United States Gulf Environmental Technical Assistance," U.S. Environmental Protection Agency. 1992.

[7]   HSE. "Kuwait Scientific Mission - Mission Overview," The Steel Construction Institute, OTH 94 450. Vol. 1, Berkshire, July 1992.

[8]   HSE. "Kuwait Scientific Mission - Technical Report," The Steel Construction Institute. Vol. 2, Berkshire, July 1992.

[9]   Cahill, T. A., Wilkinson, K., and Schnell, R., "Composition analyses of size-resolved aerosol samples taken from aircraft downwind of Kuwait, spring 1991," *Journal of Geophysical Research: Atmospheres* Vol. 97, No. D13, 1992, pp. 14513-14520.
doi: 10.1029/92JD01373

[10]   Cofer, W. R., Stevens, R. K., Winstead, E. L., Pinto, J. P., Sebacher, D. I., Abdulraheem, M. Y., Al-Sahafi, M., Mazurek, M. A., Rasmussen, R. A., Cahoon, D. R., and Levine, J. S., "Kuwaiti oil fires: Compositions of source smoke," *Journal of Geophysical Research: Atmospheres* Vol. 97, No. D13, 1992, pp. 14521-14525.
doi: 10.1029/92JD00967

[11]   Evans, D. D., Walton, W. D., Baum, H. R., Mulholland, G. W., Lawson, J. R., Koseki, H., and Ghoniem, A. F., "Smoke Emission From Burning Crude Oil," National Institute of Standards and Testing, NIST SP 995. Vol. 2, 12-14 June 1991.

[12]   Hobbs, P. V. and Radke, L. F., "Airborne Studies of the Smoke from the Kuwait Oil Fires," *Science* Vol. 256, No. 5059, 1992, pp. 987-992.
doi: 10.1126/science.256.5059.987

[13]   Laursen, K. K., Ferek, R. J., Hobbs, P. V., and Rasmussen, R. A., "Emission factors for particles, elemental carbon, and trace gases from the Kuwait oil fires," *Journal of Geophysical Research: Atmospheres* Vol. 97, No. D13, 1992, pp. 14491-14497.
doi: 10.1029/92JD01370

[14]   Ferek, R. J., Hobbs, P. V., Herring, J. A., Laursen, K. K., Weiss, R. E., and Rasmussen, R. A., "Chemical composition of emissions from the Kuwait oil fires," *Journal of Geophysical Research: Atmospheres* Vol. 97, No. D13, 1992, pp. 14483-14489.
doi: 10.1029/92JD01247

[15]   Henry, C. B. and Overton, E. B., "Chemical Composition and Source Fingerprinting of Depositional Oil from the Kuwaiti Oil Fires," *International Oil Spill Conference Proceedings*, American Petroleum Institute, 1993.

[16]   Kruge, M. A., Gallego, J. L. R., Lara-Gonzalo, A., and Esquinas, N., Wang, Z. (ed.) *Oil Spill Environmental Forensics Case Studies*, Chapter 7 - Environmental Forensics Study of Crude Oil and Petroleum Product Spills in Coastal and Oilfield Settings: Combined Insights From Conventional GC–MS, Thermodesorption–GC–MS, and Pyrolysis–GC–MS, Butterworth-Heinemann, 2018, pp. 131-155.

[17]   Evans, D. D., Madrzykowski, D., and Haynes, G. A., "Flame Heights and Heat Release Rates of 1991 Kuwait Oil Field Fires," *4th International Symposium of International Association for Fire Safety Science*, International Association for Fire Safety Science, Boston, Massachussets, 1994.

[18]   Herring, J. A. and Hobbs, P. V., "Radiatively driven dynamics of the plume from 1991 Kuwait oil fires," *Journal of Geophysical Research: Atmospheres* Vol. 99, No. D9, 1994, pp. 18809-18826.
doi: 10.1029/94JD01753

[19]   Wade, R., Sivathanu, Y. R., and Gore, J. P., "A Study of Two Phase High Liquid Loading Jet Fires," U.S. Department of Commerce, National Institute of Standards and Technology, NIS-GCR-95-678. Gainseville, MD, October 1995.

[20] Dutta, P., Gore, J. P., Sivathanu, Y. R., and Sojka, P. E., "Global properties of high liquid loading turbulent crude oil + methane/air spray flames," *Combustion and Flame* Vol. 97, No. 3–4, 1994, pp. 251-260.
doi: 10.1016/0010-2180(94)90019-1

[21] Dutta, P., Sivathanu, Y. R., and Gore, J. P., "An Investigation of Oil and Gas Well Fires and Flares," National Institute of Standards and Technology, NIST-GCR-94-653. West Lafayette, Indiana, June 1994.

[22] Pfenning, D. B., "Final report for blowout fire simulation tests," National Bureau of Standards, NBS-GCR-85-484. January.

[23] Flak, L. H., Kelly, M. J., and Tuppen, J., "Case history of Timbalier blowout shows necessity of capping while burning." Endeavor Business Media, LLC, 1995.
https://www.offshore-mag.com/business-briefs/equipment-engineering/article/16762376/well-control-technology-case-history-of-timbalier-blowout-shows-necessity-of-capping-while-burning

[24] McCaffrey, B. J. and Evans, D. D., "Very large methane jet diffusion flames," *Symposium (International) on Combustion* Vol. 21, No. 1, 1988, pp. 25-31.
doi: 10.1016/S0082-0784(88)80228-5

[25] Hasan, A. R. and Kwon, J., "Literature Review for Understanding of Well-Ignition as a Blowout Response: A White Paper," Ocean Energy Safety Institute. College Station, Texas, 10 January 2018.

[26] Siddhamshetty, P., Ahammad, M., Hasan, R., and Kwon, J., "Understanding wellhead ignition as a blowout response," *Fuel* Vol. 243, 2019, pp. 622-629.
doi: https://doi.org/10.1016/j.fuel.2019.01.142

[27] Hilcorp. "Liberty Development Project Development and Production Plan (Revised)," Hilcorp Alaska, LLC. Vol. 2015.

[28] Fitzgerald, S. and Garner, J. B., "Hilcorp Liberty Project Burn Efficiency Evaluation: Final Report," Boots & Coots: A Halliburton Service, (Proprietary). 29 December 2014.

[29] Hilcorp. "Liberty Overview," *Well Ignition as a Blowout Response: A Peer Review Workshop for Dialogue*. Ocean Energy Safety Institute, Houston, TX, 2017.

[30] Kataoka, I., Ishii, M., and Nakayama, A., "Entrainment and desposition rates of droplets in annular two-phase flow," *International Journal of Heat and Mass Transfer* Vol. 43, No. 9, 2000, pp. 1573-1589.
doi: https://doi.org/10.1016/S0017-9310(99)00236-7

[31] Berna, C., Escrivá, A., Muñoz-Cobo, J. L., and Herranz, L. E., "Review of droplet entrainment in annular flow: Interfacial waves and onset of entrainment," *Progress in Nuclear Energy* Vol. 74, 2014, pp. 14-43.
doi: https://doi.org/10.1016/j.pnucene.2014.01.018

[32] Fisher, B. T., Kessler, D. A., Tuttle, S. G., and Tuesta, A. D., "Experimental Measurements and Numerical Simulations of Droplet Behavior in a Heptane/Ethane Spray Flame," *41st AMOP Technical Seminar on Environmental Contamination and Response*, Environment and Climate Change Canada, Ottawa, Ontario, Canada, 2018.

[33] Fisher, B. T., Tuttle, S. G., Jacob, R. J., Pfützner, C. J., Tuesta, A. D., and Kessler, D. A., "High-Speed Imaging of Atomization Behavior and Temperature Field in Spray Flames that Simulate Oil Wellhead Fires," *42nd AMOP Technical Seminar on Environmental Contamination and Response*, Environment and Climate Change Canada, June 4-6, 2019,

[34]   Kataoka, I., Ishii, M., and Mishima, K., "Generation and Size Distribution of Droplet in Annular Two-Phase Flow," *Journal of Fluids Engineering* Vol. 105, No. 2, 1983, pp. 230-238.
         doi: 10.1115/1.3240969

[35]   Berna, C., Escrivá, A., Muñoz-Cobo, J. L., and Herranz, L. E., "Review of droplet entrainment in annular flow: Characterization of the entrained droplets," *Progress in Nuclear Energy* Vol. 79, 2015, pp. 64-86.
         doi: 10.1016/j.pnucene.2014.11.011

[36]   Berna, C., Escrivá, A., Muñoz-Cobo, J. L., and Herranz, L. E., Vorobieff, P., Brebbia, C. A., and Munoz-Cobo, J. L. (eds.), *Computational Methods in Multiphase Flow VIII*, Development Of New Correlations For Annular Flow, WIT Press, 2015, pp. 451-462.

[37]   Shearer, A. J., Tamura, H., and Faeth, G. M., "Evaluation of a Locally Homogeneous Flow Model of Spray Evaporation," *Journal of Energy* Vol. 3, No. 5, 1979, pp. 271-278.
         doi: 10.2514/3.62437

[38]   Singh, G., Esmaeilpour, M., and Ratner, A., "Effect of polymeric additives on ignition, combustion and flame characteristics and soot deposits of crude oil droplets," *Applied Energy* Vol. In Review, Submitted 2019.

[39]   Singh, G., Esmaeilpour, M., and Ratner, A., "Effect of carbon-based nanoparticles on the ignition, combustion and flame characteristics of crude oil droplets," *Energy* Vol. In Review, Submitted 2019.

[40]   Rastegar, R., "Liberty WCD Scenario," *Well Ignition as a Blowout Response: A Peer Review Workshop for Dialogue*. Ocean Energy Safety Institute, Houston, TX, 2017.

[41]   ECCC. "Oil Properties." Environment and Climate Change Canada, 2001.
         http://www.etc-cte.ec.gc.ca/databases/OilProperties/oil_prop_e.html

[42]   AOGCC. "Reservoir Properties." Alaska Oil and Gas Conservation Commission, 2018.
         http://aogweb.state.ak.us/poolstatistics/annual/current/OIL/Endicott,Endicott_Oil/Reservoir_Properties.html

[43]   Lemmon, E. W., McLinden, M. O., and Friend, D. G., Linstrom, P. J., and Mallard, W. G. (eds.), *NIST Chemistry WebBook, NIST Standard Reference Database Number 69*, Thermophysical Properties of Fluid Systems, National Institute of Standards and Technology, Gaithersburg MD, 20899, 2019.

[44]   Fisher, B. T., Tuttle, S. G., and Pfützner, C. J., "Experimental Approach for Measuring Burn Efficiency of a Reduced-Scale Wellhead Fire," *IOSC*, International Oil Spill Conference, 2020.

[45]   Lips, S. and Meyer, J. P., "Two-phase flow in inclined tubes with specific reference to condensation: A review," *International Journal of Multiphase Flow* Vol. 37, No. 8, 2011, pp. 845-859.
         doi: https://doi.org/10.1016/j.ijmultiphaseflow.2011.04.005

[46]   Rouhani, S. Z. and Sohal, M. S., "Two-phase flow patterns: A review of research results," *Progress in Nuclear Energy* Vol. 11, No. 3, 1983, pp. 219-259.
         doi: https://doi.org/10.1016/0149-1970(83)90012-4

[47]   Taitel, Y., Bornea, D., and Dukler, A. E., "Modelling flow pattern transitions for steady upward gas-liquid flow in vertical tubes," *AIChE Journal* Vol. 26, No. 3, 1980, pp. 345-354.

doi: 10.1002/aic.690260304

[48]   Hasan, A. R. and Kabir, C. S., *Fluid Flow and Heat Transfer in Wellbores*, 2nd ed., Society of Petroleum Engineers, Richardson, Texas, 2018, pp. 403.

[49]   Hasan, A. R. and Kabir, C. S., *Fluid Flow and Heat Transfer in Wellbores,* 2nd ed., Multiphase Flow: Mechanistic Models for Vertical Walls, Society of Petroleum Engineers, Richardson, Texas, 2018.

[50]   Tatterson, D. F., Dallman, J. C., and Hanratty, T. J., "Drop sizes in annular gas-liquid flows," *AIChE Journal* Vol. 23, No. 1, 1977, pp. 68-76.
         doi: 10.1002/aic.690230112

[51]   Cousins, L. B. and Hewitt, G. F., *Liquid Phase Mass Transfer in Annular Two-phase Flow: Droplet Deposition and Liquid Entrainment*, Atomic Energy Research Establishment, 1968.

[52]   Paras, S. V. and Karabelas, A. J., "Properties of the liquid layer in horizontal annular flow," *International Journal of Multiphase Flow* Vol. 17, No. 4, 1991, pp. 439-454.
         doi: https://doi.org/10.1016/0301-9322(91)90041-Z

[53]   Schubring, D. L. Behavior interrelationships in annular flow. Nuclear Engineering and Engineering Physics, The University of Wisconsin - Madison, Madison, Wisconsin, 2009.

[54]   Alamu, M. B. Investigation of periodic structures in gas-liquid flow [PhD]. Chemical and Environmental Engineering, University of Nottingham, Nottingham, UK, 2010.

[55]   Conroy, M. W., Ananth, R., and Tuttle, S. G., "Preliminary Technical Guidance and Literature Review to Assist in Evaluation of Wellhead Burning as a Blowout Response," Bureau of Safety and Environmental Enforcement, OSRR-1063AA. Sterling, VA, 16 February 2016.

[56]   Gill, L. E., Hewitt, G. F., Hitchon, J. W., and Lacey, P. M. C., "Sampling probe studies of the gas core in annular two-phase flow—I The effect of length on phase and velocity distribution," *Chemical Engineering Science* Vol. 18, No. 8, 1963, pp. 525-535.
         doi: https://doi.org/10.1016/0009-2509(63)85013-7

[57]   Ishii, M. and Grolmes, M. A., "Inception criteria for droplet entrainment in two-phase concurrent film flow," *AIChE Journal* Vol. 21, No. 2, 1975, pp. 308-318.
         doi: 10.1002/aic.690210212

[58]   Hinze, J. O., "Fundamentals of the hydrodynamic mechanism of splitting in dispersion processes," *AIChE Journal* Vol. 1, No. 3, 1955, pp. 289-295.
         doi: 10.1002/aic.690010303

[59]   Lopes, J. C. B. Droplet sizes, dynamics and deposition in vertical annular flow [Dissertation]. Chemical Engineering, University of Houston, Houston, TX, 1984.

[60]   Fore, L. B., Ibrahim, B. B., and Beus, S. G., "Visual measurements of droplet size in gas–liquid annular flow," *International Journal of Multiphase Flow* Vol. 28, No. 12, 2002, pp. 1895-1910.
         doi: https://doi.org/10.1016/S0301-9322(02)00121-0

[61]   Roesler, T. C. and Lefebvre, A. H., "Studies on Aerated-Liquid Atomization," *International Journal of Turbo & Jet-Engines* Vol. 6, No. 3-4, 1989, pp. 221-230.
         doi: 10.1515/TJJ.1989.6.3-4.221

[62]   Buckner, H. N. and Sojka, P. E., "Effervescent Atomization of High-Viscosity Fluids: Part I. Newtonian Liquids," *Atomization and Sprays* Vol. 1, No. 3, 1991, pp. 239-252.
         doi: 10.1615/AtomizSpr.v1.i3.10

[63]   Buckner, H. N. and Sojka, P. E., "Effervescent Atomization of High-Viscosity Fluids: Part II. Non-Newtonian Liquids," *Atomization and Sprays* Vol. 3, No. 2, 1993, pp. 157-170.
doi: 10.1615/AtomizSpr.v3.i2.30

[64]   Lund, M. T., Jian, C. Q., Sojka, P. E., Gore, J. P., and Panchagnula, M. V., "The Influence of Atomizing Gas Molecular Weight on Low Mass Flowrate Effervescent Atomizer Performance," *Journal of Fluids Engineering* Vol. 120, No. 4, 1998, pp. 750-754.
doi: 10.1115/1.2820733

[65]   Sovani, S. D., Sojka, P. E., and Lefebvre, A. H., "Effervescent atomization," *Progress in Energy and Combustion Science* Vol. 27, No. 4, 2001, pp. 483-521.
doi: 10.1016/S0360-1285(00)00029-0

[66]   Linne, M., Sedarsky, D., Meyer, T., Gord, J., and Carter, C., "Ballistic imaging in the near-field of an effervescent spray," *Experiments in Fluids* Vol. 49, No. 4, 2010, pp. 911-923.
doi: 10.1007/s00348-010-0883-3

[67]   Lin, E. P. and Hermanson, J. C., "Compression Wave Structure on Droplets under Supersonic Conditions,"*50th AIAA/ASME/SAE/ASEE Joint Propulsion Conference*, American Institute of Aeronautics and Astronautics AIAA-2014-3946.

[68]   LeFebvre, A. H., Chigier, N. (ed.) *Atomization and Sprays,* 1 ed., Basic Processes in Atomization, Hemisphere Publishing Corporation, Boca Raton, 1989, pp. 27-78.

[69]   Faeth, G. M., Hsiang, L. P., and Wu, P. K., "Structure and breakup properties of sprays," *International Journal of Multiphase Flow* Vol. 21, 1995, pp. 99-127.
doi: https://doi.org/10.1016/0301-9322(95)00059-7

[70]   Cohen, J. M. and Rosfjord, T. J., "Influences on the Sprays Formed by High-Shear Fuel Nozzle/S wirler Assemblies," *Journal of Propulsion and Power* Vol. 9, No. 1, 1993, pp. 16-27.
doi: 10.2514/3.51351

[71]   Senecal, P. K., Schmidt, D. P., Nouar, I., Rutland, C. J., Reitz, R. D., and Corradini, M. L., "Modeling high-speed viscous liquid sheet atomization," *International Journal of Multiphase Flow* Vol. 25, No. 6, 1999, pp. 1073-1097.
doi: https://doi.org/10.1016/S0301-9322(99)00057-9

[72]   Lasheras, J. C. and Hopfinger, E. J., "Liquid Jet Instability and Atomization in a Coaxial Gas Stream," *Annual Review of Fluid Mechanics* Vol. 32, No. 1, 2000, pp. 275-308.
doi: 10.1146/annurev.fluid.32.1.275

[73]   Shanmugadas, K. P. and Chakravarthy, S. R., "A canonical geometry to study wall filming and atomization in pre-filming coaxial swirl injectors," *Proceedings of the Combustion Institute* Vol. 36, No. 2, 2017, pp. 2467-2474.
doi: https://doi.org/10.1016/j.proci.2016.08.082

[74]   LeFebvre, A. H., *Atomization and Sprays*, 1 ed., Hemisphere Publishing Corporation, 1989.

[75]   Westlye, F. R., Penney, K., Ivarsson, A., Pickett, L. M., Manin, J., and Skeen, S. A., "Diffuse back-illumination setup for high temporally resolved extinction imaging," *Applied Optics* Vol. 56, No. 17, 2017, pp. 5028-5038.
doi: 10.1364/AO.56.005028

[76]   Kashdan, J. T., Shrimpton, J. S., and Whybrew, A., "Two-Phase Flow Characterization by Automated Digital Image Analysis. Part 1: Fundamental Principles and Calibration of the Technique," *Particle & Particle Systems Characterization* Vol. 20, No. 6, 2003, pp. 387-397.

doi: 10.1002/ppsc.200300897

[77] Kashdan, J. T., Shrimpton, J. S., and Whybrew, A., "Two-Phase Flow Characterization by Automated Digital Image Analysis. Part 2: Application of PDIA for Sizing Sprays," *Particle & Particle Systems Characterization* Vol. 21, No. 1, 2004, pp. 15-23.
doi: 10.1002/ppsc.200400898

[78] Lowe, A., Kourmatzis, A., and Masri, A. R., "Turbulent spray flames of intermediate density: Stability and near-field structure," *Combustion and Flame* Vol. 176, 2017, pp. 511-520.
doi: https://doi.org/10.1016/j.combustflame.2016.10.024

[79] Veynante, D. and Vervisch, L., "Turbulent combustion modeling," *Progress in Energy and Combustion Science* Vol. 28, No. 3, 2002, pp. 193-266.
doi: https://doi.org/10.1016/S0360-1285(01)00017-X

[80] Amirante, R., Distaso, E., Tamburrano, P., and Reitz, R. D., "Laminar flame speed correlations for methane, ethane, propane and their mixtures, and natural gas and gasoline for spark-ignition engine simulations," *International Journal of Engine Research* Vol. 18, No. 9, 2017, pp. 951-970.
doi: 10.1177/1468087417720018

[81] Smith, T. F., Shen, Z. F., and Friedman, J. N., "Evaluation of Coefficients for the Weighted Sum of Gray Gases Model," *Journal of Heat Transfer* Vol. 104, No. 4, 1982, pp. 602-608.
doi: 10.1115/1.3245174

[82] Khan, I. M. and Greeves, G., Afgan, N. H., and Beér, J. M. (eds.), *Heat Transfer in Flames,* Vol. 2, A Method for Calculating the Formation and Combustion of Soot in Diesel Engines, Scripta Book Company, Ann Arbor, Michigan, 1974.

[83] Gosman, A. D. and Ioannides, E., "Aspects of Computer Simulation of Liquid-Fueled Combustors," *Journal of Energy* Vol. 7, No. 6, 1983, pp. 482-490.
doi: 10.2514/3.62687

[84] Bertodano, M. A. L. d., Jan, C.-S., and Beus, S. G., "Annular flow entrainment rate experiment in a small vertical pipe," *Nuclear Engineering and Design* Vol. 178, No. 1, 1997, pp. 61-70.
doi: https://doi.org/10.1016/S0029-5493(97)00175-1

[85] O'Rourke, P. J. Collective Drop Effects on Vaporizing Liquid Sprays [Doctoral], Princeton, Princeton, New Jersey, 1981.

[86] Gumprich, W., Chrigui, M., Braun, M., and Sadiki, A., "Evaluation of collision models applied to varying dense particle jets flows,"*7th International Conference on Multiphase Flow*, International Conference on Multiphase Flow May 30 – June 4, 2010.

[87] Turns, S. R., Turns, S. R. (ed.) *An Introduction to Combustion: Concepts and Applications,* 2 ed., Oxidation of Higher Paraffins, McGraw-Hill, Boston, USA, 2000, p. 153.

[88] Hamoodi, A. N., Abed, A. F., and Firoozabadi, A., "Compositional Modeling of Two-Phase Hydrocarbon Reservoirs,"*Abu Dhabi International Petroleum Exhibition and Conference*, Society of Petroleum Engineers 1996/1/1/.

[89] Ali, A., Mehta, V., Ogbe, D. O., Kamath, V. A., and Patil, S. L., "Fluid Characterization for Compositional Simulation with Application to Endicott Field, Alaska,"*SPE Western Regional Meeting*, Society of Petroleum Engineers 1994/1/1/.

[90] IHRDC. "Crude Oil and Natural Gas: From Source to Final Products." IHRDC, 2017.
https://www.ihrdc.com/els/po-demo/module01/mod_001_02.htm

[91] Tuttle, S. G., Farley, J. P., and Fleming, J. W., "Efficient Atomization and Combustion of Emulsified Crude Oil," Naval Research Laboratory, NRL/MR/6185-14-9566. Washington, DC, September 2014.

[92] Fisher, B. T., Weismiller, M. R., Tuttle, S. G., and Hinnant, K. M., "Effects of Fluid Properties on Spray Characteristics of a Flow-Blurring Atomizer," *Journal of Engineering for Gas Turbines and Power* Vol. 140, No. 4, 2018, pp. 041511-041511-8.
doi: 10.1115/1.4038084

[93] Linne, M., "Imaging in the optically dense regions of a spray: A review of developing techniques," *Progress in Energy and Combustion Science* Vol. 39, No. 5, 2013, pp. 403-440.
doi: https://doi.org/10.1016/j.pecs.2013.06.001

[94] Tuesta, A. D., Bhuiyan, A., Lucht, R. P., and Fisher, T. S., "Laser Diagnostics of Plasma in Synthesis of Graphene-Based Materials," *Journal of Micro and Nano-Manufacturing* Vol. 2, No. 3, 2014, pp. 031002-031002.
doi: 10.1115/1.4027547

[95] Lucht, R. P., "Three-laser coherent anti-Stokes Raman scattering measurements of two species," *Optics Letters* Vol. 12, No. 2, 1987, pp. 78-80.
doi: 10.1364/OL.12.000078

[96] Thariyan, M. P., Bhuiyan, A. H., Meyer, S. E., Naik, S. V., Gore, J. P., and Lucht, R. P., "Dual-pump coherent anti-Stokes Raman scattering system for temperature and species measurements in an optically accessible high-pressure gas turbine combustor facility," *Measurement Science and Technology* Vol. 22, No. 1, 2011, p. 015301.
doi: 10.1088/0957-0233/22/1/015301

[97] Kearney, S. P. and Jackson, M. N., "Dual-Pump Coherent Anti-Stokes Raman Scattering Thermometry in Heavily Sooting Flames," *AIAA Journal* Vol. 45, No. 12, 2007, pp. 2947-2956.
doi: 10.2514/1.31054

[98] Jacob, R. J., Kline, D. J., and Zachariah, M. R., "High speed 2-dimensional temperature measurements of nanothermite composites: Probing thermal vs. Gas generation effects," *Journal of Applied Physics* Vol. 123, No. 11, 2018, p. 115902.
doi: 10.1063/1.5021890

[99] Laurendeau, N. M., *Statistical Thermodynamics: Fundamentals and Applications*, Equilibrium Radiation, Cambridge University Press, 2005, pp. 275-281.

[100] Ng, D. and Fralick, G., "Use of a multiwavelength pyrometer in several elevated temperature aerospace applications," *Review of Scientific Instruments* Vol. 72, No. 2, 2001, pp. 1522-1530.
doi: 10.1063/1.1340558

[101] Fu, T., Wang, Z., and Cheng, X., "Temperature Measurements of Diesel Fuel Combustion With Multicolor Pyrometry," *Journal of Heat Transfer* Vol. 132, No. 5, 2010, pp. 051602-051602-7.
doi: 10.1115/1.4000467

[102] DeWitt, D. P. and Nutter, G. D., *Theory and Practice of Radiation Thermometry*, Wiley, 1988.

[103] Turns, S. R., *An Introduction to Combustion: Concepts and Applications*, 3 ed., McGraw-Hill, Boston, USA, 2012, pp. 732.

[104] Weismiller, M. R., Huba, Z. J., Tuttle, S. G., Epshteyn, A., and Fisher, B. T., "Combustion characteristics of high energy Ti–Al–B nanopowders in a decane spray flame," *Combustion and Flame* Vol. 176, 2017, pp. 361-369.
doi: 10.1016/j.combustflame.2016.10.025

[105] Thirion, J. P., "Image matching as a diffusion process: an analogy with Maxwell's demons," *Medical Image Analysis* Vol. 2, No. 3, 1998, pp. 243-260.
doi: https://doi.org/10.1016/S1361-8415(98)80022-4

[106] Vercauteren, T., Pennec, X., Perchant, A., and Ayache, N., "Diffeomorphic demons: efficient non-parametric image registration," *Neuroimage* Vol. 45, No. 1 Suppl, 2009, pp. S61-72.
doi: 10.1016/j.neuroimage.2008.10.040

[107] Tuesta, A. D., Fisher, B. T., and Tuttle, S. G., "Dual Pump CARS Thermometry and Relative Mole Fractions Measurements in a Heptane/Propane Spray Flame," *41st AMOP Technical Seminar on Environmental Contamination and Response*, Environment and Climate Change Canada, Ottawa, Ontario, Canada, 2018.

[108] Fisher, B. T., Tuttle, S. G., Pfützner, C. J., and Kessler, D. A., "Method for Measuring Burn Efficiency of Spray Flames that Simulate Scaled-Down Petroleum Wellhead Fires," *Fuel* Vol. *Accepted*, 2020.

[109] Kessler, D. A., Fisher, B. T., Tuesta, A. D., and Tuttle, S. G., "The Influence of Droplet Injection Models on Reynolds-Averaged Navier-Stokes Simulations of High-Speed Heptane/Ethane Spray Flames,"*11th U. S. National Combustion Meeting*, Combustion Institute March 24–27, 2019.

[110] Kessler, D. A., Fisher, B. T., Tuesta, A. D., and Tuttle, S. G., "Reynolds-Averaged Navier-Stokes Simulations of a Piloted Heptane/Propane Spray Flame,"*Spring Technical Meeting of the Eastern States Section of the Combustion Institute*, 6-8 March 2018.

[111] Fisher, B. T., Tuttle, S. G., Tuesta, A. D., Jacob, R. J., Kessler, D. A., and Pfützner, C. J., "High-Speed Imaging of Spray Near-Field Behavior in a Turbulent Heptane/Ethane Spray Flame,"*11th U. S. National Combustion Meeting*, Combustion Institute March 24–27, 2019.

[112] Laurendeau, N. M., *Statistical Thermodynamics: Fundamentals and Applications*, Concentration and Temperature Measurements, Cambridge University Press, 2005, pp. 223-241.

[113] Demtröder, W., *Laser Spectroscopy: Vol. 1: Basic Principles*, 4th ed., Springer Berlin Heidelberg, 2008.

APPENDIX A

ADDITIONAL EXPERIMENTAL INSTRUMENTATION

Tunable-Diode Laser Absorption Spectroscopy

In effort to validate the CARS thermometry, an attempt was made by Dr. Michael Button to measure the flat-flame burner temperature with tunable-diode laser absorption spectroscopy (TDLAS) using water vapor thermometry. TDLAS is a laser-based diagnostic method that passes a laser through a gas field and then measures the absorption of that beam based on the Beer-Lambert attenuation law:

$$I_\nu(L) = I_\nu(0)e^{-k_\nu L} \tag{44}$$

where I_ν is the intensity of light at a given frequency of light, ν, L is the path length the laser passes through the absorbing medium or gas, and k_ν is the absorption coefficient based on the probability density function, line profile absorption function, and the absorptive Einstein coefficient that describes the transition behavior of the absorbing molecule [112,113].
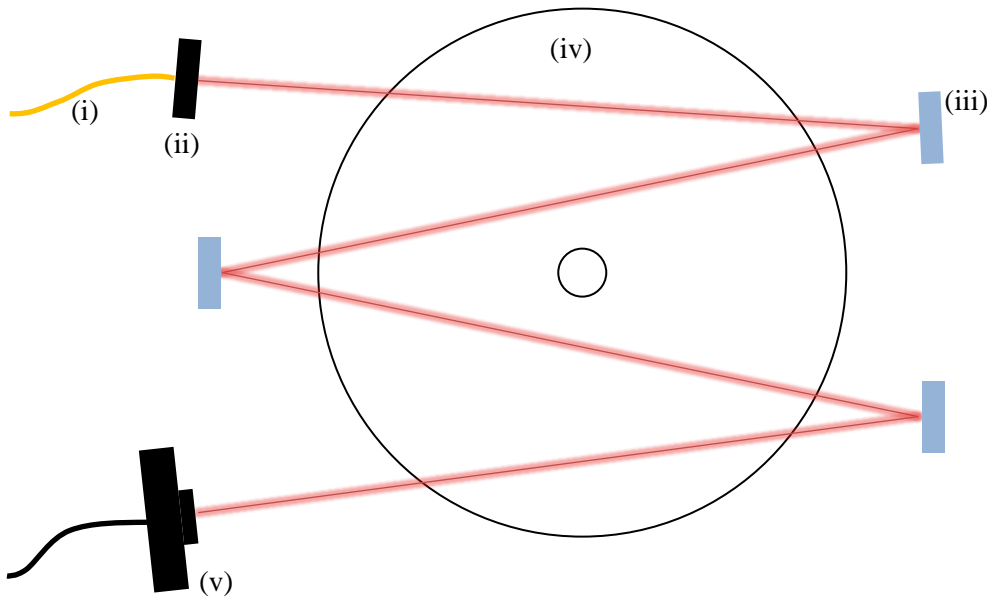
Fig. 54-Diagram of TDLAS experiment (top view). The laser is produced by a tunable diode laser, transmitted through a fiber (i), transmission optics (ii), reflected by mirrors across the hot exhaust gases above the burner (iv), and then into receiving optics and a photodiode (v).

Figure 54 shows a top view of the optical layout of the experiment with relation to the laboratory burner flat flame. Data have been collected with this apparatus and with the CARS system for two flat-flame conditions – a relatively low-temperature (~1215 K) H_2/air flame and a relatively high-temperature (~2115 K) propane/air flame. CARS data have been processed and are in relatively good agreement with the calculated adiabatic flame temperatures, while the TDLAS data are still being processed. The objective is to use TDLAS-based temperature measurements to validate the CARS thermometry system in a simple configuration (i.e., premixed flat flame), so that CARS data can be considered trustworthy for measurements in the much more complex spray flame.
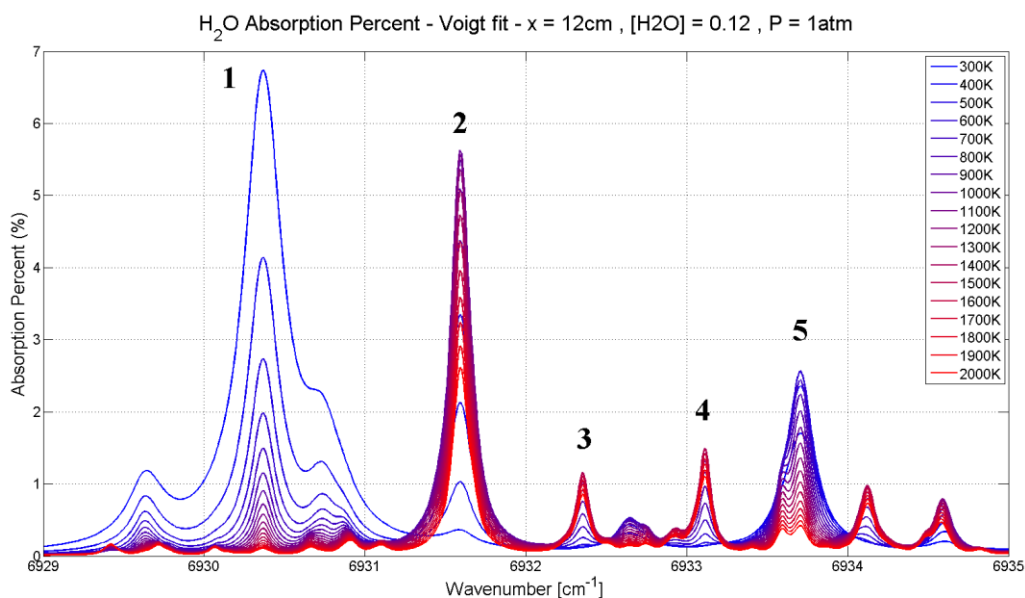

Fig. 55-Theoretical profiles of water vapor absorption features at temperature from 300 to 2000 K.

The TDLAS temperature measurements performed are based on water vapor ratiometry. Figure 55 illustrates the theoretical profiles of water vapor absorption features from 6929 to 6935 1/cm. Ratiometry is a measurement technique in which the relative amplitude of absorption features are compared to yield a temperature. As an abundant molecule in the combustion process, water vapor is an excellent molecule to probe. However, rotational transitions are complex and many across a wide spectral range giving rise to overlapping absorption features. Furthermore, water vapor is also abundant in relatively cool, ambient air through which the tunable diode laser also penetrates. This means that in order to evaluate the temperature of the water vapor within the flame, the features from the cool, ambient water vapor must not be neglected. Due to the complexities of water ratiometry, the uncertainty of the results were not satisfactory and this instrumentation course was not pursued to conclusion.

APPENDIX B

SUBMITTED JOURNAL PAPERS:

Method for Measuring Burn Efficiency for Spray Flames that Simulate Scaled-Down Petroleum Wellhead Fires

Paper included as attachment.